Numerical Methods For Organic Optoelectronic Devices: Simulations And Experiments

Emanuele Bezzeccheri

Unione Europea

Ministero dell'Istruzione,
dell'Università e della Ricerca

UNIVERSITÀ DEGLI
STUDI DI SALERNO

FONDO SOCIALE EUROPEO
Programma Operativo Nazionale 2000/2006
"Ricerca Scientifica, Sviluppo Tecnologico, Alta Formazione"
Regioni dellObiettivo 1 Misura III.4
"Formazione superiore ed universitaria"

Department of Industrial Engineering

Ph.D. Course in Industrial Engineering
(XVI Cycle-New Series, XXX Cycle)

Numerical Methods For Organic Optoelectronic Devices: Simulations and Experiments

Supervisor	**Ph.D. student**
Prof. Alfredo Rubino	*Emanuele Bezzeccheri*

Scientific Referees
Prof. Antonio Cassinese
Dr. Matthias Auf Der Maur

Ph.D. Course Coordinator
Prof. Ernesto Reverchon

Academic Year 2017-2018

Dedicated to the memory of Prof. Salvatore Bellone

Eri figlio del rancore,
Di quel rancore che cancella il viso e lascia i corridoi silenti,
Amplifica il rumore di chi preferì le proprie carte al proprio letto.

Eri figlio del rancore,
Di chi non fissa per paura di essere fissato,
Con gli occhi rossi di sonno come chi nn si dà pace.

Eri figlio del rancore,
Di chi ha avuto troppo e al contempo niente,
Di chi voleva star vicino e scappare,
Di chi era rimasto bambino, la lingua attorcigliata in idioglossia.

E noi siam figli tuoi.

Eppure, nonostante l'ostinato rancore, siam tutti ancora svegli,
E il mondo tutto si è chinato improvvisamente attorno alle tue spoglie,
Ultima presa in giro e massimo torto,
Per non farti morire come hai vissuto,
Come avresti voluto.

Un ultimo saluto per liberare la tua anima.

(E.B.)

Acknowledgments

The results reported in this work have often been obtained with limited resources and a great amount of personal sacrifice. Nevertheless, it is true indeed that this could not have happened without the help of many people. Taking the doctoral path means acquiring hard and soft skills of great value inside and outside the academic environment. Those include being able to express complex ideas in a plain language, having a creative approach to new and common problems, developing intellectual rigor – which is even more important nowadays in a post-truth era.

For me, above all, PhD commitment developed the even more important ability of being able to handle whatever life throws at me. No problem is too big now to be confronted. I owe my gratitude for this lesson learned to my academic tutor, Prof. Alfredo Rubino. I also want to thank all the members and colleagues of the Microelectronics Laboratory at the University of Salerno: Rosalba Liguori – for her support and counsel, Carmine Cappetta – for the unconditional help, Luigi Di Benedetto and Prof. Gian Domenico Licciardo – for the stimulating discussions on electronic devices. A big thank you goes to Aldo Femia as well, for being my student and having to endure me through all the hours of hard work.

I remain grateful to Prof. Paolo Lugli, who kindly accepted me in his research team at the Technical University of Munich, department of Nanoelectronics. I learned a great deal during this experience on both professional and personal regards, as this expertise will remain in my engineering and human portfolio for the years to come. I also want to thank the many colleagues I met there, with whom I shared thoughts, visions, helles bier und halbes hendl: Simone Colasanti, Pietro Luppina, Florin-Christian Loghin, Bogdan Popescu, Katharina Melzer, Ahmed Abdelhalim, Vijay Deep Bhatt, Claudio Ciceroni and Mattia Petrelli. Even though I stayed in Munich for a short period, I have met many people that helped me in a way or another. My acknowledgment goes to Marco, Olivier, Manuel, Matt, Janine and the mighty Ciro.

My sincere gratitude goes to my managers Ewan McCulloch and Dave

Morrison for giving me the opportunity to conclude the last period of my PhD while working at Cadence Design Systems in Livingston, UK. I would also like to thank the whole Cadence team for reigniting the fire of engineering that I lost somehow in the process and maybe a long time ago.

A very special thank you goes to my friend and colleague Aniello Falco, who always supported me during this three years and to whom I owe a lot, for sure my life during the journey in the lands of always winter. A particular mention also goes to my long-time sensei Salvatore Aprano, who saved me right in time once again from the height of his wisdom and proved to be a real deus-ex-machina.

Last but not least, my deep love goes to my girlfriend Alessandra – I could not have survived the hard times without your kindness, sweetness and shank-kicking attitude, you just know that – and to my parents and family, that were always there to support me in everything I could need, despite issues and problems.

Emanuele

List of Publications

Journals

Casa, M., Sarno, M., Liguori, R., Cirillo, C., Rubino, A., Bezzeccheri, E., Liu, J. and Ciambelli, P. (2018), ‘Conductive adhesive based on mussel-inspired graphene decoration with silver nanoparticles’, *Journal of Nanoscience and Nanotechnology* **18**(2), 1176–1185.

Falco, A., Petrelli, M., Bezzeccheri, E., Abdelhalim, A. and Lugli, P. (2016), ‘Towards 3d-printed organic electronics: Planarization and spray-deposition of functional layers onto 3d-printed objects’, *Organic Electronics* **39**, 340–347.

Vaiano, V., Sacco, O., Iervolino, G., Sannino, D., Ciambelli, P., Liguori, R., Bezzeccheri, E. and Rubino, A. (2015), ‘Enhanced visible light photocatalytic activity by up-conversion phosphors modified n-doped tio 2’, *Applied Catalysis B: Environmental* **176**, 594–600.

Conference Proceedings

Bezzeccheri, E., Colasanti, S., Falco, A., Liguori, R., Rubino, A. and Lugli, P. (2016), Comparative modeling of vertical and planar organic phototransistors with 2d drift-diffusion simulations, *in* ‘VIII International Conference on ”Times of Polymers and Composites”’, Vol. 1736, AIP Publishing, pp. 020084–1.

Bezzeccheri, E., Femia, A., Liguori, R. and Rubino, A. (In publication), Interface trap state characterization of metal-insulator-semiconductor structures based on photosensitive organic materials, *in* ‘Materials Today: Proceedings (9th International Symposium on Flexible Organic Electronics, Thessaloniki, Greece, 4-7 July 2016)’.

Falco, A., Nagel, R., Lugli, P., Bezzeccheri, E., Liguori, R. and Rubino, A. (2016), Simulation and fabrication of polarized organic photodiodes, *in* ‘SENSORS, 2016 IEEE’, IEEE, pp. 1–3.

Fiorillo, M. R., Liguori, R., Diletto, C., Bezzeccheri, E., Tassini, P., Maglione, M. G., Maddalena, P., Minarini, C. and Rubino, A. (In publication), Trap density analysis in pc70bm n-type thin film transistors through admittance studies, *in* ‘Materials Today: Proceedings (9th International Symposium on Flexible Organic Electronics, Thessaloniki, Greece, 4-7 July 2016)’.

Liguori, R., Sheets, W. C., Bezzeccheri, E., Facchetti, A. and Rubino, A. (2016), Combination of light-induced effect and gate bias stress in organic phototransistors, *in* ‘VIII International Conference on ”Times of Polymers and Composites”’, Vol. 1736, AIP Publishing, pp. 020167–1.

Table of Contents

Page

List of Figures v

List of Tables vii

Abstract ix

Abstract (Italiano) xi

Introduction xiii

Chapter 1- Organic Electronics 1
1.1 Introduction 1
1.2 Organic Semiconductors 2
    1.2.1 Charge Transport 5
    1.2.2 Light Absorption 8
    1.2.3 Light Emission 9
1.3 Numerical Methods 10
    1.3.1 Atomistic Simulations 11
    1.3.2 Monte Carlo Simulations 12
    1.3.3 Continuum Simulations 13
    1.3.4 Multiscale Simulations 15
1.4 Conclusion 16

Chapter 2- Technology Computer-Aided Design 17
2.1 Introduction 17
2.2 Semiconductor Equations 18
    2.2.1 Electrostatic Potential 18

2.2.2 Carrier Transport 21
2.2.3 Carrier Recombination 22
2.2.4 Traps 24
2.2.5 Optical Generation 25
2.2.6 Boundary Conditions 27
2.3 Discretization 29
2.4 Solving Methods 30
2.5 Application to Organic Semiconductors 32
2.5.1 Organic Light Emitting Diodes 33
2.5.2 Organic Photovoltaics 33
2.5.3 Organic Field-Effect Transistors 34
2.5.4 Organic Photodiodes 35
2.6 Materials Modeling 36
2.6.1 Electrodes 36
2.6.2 PEDOT:PSS 37
2.6.3 P3HT 38
2.6.4 $PC_{61}BM$ 38
2.6.5 $P3HT:PC_{61}BM$ 39
2.6.6 Al_2O_3 40
2.7 Conclusion 40

Chapter 3- The Organic Field-Effect Transistor **43**
3.1 Introduction 43
3.2 State of the Art 44
3.2.1 DC Characteristics 46
3.2.2 AC Characteristics 49
3.3 Bulk Heterojunction-Based Transistors 51
3.3.1 Current-Voltage Analysis 52
3.3.2 Admittance Analysis 57
3.4 Conclusion 62

Chapter 4- The Vertical Organic Transistor **65**
4.1 Introduction 65
4.2 State of the Art 66
4.2.1 Organic Permeable Base Transistor 67
4.2.2 Organic Static Induction Transistor 69
4.2.3 Organic Schottky Barrier Transistor 70
4.2.4 Vertical Organic Field Effect Transistor 73
4.3 Organic Phototransistor Application 74

4.3.1 Simulated Device Structures 75
4.3.2 Tuning the Bulk Heterojunction Model 76
4.3.3 Current-Voltage Analysis 77
4.3.4 Band Diagram 79
4.3.5 External Quantum Efficiency 81
4.3.6 Performance Improvements 82
4.4 Conclusion 84

Chapter 5- The Polarized Organic Photodiode 87
5.1 Introduction 87
5.2 State of the Art 87
5.3 Monolithic Integration 89
5.3.1 Device Evaluation 90
5.3.2 Device Feedback 94
5.4 Modeling the Bulk Heterojunction Morphology 97
5.4.1 Spin Exchange Algorithms 97
5.4.2 Monte Carlo Simulations 100
5.4.3 TCAD Simulations 106
5.5 Conclusion 107

Conclusion and Outlook 109

Appendix A- Material Parameters 113

Appendix B- Names Of Chemical Compounds 117

Bibliography 119

List of Symbols 145

Acronyms 153

List of Figures

1 The Ethylene molecule showing the concept of molecular orbitals. Adapted from Köhler and Bässler (2015). 4
2 Charge Transport: a) hopping picture, b) MTR picture. 7
3 The numerical methods paradigm in organic electronics. . . . 11
4 A typical simulation flow in TCADs. 14
5 Impinging, reflected and transmitted rays on an optical interface. 26
6 Delaunay mesh: a) circumscribing circles, b) seeds, c) complementary Voronoï grid (red). 29
7 Newton's method: a) fully-coupled iterations, b) de-coupled iterations (Gummel). 31
8 OFET configurations: a) BGTC, b) BGBC, c) TGBC, d) TGTC (Klauk (2010)). 45
9 Experimental and modeled OFETs transfer curves: a) linear scale, b) logarithmic scale. 52
10 Experimental and simulated OFETs currents: a) transfer curve (lin. scale), b) transfer curve (log. scale), c) P3HT output curves, d) BHJ output curves. 55
11 Simulations of OFETs transfer curves varying the interface traps concentration. 56
12 Experimental and modeled OFETs admittance: a) P3HT capacitance, b) BHJ capacitance, c) P3HT loss, d) BHJ loss. . . . 58
13 Equivalent circuits for a) P3HT OFET admittance and b) BHJ OFET admittance. 58
14 Experimental and simulated OFETs admittance: a) P3HT capacitance, b) BHJ capacitance, c) P3HT loss, d) BHJ loss. . . . 60
15 Simulations of OFETs loss function varying the interface traps concentration. 61
16 OFETs cut-off frequencies. 62

17 The various VOT structures: a) OPBT, b) OSIT, c) OSBT, d) VOFET. 66
18 Simulated OPT structures (not in scale): a) BGBC-OFET, b) OSIT. 75
19 Reference OPD simulations: a) trap distributions, b) band diagram (equilibrium), c) dark currents, d) *k* and EQE. 78
20 J-V Characteristics: a) OFET output curves, b) OFET transfer curves, c) OSIT output curves, d) OSIT transfer curves. 79
21 The band diagram of the OSIT a) in equilibrium and b) under a drain bias; c) the space charge in the pinch-off region; d) the average intrinsic gate barrier. 80
22 The EQE of a) the OFET and b) the OSIT. 81
23 The staggered-gate OSIT structure. 82
24 Simulations of the staggered-gate OSIT: a) output curves, b) band diagram, c) transfer curves, d) EQE. 83
25 OLED/OPD cross polarization scheme for LoC analytic applications (Pais et al. (2008)). 88
26 Monolithic integration of a POPD: a) application of a WGP, b) integration of a WGP, c) realization of the POPD. 89
27 WGP FDTD simulations: a) transmissions, b) PER. 91
28 POPD structure in TCAD simulations. 92
29 A diagram showing the flow of POPD TCAD simulations. . . 92
30 TCAD simulations of the POPD: a) currents, b) EQE. 93
31 Comparison between experimental data and simulations: a) currents, b) EQE. 94
32 WGP FDTD simulations for a more realistic structure: a) transmissions, b) PER. 95
33 Refinement of POPD simulations using more accurate transmission value: a) currents, b) EQE. 95
34 Refinement of POPD simulations using an Auger-like recombination rate: a) currents, b) EQE. 96
35 Spin exchange algorithms: a) Metropolis, b) Bortz. 99
36 Class coupling for a 3D lattice in the Bortz algorithm. 99
37 Lattice evolution MC simulations: a) average grain size, b) classes population. 104
38 Generated morphologies: a 2D lattice a) before and b) after the evolution; a 3D lattice a) before and b) after the evolution. . . 105
39 TCAD simulations of BHJ morphologies: a) 2D current density distribution (V=-1 V), b) J-V characteristics. 106

List of Tables

1 Box integration coefficient for Poisson and continuity equations. 30
2 Electrode model parameter values. 37
3 PEDOT:PSS model parameter values. 38
4 P3HT model parameter values. 38
5 $PC_{61}BM$ model parameter values. 39
6 $P3HT:PC_{61}BM$ model parameter values. 39
7 Al_2O_3 model parameter values. 40
8 Empirical and fitting parameters in the Marinov, Estrada and Li OFET DC compact models. 49
9 The parameters employed in the fitting model of the OFET currents. 53
10 The parameters employed in OFET DC simulations. 56
11 The parameters employed in P3HT OFET admittance equivalent circuit. 59
12 The parameters employed in BHJ OFET admittance equivalent circuit. 59
13 The salient features of state-of-the-art n-type and p-type OPBTs. 69
14 The salient features of state-of-the-art OSITs. 70
15 The salient features of the OSBTs reported by Yang, Tessler and Rinzler groups. 72
16 $P3HT:PC_{61}BM$ BHJ bulk traps model values. 76
17 $P3HT:PC_{61}BM$ BHJ interface traps model values. 77
18 Class characterization for a 3D lattice ($T = 300\ K$). 100
19 PEDOT:PSS characterization in the literature. 113
20 P3HT characterization in the literature. 114
21 $PC_{61}BM$ characterization in the literature. 114
22 $P3HT:PC_{61}BM$ characterization in the literature. 115
23 ITO characterization in the literature. 115

24 Al_2O_3 characterization in the literature. 115

Abstract

In recent years, the field of organic electronics has been experiencing a great expansion, due to several characteristics which candidate it as a main player in the definition of new markets comprising low-cost, flexible and biocompatible electronics.

Although many experimental works on the optimization of organic devices have been performed, a real improvement in performance is subordinate to a good understanding of the underlying physical phenomena. At this purpose, computer-based simulations are of great importance for the determination of suitable high-level models and the identification of limiting factors.

This thesis is focused on the application of state-of-the-art Technology Computer Aided Design (TCAD) tools to organic electronics, aiming to show how models peculiar to this field can be integrated into a commercial, mass-production oriented software and exploited for the analysis and design of novel devices. In this respect, particular importance is given to Organic Phototransistors (OPTs) and Organic Photodiodes (OPDs), which rely on Bulk Heterojunction (BHJ) organic semiconductors in order to enhance the photogeneration quantum yield.

To study the transport properties of a BHJ, testbed Organic Field-Effect Transistors (OFETs) are fabricated on Silicon substrates with conventional techniques, such as spin-coating deposition. The current-voltage characteristics and impedance curves of the OFETs are described using TCAD simulations. This analysis shows how the transport of charge is limited by the presence of electronic traps in the material, which negatively affect the subthreshold swing and cut-off frequency of the OFET.

These considerations can be directly applied to vertical OPTs. A comparative modeling study is performed in comparison to a planar OPT with means of TCAD simulations. Results show that vertical devices can outperform the planar ones in both electrical and optical characteristics, which confirms vertical OPT a promising technology due to the advantages of reduced channel length and large sensitive area.

The TCAD methodology also applies to the design rather than analysis only. This concept is demonstrated on a novel OPD architecture, in which a wire-grid polarizer is directly integrated into the device in order to make the photocurrent sensitive to light polarization. The OPD is studied and optimized using numerical simulations, stressing the effect of important physical and geometrical parameters. Consequently, a proof-of-concept of the OPD is demonstrated and the model is refined. A Monte Carlo approach is also proposed in order to enhance the semiconductor models used for the simulation of BHJ materials.

In conclusion, this work describes a complete framework in which organic electronics models are integrated with state-of-the-art TCAD tools. It is our opinion this approach will set the basis for a better understanding and design of organic electronic devices in the near future.

Abstract (Italiano)

Recentemente, il campo dell'elettronica organica è stato soggetto ad una forte espansione, grazie a diverse caratteristiche che lo candidano ad avere un ruolo importante nella definizione di nuovi mercati caratterizzati da dispositivi biocompatibili, flessibili ed a basso costo.

Sebbene diversi lavori sperimentali siano stati effettuati circa il perfezionamento dei dispositivi organici, un reale miglioramento delle loro prestazioni è subordinato alla comprensione dei meccanismi fisici che ne regolano il funzionamento. A questo proposito grande importanza rivestono le simulazioni al calcolatore elettronico, in quanto consentono lo sviluppo di modelli di alto livello e l'identificazione di fattori limitanti.

Questa tesi tratta dell'applicazione di simulatori numerici allo studio dei dispositivi elettronici realizzati con semiconduttori organici, ponendosi come scopo quello di mostrare in che modo modelli peculiari di questa branca possano essere integrati all'interno di software commerciali e orientati alla produzione di massa, in modo da essere sfruttati per l'analisi e il progetto di nuovi dispositivi. A tale proposito, particolare importanza è data ai fototransistori e fotodiodi realizzati con miscele di due semiconduttori organici dalle diverse proprietà, molto utilizzate da un punto di vista tecnologico in quanto consentono di aumentare l'efficienza di resa quantica e la fotogenerazione ottica.

Per studiare le proprietà di trasporto di tali miscele, sono stati fabbricati dei transistori di prova su substrati convenzionali in Silicio cristallino mediante l'utilizzo di deposizione tramite spin-coating. Le caratteristiche corrente-tensione e le curve di impedenza dei transistori sono state descritte attraverso simulazioni numeriche. Tale analisi mostra come il trasporto di carica è limitato dalla presenza di trappole elettroniche nella miscela che influiscono negativamente sullo swing di sottosoglia e sulla frequenza di taglio dei transistori.

Tali considerazioni possono essere applicate direttamente ai fototransistori verticali. Uno studio basato su simulazioni numeriche è stato effettuato in maniera da confrontare le prestazioni di un fototransistore planare e di uno verticale. I risultati mostrano come i dispositivi verticali hanno migliori per-

formance sia da un punto di vista elettrico che ottico, il che conferma come i fototransistori verticali siano una tecnologia promettente grazie ad una ridotta lunghezza di canale e ad una grande area sensibile.

Una metodologia basata su simulazioni numeriche può essere applicata anche alla progettazione, oltre che all'analisi di tali dispositivi. Questo concetto è stato dimostrato su una nuova architettura di fotodiodo, in cui un polarizzatore a griglia è stato direttamente integrato all'interno del dispositivo in modo da ottenere una fotocorrente sensibile alla polarizzazione della luce incidente. Tale architettura è stata in principio studiata e ottimizzata attraverso l'ausilio di simulazioni numeriche, stressando l'effetto di importanti parametri fisici e geometrici. Successivamente, un prototipo è stato realizzato a dimostrazione delle sue operazioni, rifinendo di conseguenza il modello teorico utilizzato per il progetto. Un approccio basato su simulazioni di tipo Monte Carlo è stato inoltre proposto in modo da migliorare il modello impiegato per le simulazioni della miscela organica utilizzata come strato semiconduttore.

In conclusione, questo lavoro descrive una completa metodologia in cui modelli peculiari dell'elettronica organica sono integrati in simulatori numerici allo stato dell'arte per l'analisi e il progetto di dispositivi elettronici organici. È nostra opinione che tale approccio sarà alla base per una miglior comprensione di tali dispositivi in un futuro prossimo.

Introduction

Organic Semiconductors (OSCs) combine the advantages of semiconducting materials with the chemical and mechanical benefits of organic compounds such as plastics. These materials join the ability to conduct electricity and absorb or emit light with a structure that can easily be modified by chemical synthesis – for example, to tailor emission or absorption spectra, to achieve solubility, to allow for mechanically robustness or the fabrication of lightweight and flexible thin films. These peculiar properties have attracted increasing interest from the scientific community, spreading to the industrial world through the huge quantities of projects involving more or less big enterprise partners. This has – in some cases – resulted to the mass production of items targeting semiconductor applications, such as displays, lighting panels and solar cells produced with a variety of solution-processing techniques or vacuum deposition methods.

Nonetheless, the full potential of organic electronics has not yet been fully unveiled, since a number of applications still struggle to exit the academic umbrella to be exploited in market-oriented products. This is especially true for sensing purposes, where the application of optoelectronic devices – as Organic Photodiodes (OPDs) and Organic Phototransistors (OPTs) – is of foremost importance. These devices perform an electro-optical conversion, i.e. of light into electrical quantities (current, voltage, etc.).

A real boost to their development can be achieved by introducing numerical simulations in the design and analysis phases of the product. Those methodologies are extremely valuable in order to drop the trial-and-error experimental effort, cut out the waste of resources and improve the time-to-market of targeted products, as already exploited by the huge expansion of the Silicon electronics – and in the general the one related to inorganic semiconductors – in the last thirty years.

Following these considerations, the present thesis is primarily focused on the numerical analysis of organic optoelectronic devices. In particular, Technology Computer Aided Design (TCAD) is exploited for the analysis, design and implementation of novel device concepts – like vertical and planar phototransistors as well as polarized photodiodes – in order to highlight current capacity and limitations of state-of-the-art tools. The organization of this work is highlighted in the following.

In Chapter 1, an introduction to OSCs is given, especially for what concern conduction and light absorption/emission mechanisms. In addition, a survey on the state-of-the-art of the application of numerical simulations to organic devices is also given, highlighting differences and commonalities of existing approaches, as atomistic simulations, Monte Carlo (MC) simulations, continuum simulations and multiscale simulations.

In Chapter 2, the focus is conveyed on the application of TCAD tools, since they are mainly employed in this work. A TCAD is a computer-based simulator capable of systematically integrate the various physical phenomena contributing to the behavior of a semiconductor device in form of Partial Differential Equations (PDEs) to mathematically describe fabrication processes and semiconductor operations. The most common models employed in TCAD simulations are presented, with particular interest to those specifically describing OSCs. Techniques employed for space discretization and equations solution are also introduced. TCAD tools have been increasingly applied to organic electronics since accurate results can be obtained in reasonable simulation times, i.e. if compared for instance to a MC approach. A survey on the application of those tools to conventional organic devices as Organic Light Emitting Diode (OLED) and Organic Photovoltaic (OPV) is reported. In most cases, OSC models employed in TCAD simulations should be adapted in order to be introduced into existing commercial software. This is highlighted for the materials of interest in this thesis.

In Chapter 3, the application of TCAD tools to the analysis of Organic Field-Effect Transistors (OFETs) based on Bulk Heterojunction (BHJ) semiconductors is demonstrated. This class of materials is crucial in the operation of organic optoelectronic devices and its properties can be evaluated using OFETs as a testbed. The transistors are analyzed in terms of current and admittance, the latter measured by spectroscopy techniques, in order to evaluate the influence of the dielectric layer of the transport properties. The experimental curves are confronted with empirical models to perform a first-hand estimation of important quantities such as field-effect mobility and cut-off frequency. Then, TCAD simulations are employed to lay a physical-based framework on the interpretation of the results and refine the estimations with the application of accurate models. This analysis shows how traps present at the semiconductor-dielectric interface negatively influence performance, affecting the subthreshold swing and the cut-off frequency of the OFET. In particular, the latter also deviates from the expected voltage-dependent behavior, implying the threshold voltage changes as traps influence the interface potential.

In Chapter 4, the application of TCAD tools to the design of Vertical Organic Transistors (VOTs) is demonstrated. In particular, their use as OPTs is evaluated. The VOT has been identified as a promising technology to overcome planar transistor limitations, as the channel length of this device can be controlled with nanometer precision without restoring to sub-μm structuring techniques. Furthermore, the vertical process flow can be better upscaled and integrated with other devices such as OLEDs and OPDs, leading to transistors with high current densities and a large sensitive area. As a result, they are considered more suitable to be applied as OPT if compared to conventional planar devices. To this purpose, a TCAD simulation-based comparative study of vertical and planar OPTs is performed, highlighting commonalities, strengths and weaknesses of both devices from an electrical and optical point-of-view. In particular, it is found the vertical OPT is characterized by an higher efficiency since its structure is more inclined to collect photogenerated carrier with respect to the planar one. The performance of the vertical OPT can be improved as TCAD tools can be employed to evaluate new transistor structures. In this regard, it is shown how the electrical and optical responses of the device are improved by changing the gate architecture.

In Chapter 5, the TCAD methodology is exploited for the implementation of a Polarized Organic Photodiode (POPD) – a novel photodiode architecture in which the photocurrent is sensible to the incident light polarization. This is achieved by integrating a Wire Grid Polarizer (WGP) into a conventional OPD based on BHJ semiconductors. This concept demonstrates the potential of organic electronics, in which modular designs can be realized exploiting native compatibilities of processes and materials in order to create room for new applications, as the POPD can be employed in Lab-on-a-Chip (LoC) systems to overcome current state-of-the-art limitations. The performance of the POPD are first evaluated using numerical simulations based on established models, in order to asses if performance are suitable for LoC applications. A proof-of-concept implementation of the POPD is then realized based on the simulations outcome. The collection of the device response allows for feedback introduction into applied numerical models, in order to gain insights related to device behavior. Although performance of the POPD implemented using this methodology can be considered reasonable, it is found that more accurate models are needed to correctly describe the device mechanisms. To this extent, an approach based on simulations of the BHJ morphology using spin exchange algorithms is proposed to overcome some of these limitations.

In synthesis, this work describes a complete framework in which organic electronics models are integrated with existing numerical simulation software to study organic optoelectronic devices. Technological feedback and the application of computer-based tools is very important nowadays, since it allows for a reduction of the experimental effort due to the identification of factors limiting device performance. This results in a reduced time-to-market, which is of great interest for industrial production. It is our opinion this approach will set the basis for a better exploitation of the organic technology in the near future. With this work, we are aiming to demonstrate that commercial TCAD tools can be conveniently applied and modified for the analysis, design and implementation of novel organic electronic devices, such as VOTs and POPDs, paving the way to the development of new applications in the multifaceted shades of organic electronics.

Chapter 1
Organic Electronics

1.1 Introduction

Organic electronics rely on the exploitation of molecules and polymers with semiconducting properties, i.e. absorption and emission of light in the visible spectral range and a degree of conductivity that is sufficient for the operation of classical semiconductor devices, such as diodes and transistors. Even though this field has expanded considerably in the industrial and academic world in recent years, its roots go back to the study of molecular crystals, which took place from 1950 to 1980. Interest in those materials gained momentum from the report of electroluminescence in an anthracene crystal (Helfrich and Schneider (1965, 1966); Pope et al. (1963)). Unfortunately, molecular crystals are brittle and require a certain minimum thickness in the range of a few micrometers to achieve mechanical stability. This implies the electric field needed for charge injection and conduction can only be obtained by applying a few hundred volts across the crystal slice, which is not suitable for any consumer application.

The first commercial exploitation of organic electronics lies in the field of Molecularly Doped Polymers (MDPs). When companies such as Xerox and Kodak investigated materials that are suited as photoreceptors for electrophotography in the mid-1970s, it was noted that the until hen used inorganic chalcogenides could be replaced profitably by a few nanometers thin-film of MDP. The application of xerography requires a material that has a very low dark conductivity, yet a reasonable photoconductivity. This is well fulfilled by MDPs, which consist of an inert polymeric binder material that is doped with an optically active molecule. Moreover, MDPs have the advantage of being nontoxic and easy to process, and for this reason they are still used in every common photocopying machine today (Köhler and Bässler (2015)).

The technological development of organic electronics took off with the discovery of electroluminescence in amorphous organic films, as Tang and VanSlyke (1987) reported the first vacuum-deposited Organic Light Emitting Diode (OLED) based on the molecule Alq$_3$ having an external quantum efficiency of 1$\%$. This was followed by Burroughes et al. (1990), who reported the first solution-processed OLED based on the π-conjugated polymer PPV operating at voltages below 14 V. The success of the OLED technology was made possible by the possibility of creating thin films with thicknesses in the order of 100 *nm* to allow low energetic budgets to be employed in fabrication, devices with low operating voltages and – still – acceptable performance with a huge margin for improvements. By today, OLEDs have been exploited in organic displays (Steudel et al. (2012)), lighting panels (Reineke et al. (2009)) and successfully employed in consumer applications by LG and Samsung. This success has stimulated the creativity of the academic world towards the creation of novel devices, their exploitation in new and transversal applications (Nau et al. (2015)) as well as increasingly integration with high-volume manufacturing technologies (Kong et al. (2014)).

However, most of the theoretical understanding on the behavior of Organic Semiconductor (OSC) has been transferred from early fields – as that of molecular crystals and MDPs – into the study of amorphous thin films, as the notions charges move by hopping between molecules at room temperature and optical excitation creates a coulomb-bound electron-hole pair that may move through the material. The observed electroluminescence in OLEDs – and later any related electronic property such as field-effect mobility in transistors or photoconductivity in solar cells structures – was interpreted using elements derived from early studies on organic electronics (Schwoerer and Wolf (2007)). The huge technological expansion of the latest years demands for a more consistent mathematical description of organic electronics which can be applied to device analysis and design from a computer-based point of view. This chapter introduces basic concepts governing organic electronics physics and gives a brief survey on the main approaches used in the literature to study those kind of devices with numerical techniques.

1.2 Organic Semiconductors

OSCs are materials mostly made up by Carbon atoms that show properties typically associated with semiconductors. Most of these properties go all the way back to the hybridization of Carbon atoms. In some cases, when Carbon atoms approach as binding partners, the concomitant external forces compensate the energy difference between $2s$ and $2p$ orbitals in order to mix them and form energetically equivalent states.

When two atoms form a bond, atomic orbitals interact with each other to form molecular orbitals. These can be distinguished in σ-orbitals, which are characterized by a strong electronic density on the molecular axis, and π-orbitals, which are characterized by an electronic density off the molecular axis. The energies of molecular orbitals can be approximated with a Linear Combination of Atomic Orbitals (LCAO), which predicts the presence of lower and upper energy molecular orbitals. The latter is usually referred to as anti-bonding orbital and it is denoted by an asterisk. In this process, since the contributions from atomic orbitals of different energies is small due to a limited contribution of the overlap integral, it is sufficient to only consider the mutual interaction of orbitals at equal or similar energy (Atkins and Friedman (2011)).

When the atomic orbitals in Carbon are partially hybridized, the resulting molecule is characterized by π-bonds. In the Ethylene molecule, which is often considered as an example, the Carbon atoms are characterized by a $2sp^2$ hybridization of the outer shell, i.e. the $2s$ orbital is mixed with only two of the $2p$ orbitals. In the bonding process, the $1s$ orbitals of Carbon atoms are close to the core with negligible interaction, forming σ- and σ^*-orbitals with only little splitting between them. The three $2sp^2$ hybrid orbitals points along their internuclear axis with a large amount of charge overlap located between the nuclei, leading to a large interaction originating σ- and σ^*-orbitals that are pushed far apart. On the contrary, the interaction of the non-hybridized $2p_z$ orbitals takes place at some distance from the nuclei, and thus results in a weaker splitting between the π- and π^*-orbital. These concepts are shown in fig. 1.

The $1s$-orbitals each contribute with two electrons, which are accommodated in the inner shell σ and σ^*. The electrons contained in each of the three $2sp^2$ hybrid orbitals are used to fill the outer shell σ, leaving the anti-bonding σ^* at high energy empty. This leads to a strong net attractive interaction between the nuclei involved, which keeps the molecule together. The two $2p_z$ orbitals each contain one electron to be accommodated, filling the π-orbital and leaving the π^* empty. In contrast to the σ-orbital, the π-orbital contributes only little to the attractive force between the nuclei, since the overlap electronic density is further away from the internuclear axis, which is reflected in the lower splitting between π- and π^*-orbitals compared to the outer shell σ and σ^*. As a result, the π- and π^*-orbitals form the Highest Occupied Molecular Orbital (HOMO) and the Lowest Unoccupied Molecular Orbital (LUMO)

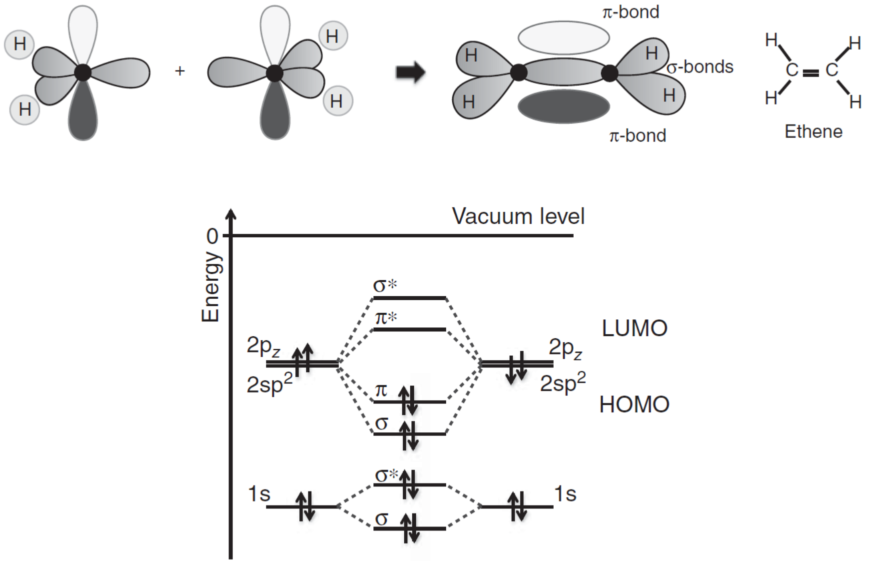

Figure 1: *The Ethylene molecule showing the concept of molecular orbitals. Adapted from Köhler and Bässler (2015).*

– which are also called frontier orbitals – of the Ethylene molecule (Köhler and Bässler (2015)).

The ability of a molecule to take part in electronic processes such as charge transport and light absorption depends on the HOMO and LUMO energy levels of the frontier orbitals. For instance, a charge carrier injected from an electrode to the molecule will go to occupy the LUMO level. Similarly, the extraction of a charge carrier from the molecule corresponds to taking an electron out of the HOMO. Moreover, the charge carrier can be either electron or hole, depending on the relative position of the frontier orbitals and the electrode workfunction. When the HOMO and the LUMO are formed by σ- and σ^*-orbitals the charge injection from electrodes into the molecule results difficult, since these orbitals are placed at fairly low and high energies. Similarly, light absorption occurs in the ultraviolet spectral range. On the other hand, the frontier orbitals are placed in the range of typical metal workfunctions when they are π and π^* due to a moderate amount of splitting, allowing for charge carriers injection and absorption in the visible range to take place.

Molecules that are formed by hydrocarbons with alternating single and double bonds are called π-conjugated systems, and are at the basis of organic electronics. The discovery and development of these systems was rewarded in 2000 with the Nobel Prize in Chemistry (Chiang et al. (1977); Heeger (2001)). When those materials are employed to form a thin amorphous film, a large number of atomic orbitals overlap giving birth to quasi-continuum bands, with an energy gap arising between π- and π^*-orbitals due to the Pauli's exclusion principle. However, differently from inorganic semiconductors – where lattice periodicity originates Bloch waves that are responsible for electron delocalization in the entire crystal – π-conjugated molecules are held together by weak interaction forces (i.e. Van Der Waals dipoles), and delocalization of electrons due to π-orbitals only happens to a restricted group of atoms. In this case, bands are originated from disorder, i.e. incoherent bands, and the mechanisms underlying OSCs operations are different and peculiar to this class of materials (Caserta et al. (1969); Lanzani (2012)).

1.2.1 Charge Transport

As said, OSCs mostly present in the form of amorphous thin films, i.e. disordered media that are nevertheless capable of conducting an appreciable current. A variety of approaches have been proposed over the years to describe charge transport in OSCs, with lively debates on the correctness of each still going on today in the academic world. However, in order not to be lost in the maze of models proposed in the literature, the underlying assumptions for each approach shall be considered, since a model no longer works only when brought out of contest (Tessler et al. (2009)).

As in OSCs bands are originated from disorder, charge transport may be in principle considered as an hopping process from a localized state to another. In other words, the electrical currents observed in thin films of an OSC are attributable to electron transfer between adjacent molecules. The rate at which this process occur is related to the semiconductor conductivity, and can be described through eq. (1).

$$\frac{\partial f_i}{\partial t} = -\sum_{i\neq j} w_{ij} f_i(t)[1-f_j(t)] + \sum_{i\neq j} w_{ji} f_j(t)[1-f_i(t)] - \lambda_i f_i(t) \tag{1}$$

This can be considered as an hopping master equation in which f_i is the occupation probability for the i-th localized state, t is the time, w_{ij} is the hopping rate from state i to state j and λ_i is the i-th state decay rate (Movaghar et al. (1986); Pasveer et al. (2005)). The hopping rate is usually characterized by the Miller-Abrahams formalism, which describes the hopping process as a phonon-assisted tunneling (Miller and Abrahams (1960)). This is reported in eq. (2), where ν_0 is the phonon frequency (i.e. the hop attempt rate), η is the inverse localization radius of the electron wavefunction [1], r_{ij} the distance between states i and j, $\Delta\varepsilon_{ij}$ is the energy difference between states i and j, k_B is the Boltzmann constant and T is the temperature.

$$w_{ij} = \nu_0 \exp\left(-2\eta \left|r_{ij}\right|\right) \begin{cases} \exp\left(-\frac{\Delta\varepsilon_{ji}}{k_B T}\right) & \Delta\varepsilon_{ij} > 0 \\ 1 & \Delta\varepsilon_{ij} \leq 0 \end{cases} \tag{2}$$

Intuitively, the Miller-Abrahams rate express the fact an electron may hop between two localized states if these are close enough in space and/or energy, being the process driven by phonon availability. The formalism contained in eqs. (1) and (2) needs to be solved, being a non-linear set of equations of potentially extremely high number of terms. Moreover, assumptions have to be made for what concern the physical distribution of localized band states in space and energy. The above equations have sprouted into a number of semi-phenomenological models for OSC conductivity, form Variable Range Hopping (VRH) (Mott (1968)) to percolation theory (Ambegaokar et al. (1971)). The most popular in the organic electronics community is probably that proposed by Bässler (1993), which numerically solved the master equation for a system in which the localized band was characterized by a non-uniform Density Of States (DOS) of Gaussian shape. This model has been expanded over the years and has been employed to successfully explain a series of different physical phenomena, such as temperature- and bias-dependent mobilities (Vissenberg and Matters (1998)).

However, with the advance of technological processes and the synthesis of high-performing OSCs, a modified approach based on band theory has been increasingly exploited by many to describe OSCs physics. In particular, this has been framed in the picture of the so-called Multiple Trapping and Release (MTR) model, in which the current is determined by delocalized bands and significantly influenced by localized states acting as trapping sites – as initially derived for amorphous Silicon (Shur and Hack (1984)). As for hopping-based models, MTR has proven to be successful in describing the behavior of materials and devices, with a broad spectrum of physical phenomena and devices accounted for. For example, a temperature-dependent mobility is originated since the ratio of trapped and free charge is dependent upon temperature

---

[1] The inverse localization radius η comes from the quantum mechanical description of the problem, being related to the overlap integral of electron wavefunctions assuming an exponential decay with distance

at the thermal-equilibrium. Similarly – since traps are usually distributed in energy – a bias-dependent mobility results from the effect of bias and associated Fermi-level shifts on traps occupancy (Horowitz et al. (1995)). As time and debate goes by, a band-theory approach seems reasonable to many researchers since it is better suited to describe the very high mobilities of modernly engineered OSC with respect to hopping/percolation theory. For instance, hopping has difficulties in explaining the broad mobility variation obtained in some materials (e.g. Pentacene) upon different processing conditions, while this is straightforwardly embedded in the MTR model, where it only takes to tune the trap concentration (Stallinga (2011)). The main models employed in the description of OSCs through band theory are the subject of Chapter 2, as this is the main approach employed in the present dissertation. However, it is worth noting that one approach does not necessarily rule out the other. This concept can be summarized in fig. 2.

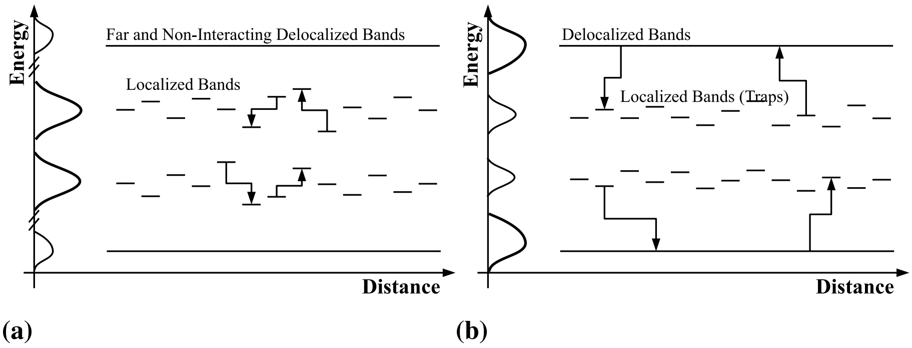

Figure 2: *Charge Transport: a) hopping picture, b) MTR picture.*

Depending on the degree of conductivity of the considered OSC, hopping and MTR theories can be both applied successfully and unified in principle. As a general rule-of-thumb, hopping theory rules out delocalized transport only insofar the dominating mechanism is the conduction through localized states bands, i.e. delocalized bands are far in energy and non-interacting with localized states. In MTR, the interaction of delocalized bands with localized states cannot be longer neglected, the latter acting as trapping sites. Moreover, all degrees of conductivity can be in principle described using an hybrid approach based on the combination of hopping and MTR theories.

1.2.2 Light Absorption

OSCs have been attracting ever increasing interest due to their outstanding optoelectronic properties. Their high absorption coefficient in the visible range of the electromagnetic spectrum has been successfully exploited in Organic Photovoltaic (OPV) and photodetectors.

Photons impinging on an OSC generate excitons, i.e. neutral excited molecular states in which an electron is bound to an hole with a binding energy of few hundreds *meV* (Kippelen and Brédas (2009)). The relatively strong exciton binding energy prevent the spontaneous dissociation of excitons into free charge carrier pairs, conversely to inorganic semiconductor – where the binding energy is small due to the relatively high dielectric constant. As a result, exciton dynamics becomes important in OSCs, as photogenerated excitons move by diffusion following hopping mechanisms, with typical diffusion lengths in the order of 10 *nm*, and may be subjected to quenching, i.e. due to non-radiative decay to the ground state. To avoid losses, an electric field should be applied to effectively dissociate the exciton into an electron/-hole pair, opposing the potential barrier that separates the bound and unbound states. Photogeneration in pristine OSCs is poorly to mildly efficient and rather impractical, as it strongly depends on the availability of excess energy supplied by the external electric field.

The quantum yield of an OSC can be enhanced introducing donor/acceptor interfaces, i.e. junctions formed between molecules that posses low ionization potential (donors) and high electron affinity (acceptor). An exciton reaching a donor/acceptor interface decays into a Charge Transfer (CT) state having the electron on the LUMO of the acceptor and the hole on the HOMO of the donor. In the CT state the electron/hole pair is less bound by Coulomb interaction since the difference in the energetic levels of the donor/acceptor couple accounts for some of the exciton binding energy. In addition, the exciton/CT decay is very competitive with respect to quenching mechanisms, since it occurs on a fs timescale (Baeg et al. (2013)).

High photogeneration quantum yields require an high degree of intermixing between the donor and acceptor phases, while the separated electron/hole couple collection requires the continuity of the phases themselves. From a device point of view, one of the most adopted solutions is the so called donor/acceptor Bulk Heterojunction (BHJ), where the two phases are blended together to form an intertwined morphology, effectively distributing donor/acceptor interfaces in the bulk of the OSC (Brady et al. (2011)). In this case, the donor/acceptor morphology has a critical impact on device performance.

Two scenarios have been proposed to explain why free charge generation at donor/acceptor interfaces is an efficient process. The first one link the effect of interface dipoles, entropy, disorder and external electric fields to the binding energy of the ground CT state (Deibel et al. (2010)). The second scenario considers the formation of hot CT states, which are more spatially extended than ground CTs, leading to a smaller binding energy of the electron/hole couple (Grancini et al. (2013)). To profit from the latter mechanism, the energy difference between the acceptor LUMO and the donor HOMO should be maximized. This can have a negative impact on OPV due to a drop of the open circuit voltage. In Organic Photodiodes (OPDs) and Organic Phototransistors (OPTs) this effect can be instead be beneficial, since the voltage is applied from an external source and the focus only resides on the current output due to light excitation.

1.2.3 *Light Emission*

OSCs are also capable to effectively emit light, as demonstrated by the fabrication of OLEDs having efficiencies that reach and surpass that of fluorescent tubes (Reineke et al. (2009)). As for absorption, light emission is mediated by the formation of excitons. However, for the latter is important to discriminate between singlet and triplet excited states [2]. The total spin of an exciton is a linear combination of hole and electron spins, as reported in eq. (3).

$$\begin{aligned} s_1 &= |\uparrow\uparrow\rangle \\ s_2 &= |\downarrow\downarrow\rangle \\ s_3 &= \frac{1}{\sqrt{2}}(|\uparrow\downarrow\rangle + |\uparrow\downarrow\rangle) \\ s_4 &= \frac{1}{\sqrt{2}}(|\uparrow\downarrow\rangle - |\uparrow\downarrow\rangle) \end{aligned} \tag{3}$$

Three of these four possible states have spin equal to one, while the last one has spin equal to zero. An exciton is said to be in the triplet state in the former case (threefold degeneracy), while to be in a singlet state in the latter. Exciton radiative decay is a process for which the spin must be conserved, hence – statistically – only the 25% of created excitons (singlet) can lead to a photon emission. This process is known as fluorescence and OSCs for which this happens are known as fluorescent emitters (e.g. Alq_3). Radiative decay of

---

[2] The rules for spin conservation say that excitons generated by photon absorption are always in the singlet state.

triplet excitons can happen if the considered molecule has a strong spin-orbit coupling, which is usually the case if an heavy metal atom is present in the molecule itself. In this case, singlet and triplet states can undergo Inter-System Crossing (ISC) and their wavefunctions can mix in a way to allow radiative decay, generally speaking, by the whole excitonic brood. Emission from the triplet state is named phosphorescence and OSCs for which this happens are known as phosphorescent emitters. In this regard, the most efficient emitters are based on Iridium, as this compounds are subject to a very strong spin-orbit coupling – i.e. efficiencies close to the theoretical limit of 100% – spanning the whole visible spectrum with red (e.g. Ir(MDQ)$_2$), green (e.g. Ir(ppy)$_3$) and blue (e.g. FIrpic) emission. As a matter of fact, they are massively employed in the realization of highly efficient white OLEDs (Reineke et al. (2013)).

1.3 Numerical Methods

This section gives a brief overview of numerical methods employed for OSCs and devices simulations following a bottom-up approach, i.e. going from microscopic to macroscopic methods. The greatest deal of refinements is given when the actual molecular structure is taken into account. This can be performed using atomistic simulations, which solve the quantum mechanical problem on a molecular material to calculate quantities such as wavefunctions, bands and energy levels. Going up, while Monte Carlo (MC) simulations are a set very generic statistical methods that can be applied to the most disparate fields at various levels of refinement, they have been historically employed in organic electronics to build upon the quantum mechanical framework and study electrical quantities in systems which extend in the *nm* range. The term continuum simulations is used to refer in here methods that does not account for the microscopic description of the semiconductor. Continuum simulations mainly fall in the Technology Computer Aided Design (TCAD) framework. To give a complete description of a given problem it is often true that different spacial and energetic scales have to be taken into account. This issue can be faced with multiscale simulations.

The importance of employing numerical methods to the study of organic electronic devices is twofold. To one extent, these methods provide a platform to prove the physics right, i.e. the refinement of existing models and the creation of new ones. This process resides in the device analysis domain, in which simulations are employed to describe a set of experimental data to asses the parameters of a model for a given material or help developing equations for a particular phenomenon. On the other hand, given a set of established models, simulations can be directly applied to device design, e.g. varying geometrical parameters and/or layers distribution, and implementation. This process resides in the device design domain. The two processes are not stand alone, since they can interact through the analysis-design boundary, being their advancement concurrent as technological development goes on. These concepts are shown in fig. 3.

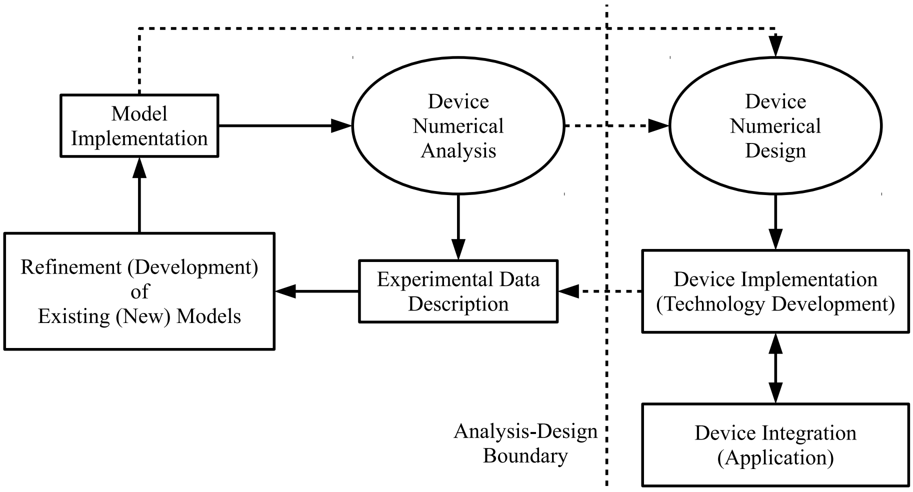

Figure 3: *The numerical methods paradigm in organic electronics.*

1.3.1 Atomistic Simulations

The smallest organic device possible is that formed by a single molecule. Molecular electronics is seen by many as one of the possible candidates to solve the increasingly shrinking down in size of conventional devices [3]. Description of devices behavior at this scale is inevitably involves the application of quantum mechanics first principles, which is often referred to as atomistic simulations.

Atomistic simulations are also useful in conventional device analysis, as there are cases in which quantum-mechanical effects must be accounted for in order to have a correct picture of the device behavior. Atomistic models have been applied to OSC systems in order to calculate material-related elec-

---

[3] Transistors are now reaching the 5 *nm* technology node (Feng et al. (2017)). Approximately 50 atoms of Silicon can be contained in a 5 *nm* length.

trical quantities as the mobility. For instance Kwiatkowski et al. (2008) and Nagata and Lennartz (2008) employed atomistic simulations to study charge transport in Alq$_3$. The first report suggests that transport is dominated by a small number of molecule that creates conductive pathways. In addition, the authors predict electron mobility is higher than hole mobility due to a greater LUMO delocalization with respect to the HOMO's. The second report associates the Poole-Frenkel (PF) mobility that is often observed in organic devices to the energetic disorder of the material and to randomly meshed molecular connectivity. Atomistic models have also been applied for the sake of thorough OLED simulations (Kordt et al. (2015)).

The atomistic approach invariably take into account a great deal of details and demands a huge request of computational resources. In addition, when applied with the aim of upscaling models to conventional devices size, they are used in conjunction with MC or other solving methods in order to calculate the electrical quantities of interest. For these reasons, atomistic simulations are relied to only when a complete quantum-mechanical description of the problem is absolutely necessary to assess a clear picture of the experimental background at hand.

1.3.2 Monte Carlo Simulations

The Monte Carlo is a statistical method based on the selection of random numbers, which was first applied in semiconductor device simulations by Kurosawa (1966). The motion free charge carriers under the influence of external forces, e.g. electrical bias, is influenced by various phenomena which are due to the surrounding semiconductor medium. Those phenomena – i.e. scattering, collisions, radiative/non-radiative decay, etc. – are characterized in terms of probabilities. As simulation time goes by, the MC method stochastically select one of this events based on these probabilities to determine carriers trajectories and hence macroscopic quantities as device current. The results obtained with a MC procedure are never exact, but rigorous in a statistical sense, i.e. the exact result lies in given intervals with given probabilities. The uncertainty is strictly related to the variance of possible outcomes and it is smaller if the amount of computations devoted to the solution of the problem is larger. MC calculations can be considered as a simulated experiment, as the final results must be interpreted to in physical terms in order to obtain a better understanding of the problem at hand (Jacoboni and Lugli (2012)).

The MC method has been initially used in simulations of organic devices and systems because it well suited the description of charge transport in terms of hopping on a randomly disordered structure. In this regards, it was used by Bässler (1993) for the derivation of the Gaussian Disorder Model (GDM) and mostly applied later on for the simulations of various transport problem from the study of metal-organic interfaces (Scott (2003); Wolf et al. (1999)) to current-voltage relationships in OLEDs (Walker et al. (2002)) and the derivation of carriers mobility in OFETs (Sharma et al. (2011)). More recently, MC simulations have become the preferred method to study BHJ solar cells, as they have been employed to asses the dependence of the efficiency upon the blend morphology Albes et al. (2016); Watkins et al. (2005) and the effect of electrostatic interaction (Casalegno et al. (2010)).

The MC method is an extremely valuable tools to study the properties of those systems, yielding insights on device behavior, but it suffers from a massive request of computational resources and is usually slow even when optimized – especially if compared to continuum simulations. For this reason, its applicability is limited to small domains and MC simulations are difficult to be upscaled and employed in a commercial environment for full device analysis and design.

1.3.3 Continuum Simulations

In organic electronics, continuum simulations are mostly performed through TCAD tools. Historically, TCADs have been developed for inorganic electronics to enable in technology the advances that Moore's Law has driven in computing power and data transformation. They play an essential role in achieving both flexibility and simplicity, which are exploited to carefully assess the implication of technological parameters on design rules, allowing developers and circuit/device end-users to communicate and optimize performance and production objectives. Nevertheless, it is indeed true that semiconductors are quite old [4], and – as this stands – TCAD can be considered a relatively young since the history of using computers to design technology started somewhere in between 1960 and 1970, with one the first papers published in 1986 (Law (2016)). Being OSCs the guinea pigs of the new wave of electronics, the ap-

---

[4] The first to notice a physical effect due to semiconducting properties was Thomas Johann Seebeck in 1821 (Velmre (2007)). The first application of semiconducting materials in electronics can be traced back in 1906 when the American Brigadier General Henry Harrison Chase Dunwoody signed a patent for a Silicon Carbide steel detector to be used in crystal radios (Lee (2007)), while the operations of the first transistor were demonstrated in 1948 by Bardeen, Brattain and Shockley (Bardeen and Brattain (1948); Shockley (1976)).

plication of TCADs to this field can be considered a baby born. At the current state-of-the-art, commercial tools integrate inorganic semiconductor models with the most relevant related to the organic world. The aim of this dissertation is to assess the applicability of commercial TCADs to novel organic devices, in order to highlight current capacity and limitations. A more detailed description of the TCAD framework and its application to organic electronics is given in Chapter 2. In here, a typical simulation flow is highlighted, as shown in fig. 4.

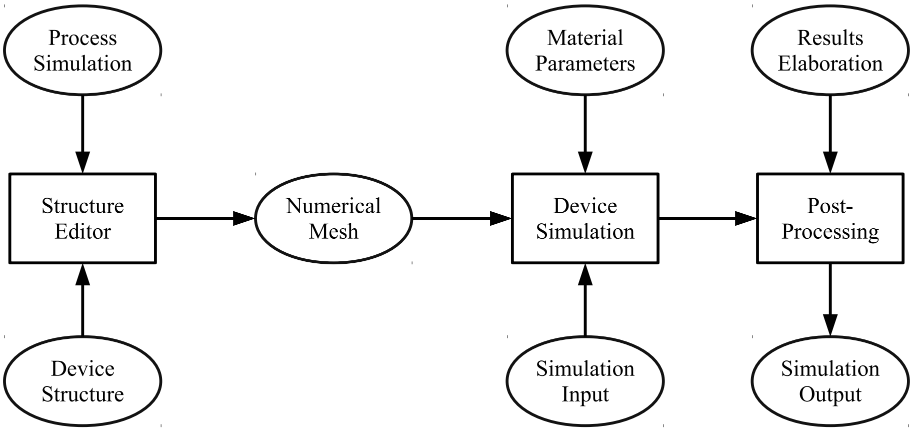

Figure 4: *A typical simulation flow in TCADs.*

This follows in a modular fashion as the process is broken in various step. First, the device structure on which device simulations is to be performed is built through process simulation and/or direct specification. The device space is then discretized in order to obtain the numerical mesh. This is fed to the device simulator, along with material parameters and the definition of the optoelectronic problem. The device simulator output is then given as input to post-processing tools in order to obtain the final output in terms of graphs or derived quantities. The steps inside a TCAD simulation can be combined customary to allow for a great degree of flexibility and the need of different user applications. In addition, wrapper scripts for automated execution and continuous integration needs can be applied in order to speed up the development process.

TCAD tools have proven over time to be the optimal solution in terms of simulation yield and have a successful history in industrial environments. However, the continuum description of the problem may produce inaccurate results and fail to model phenomena taking place at the microscopic scale, which other techniques, e.g. the MC method, are better suited to describe.

1.3.4 Multiscale Simulations

All the simulation methods highlighted before present strengths and weaknesses basically due to the degree of details that are taken into account. Atomistic simulations directly applies quantum-mechanics first principles to carefully describe molecules interaction. This is pretty accurate in retrieving fundamental quantities but only suitable to describe molecular materials, i.e. below the *nm* range. MC simulations apply probability rates derived from first principles to statistically calculate the mobility of an OSC layer or the current flowing in simple devices. This method usually applies to the *nm* range and is difficult to upscale towards more complex systems, but has proven a extremely valuable tool in study on nanostructured devices as BHJ solar cells. Continuum simulations collocate themselves in the TCAD framework, which follows the band structure-picture approximation. This method is capable of describing a whole device or a small system in the range of μm, but fails to describe peculiar effect due to the microscopic arrangement of the OSC. Indeed, the trend to scale down device dimensions is hindering the possibility to satisfactorily approach an electronic problem using only one of these scales, especially in organic electronics where engineers have to deal with molecules and microscopic systems in the first instance.

To solve this issue, it is possible to resort to multiscale simulation techniques. Multiscale simulations combine the quantum mechanical and semiclassical approaches, involving two or more coupled models that resolve on different spacial or energetic scales (Auf der Maur et al. (2011)). Here, the mathematical formulation of the problem is accommodated to suite each of these scales. Multiscale simulations have been applied to BHJ OPV by de Falco et al. (2012), in which a micro- and a macro-scale are considered. The micro-scale provides a full description of excitation, transport, dissociation and recombination phenomena occurring at semiconductors interface. The macro-scale is obtained from the micro-scale by averaging the considered equations across the interface region, giving rise to nonlinear transmission conditions that are parametrized by the interfacial width. Using this approach, the authors have performed extensive numerical simulations of realistic device structures.

1.4 Conclusion

This chapter deals with basic concepts that are foundation for the following ones. First of all, the organic electronics framework is introduced. Organic Semiconductors are made by molecules and the electronic structure is different to that found in inorganic crystals as Silicon. As a consequence, the physics of those materials is peculiar and device description follow behind specific models that have been borrowed from studies of conductivity in low-mobility systems. Charge transport have been historically described using an hopping approach, where charge carriers jump from a molecule to another using a phonon-assisted tunneling mechanism. While this picture hold strong as today, organic electronics researchers have also applied a modified version of band theory – namely the Multiple Trapping and Release approach – to better suit the needs of describing modernly engineered materials, where relatively high mobilities are reached. Due to the low Coulomb screening in Organic Semiconductors, carrier-carrier interactions become important and mechanisms like light absorption/emission are governed by the formation of excited states where electrons and holes are bound together. The exciton dynamics need to be considered in describing the operations of organic devices, despite the fact conventional methods can be applied to have a first estimate of device behavior. Due to the complexity of the problem, numerical methods are necessary to thoroughly study organic devices and contribute to the advance of technology. The importance of employing numerical methods to the study of organic electronic devices is twofold. To one extent, these methods provide a platform to prove the physics right, on the other hand simulations can be directly applied to device design and implementation when a set of models is established. The main numerical methods employed in organic electronics have been briefly reviewed, being them atomistic, Monte Carlo, continuum and multiscale simulations. The application of continuum simulation to the analysis, design and implementation of novel optoelectronic organic devices is the subject of this thesis.

Chapter 2
Technology Computer-Aided Design

2.1 Introduction

Despite being a relatively new field, organic electronics has demonstrated devices and materials with appealing features in various applications – from analog and digital circuits to bioelectronics – to the point of being successfully exploited in commercial products as, for instance, Organic Light Emitting Diode (OLED) displays.

Although studies have flourished during the years, a real improvement in devices and materials performance is subordinate to the deep understanding of the underlying physical mechanisms and their connections to design-relevant parameters. At this purpose, the use of numerical simulations has been considered of foremost importance for the development of consistent mathematical models, which are helpful in identifying and overcoming technology-limiting factors.

This chapter deals with the application of Technology Computer Aided Design (TCAD) tools to organic electronics. A TCAD is a computer-based simulator capable of systematically integrate the various physical phenomena contributing to the behavior of a semiconductor device. Numerical models are provided as sets of non-linear Partial Differential Equations (PDEs) in order to mathematically describe fabrication processes and semiconductor operations. PDEs are then transformed into difference equations using a spatial discretization scheme and solved using iterative algorithms based on the Newton's method, usually leading to reliable results in a reasonable simulation time.

The analysis that follows gives an introduction to TCAD and a general description of numerical methods used in state-of-the-art software. Although these methods have been primarily developed for Silicon, they remain still valid to a certain degree of approximation in describing the behavior of Organic Semiconductors (OSCs). The extent of the implications relevant for this class of materials is also considered here.

The commercial TCAD Sentaurus©(Synopsys (2015)) will be taken as reference during the discussion, as it is used for all the simulations contained in this thesis.

2.2 Semiconductor Equations

Semiconductors behavior is generally described with a set of non-linear PDEs modeling electrical and optical properties. Those models have been developed in first instance for inorganic semiconductors and are framed within the band structure picture (Shur (1990)). Since organic materials present their peculiarities with respect to inorganic semiconductors, conventional equations need to be conveniently modified in order to take into account OSC properties. In the following, models derived from band theory and used to describe semiconductors behavior in TCAD are introduced, highlighting the most important modifications due to the organic framework.

2.2.1 Electrostatic Potential

The electrostatic potential is a key observables for what concern the electrical behavior, since it is responsible for charges motion in a device. The electrostatic potential is a solution of the Poisson's equation and it is determined by the charge distribution itself. This is formed by both mobile (i.e. holes and electrons) and immobile charges (i.e. dopants, traps).

The Poisson's equation is reported in eq. (4), where ε is the absolute dielectric constant, ψ is the electrostatic potential and ρ is the charge density. The latter is contributed to by free electron and hole concentrations (n and p), ionized donor and acceptor concentrations (N_D and N_A) and trapped charge density (ρ_{trap}). Note that q is the elementary charge.

$$\nabla \cdot (\varepsilon \nabla \psi) = -\rho = -q(p - n + N_D - NA) - \rho_{trap} \tag{4}$$

The free electron and hole concentration is computed as in eqs. (5) and (6), for the general case in which the Fermi statistics is employed. Here, N_C and N_V are the conduction and valence band effective Density Of States (DOS), $F_{1/2}(x)$ is the Fermi integral of order $1/2$ [5], $E_{F,n}$ and $E_{F,p}$ are the quasi-Fermi

---

[5] Note that this reduces to the exponential function when the Boltzmann statistics is used.

levels for electrons and holes, E_C and E_V are the conduction and valence band edges.

$$n = N_C F_{1/2}\left(\frac{E_{F,n} - E_C}{k_B T}\right) \tag{5}$$

$$p = N_V F_{1/2}\left(\frac{E_V - E_{F,p}}{k_B T}\right) \tag{6}$$

For non-doped semiconductors electrons and holes are present in equal quantity. This is indicated as intrinsic free charge carrier concentration n_i [eq. (7)] and it is only dependent on the semiconductor bandgap E_G. In addition, the relation $np = n_i^2$ always holds at thermodynamic equilibrium for a generic doping level.

$$n_i = \sqrt{N_C N_V}\exp\left(-\frac{E_G}{2k_B T}\right) \tag{7}$$

The conduction and valence band edge are related to the electrostatic potential as in eqs. (8) and (9), where χ is the electron affinity.

$$E_C = -\chi - q\psi \tag{8}$$

$$E_V = -\chi - E_G - q\psi \tag{9}$$

A Gaussian DOS is often considered for OSCs to model the energetic disorder of localized states, assuming they have random energy around the nominal LUMO or HOMO levels. This is know as Gaussian Disorder Model (GDM) and has been derived empirically by Bässler (1993). The GDM has proven its numerical accuracy in MC simulations and has been further refined over the years to improve the description of mobility dependence over temperature and electric field (Bouhassoune et al. (2009); Pasveer et al. (2005)).

Similarly, the GDM results useful in TCAD simulations since it leads to refined equations for n and p calculation. The GDM DOS – g_n and g_p – are reported in eqs. (10) and (11), where E_{LUMO} and E_{HOMO} are the LUMO and HOMO energy levels, N_{LUMO} and N_{HOMO} the total number of hopping sites and σ_n and σ_p the energy spreading [6].

$$g_n(E) = \frac{N_{LUMO}}{\sigma_n\sqrt{2\pi}}\exp\left[-\frac{1}{2}\left(\frac{E - E_{LUMO}}{\sigma_n}\right)^2\right] \tag{10}$$

---

[6] This is opposed to $g_{n,p} \sim \sqrt{E}$ as employed for inorganic semiconductors, from which eqs. (5) and (6) are derived

$$g_p(E) = \frac{N_{HOMO}}{\sigma_p\sqrt{2\pi}} \exp\left[-\frac{1}{2}\left(\frac{E - E_{HOMO}}{\sigma_p}\right)^2\right] \tag{11}$$

Based on the GDM, Paasch and Scheinert (2010) have derived an analytical expression for free charge carrier concentrations. This has been calculated using an approximation of the Fermi-Gauss integrals, yielding to eqs. (12) and (13).

$$n = G\left(-\frac{E_{LUMO} - E_F}{kT}, \frac{\sigma_n}{kT}\right) \tag{12}$$

$$p = G\left(-\frac{E_{F}{-}E_{HOMO}}{kT}, \frac{\sigma_p}{kT}\right) \tag{13}$$

The function G is reported in eq. (14), where H and K functions are shown in eqs. (15) and (16) respectively.

$$G(\zeta, s) = \begin{cases} \frac{exp\left(\frac{s^2}{2}+\zeta\right)}{1+exp(K(s)(\zeta+s^2))} & \zeta \leq -s^2 \\ \frac{1}{2}\,\mathrm{erf}\left(-H(s)\frac{\zeta}{s\sqrt{2}}\right) & \zeta > -s^2 \end{cases} \tag{14}$$

$$H(s) = \frac{\sqrt{2}}{s}\,\mathrm{erf}^{-1}\left[\exp\left(-\frac{s^2}{2}\right)\right] \tag{15}$$

$$K(s) = 2 - \frac{H(s)}{s}\sqrt{\frac{8}{\pi}} \exp\left[\frac{1}{2}s^2(1 - H^2(s))\right] \tag{16}$$

In the case of non-degenerate semiconductors, the Maxwell-Boltzmann approximation can be used and the above relations can be simplified. The carrier density versus energy follows the conventional exponential law – with modified expressions for N_C and N_V as reported in eqs. (17) and (18).

$$N_C = \frac{N_{LUMO}}{2} \exp\left(\frac{\sigma_n^2}{2(k_BT)^2}\right) \mathrm{erf}\left(\frac{\sigma_n}{\sqrt{2}k_BT}\right) \tag{17}$$

$$N_V = \frac{N_{HOMO}}{2} \exp\left(\frac{\sigma_p^2}{2(k_BT)^2}\right) \mathrm{erf}\left(\frac{\sigma_p}{\sqrt{2}k_BT}\right) \tag{18}$$

2.2.2 *Carrier Transport*

Currents inside a device can be computed using continuity equations. They are reported in eqs. (19) and (20) for electrons and holes respectively, where J_n and J_p are the electron and hole current densities, R_{net} the net recombination rate and G_{opt} the optical generation rate.

$$\nabla \cdot \vec{J_n} = q(R_{net} - G_{opt}) + q\frac{\partial n}{\partial t} \tag{19}$$

$$-\nabla \cdot \vec{J_p} = q(R_{net} - G_{opt}) + q\frac{\partial n}{\partial t} \tag{20}$$

To result meaningful, currents shall be related to material properties and constants. This is done using carrier transport models. The most popular is the Drift-Diffusion (DD) model by Roosbroeck (1950), which is derived from the Boltzmann Transport Equation (BTE) [7] using the first two momenta. This can be expressed in a generic form that considers quasi-Fermi potentials corrective factors ξ_n and ξ_p [eqs. (23) and (24)], as reported in eqs. (21) and (22) (Synopsys (2015); Windbacher et al. (2011)) [8]. Note that μ_n and μ_p are the electron and hole mobilities, D_n and D_p electron and hole diffusivities.

$$\vec{J_n} = \mu_n n \nabla E_C + D_n(\nabla n - n\nabla \ln \xi_n) \tag{21}$$

$$\vec{J_p} = \mu_p p \nabla E_V - D_p(\nabla p - p\nabla \ln \xi_p) \tag{22}$$

$$\xi_n = \frac{n}{N_C}\exp\left(\frac{E_C - E_{F,n}}{k_B T}\right) \tag{23}$$

$$\xi_p = \frac{p}{N_V}\exp\left(\frac{E_{F,p} - E_V}{k_B T}\right) \tag{24}$$

The diffusivities are usually expressed through the Einstein relation, as in eqs. (25) and (26).

$$D_n = \mu_n k_B T \tag{25}$$

---

[7] The Boltzmann Transport Equation is the semiclassical model for carrier transport, which determines the probability to find an electron with a certain momentum in a point of space and time.

[8] When the Boltzmann statistics is employed, the corrective factors reduce to 1.

$$D_p = \mu_p k_B T \tag{26}$$

The DD model yields reasonable results for low-power density devices, otherwise it is necessary to resume more sophisticated sets of equations like thermodynamic (Wachutka (1990)) and hydrodynamic (Apanovich et al. (1995)) transport models.

Note that for OSCs, mobilities are often expressed as a function of the electric field. In this regard, one of the most used models is the Poole-Frenkel (PF) model (Frenkel (1938)). The PF model lays its framework in a Multiple Trapping and Release (MTR) transport context: high electric fields lower the Coulomb-like barrier offered by the trap to its captive, increasing the probability of charge carrier to escape and contribute the current. The field-dependence of the mobility μ is expressed as in eq. (27) (Riede et al. (2011)), where μ_0 is the low-field mobility, E_A is the trap activation energy and F is the electric field.

$$\mu = \mu_0 \exp\left(-\frac{E_A}{k_B T}\right) \exp\left(\frac{1}{k_B T}\sqrt{\frac{q^3 F}{\pi \varepsilon}}\right) \tag{27}$$

Another electric field-dependent mobility model is the one reported in eq. (28), which will from now on be addressed as Power Law (PL) mobility. Here, μ_0 is the low-field mobility, $F_\perp$ is the normal electric field [9], ζ is the mobility exponent and F_0 is a normalization constant. This is an empirical model based on the observation of a power-law field-effect mobility in Organic Field-Effect Transistors (OFETs), which is attributed to hopping transport in an exponential DOS (Castro-Carranza et al. (2012); Estrada et al. (2010, 2008)). The PL mobility model can be effectively employed in OFET simulations, as will be shown later in Chapter 3.

$$\mu = \mu_0 \left(\frac{F_\perp}{F_0}\right)^{\zeta} \tag{28}$$

2.2.3 Carrier Recombination

The current in semiconductors is determined by two types of carriers – electrons and holes – that can be exchanged between transport bands and interact with each other. Processes that involve the interaction of electrons and

---

[9] For OFET simulation purposes, $F_\perp$ is normal to the insulator/semiconductor interface

holes are called recombination processes. These are usually characterized by a net recombination rate R_{net}, which is the total number of electron-hole couples coming from creation and annihilation.

The Shockley-Read-Hall (SRH) model takes into account electron-hole couple recombination through a trap level in the energy gap of the semiconductor (Hall (1952); Shockley and Read Jr (1952)). The net recombination rate can be expressed as in eq. (29), where τ_n and τ_p are the lifetimes for electron and hole respectively.

$$R_{net} = \frac{np - \xi_n \xi_p n_i^2}{\tau_p (n + \xi_n n_1) + \tau_n (p + \xi_p p_1)} \tag{29}$$

The factors n_1 and p_1 are expressed in terms of the trap energy level E_T and the intrinsic Fermi level $E_{F,i}$ as in eqs. (30) and (31).

$$n_1 = n_i \exp\left(\frac{E_T - E_{F,i}}{kT}\right) \tag{30}$$

$$p_1 = n_i \exp\left(\frac{E_{F,i} - E_T}{kT}\right) \tag{31}$$

The lifetimes can be further expressed in terms of the trap density N_T, electron-hole trap capture cross sections (x_n and x_p) and thermal velocities ($v_{th,n}$ and $v_{th,p}$) as in eqs. (32), (33), (34) and (35). Note that m_n^* and m_p^* denote the electron and hole effective masses.

$$\tau_n = \frac{1}{x_n N_T} \tag{32}$$

$$\tau_p = \frac{1}{x_p N_T} \tag{33}$$

$$v_{th,n} = \sqrt{\frac{k_B T}{m_n^*}} \tag{34}$$

$$v_{th,p} = \sqrt{\frac{k_B T}{m_p^*}} \tag{35}$$

The Langevin model – also called bimolecular – is a band-to-band recombination that directly involves an electron and a hole (Langevin (1903)). The recombination rate is expressed in eq. (36).

$$R_{net} = \frac{q}{\varepsilon}(\mu_n + \mu_p)(pn - n_i^2) \tag{36}$$

The Auger model describes a three particles band-to-band recombination, in which the electron-hole annihilation transfers energy to a second electron that gets excited to the conduction band (Auger (1925); Lochmann and Haug (1980)). This mechanism becomes important at high carrier densities and its recombination rate is given in eq. (37), where Γ_n and Γ_p are the Auger coefficients for electrons and holes respectively.

$$R_{net} = (\Gamma_n n + \Gamma_p p)(pn - n_i^2) \tag{37}$$

Note that the SRH, Langevin and Auger recombination rates are respectively proportional to increasing power of carrier concentration from one to three.

2.2.4 Traps

Traps are spurious energy levels available in the semiconductor bandgap. These are generally employed to macroscopically describe band structure degeneracy in polycrystalline and amorphous semiconductors or to take into account the electrical effect of structural defects in crystalline materials. Traps are generally important in describing semiconductors behavior and are mostly used to fine-tune devices response.

Traps can differently behave with respect to electrons and holes. A trap is called acceptor if uncharged when unoccupied and negatively charged when fully occupied (i.e., an electron trap)., while it is called donor if uncharged when unoccupied and positively charged when fully occupied (i.e., an hole trap). Traps can also be distributed in energy. The most important shapes are Gaussian and Exponential. The expressions of their DOS are reported in eqs. (38) and (39), respectively. Here, E_μ is the mean energy level and E_σ represents the energy broadening.

$$N_{DOS}(E) = N_{DOS}(E_\mu)exp\left[-\frac{(E-E_\mu)^2}{2E_\sigma^2}\right] \tag{38}$$

$$N_{DOS}(E) = N_{DOS}(E_\mu)exp\left(-\left|\frac{E-E_\mu}{E_\sigma}\right|\right) \tag{39}$$

The total trap concentration N_T is simply given by integrating the trap distribution over the bandgap energy range [eq. (40)].

$$N_T = \int_{E_G} N_{DOS}(E)dE \tag{40}$$

The evolution of trapped charge concentration is given by eq. (41) for a single trap level following the principle of detailed balance, where f_n is the electron occupation probability.

$$\frac{1}{q}\frac{d\rho_{trap}}{dt} = \frac{1}{\tau_p}\left[p_1(1-f_n) - pf_n\right] - \frac{1}{\tau_n}\left[n(1-f_n) - n_1 f_n\right] \tag{41}$$

The recombination rate can be found by evaluating the above at the steady-state, which leads to the SRH theory. The recombination rate can be generalized in the case of arbitrary trap distributions (Goudon et al. (2007); Simmons and Taylor (1971, 1975)), even though these gets discretized and usually treated as single levels in numerical simulations.

Recombination-wise, key parameters are the electron and hole capture cross sections x_n and x_p, which determine how well a trap level can capture a free charge carrier. These are generally considered constants, but several model that take into account electric field enhancement (Colalongo et al. (1997)) and trap-assisted tunneling (Hurkx, De Graaff, Kloosterman and Knuvers (1992); Hurkx, Klaassen and Knuvers (1992)) exist. Traps are very important in modeling OSCs in TCAD simulations, as this follows from a MTR transport approach (Stallinga (2011)).

2.2.5 Optical Generation

Semiconductors can interact with light. The term optical generation encloses all the processes that produce electron-hole pairs upon photons absorption. Several numerical methods exist for the computation of the optical generation rate. Besides plane wave propagation (Katsidis and Siapkas (2002)) and direct solution of the Maxwell's equations (Taflove and Hagness (2005)), geometrical optics [10] can also be employed.

In fig. 5 an optical interface between two media with different refractive index n_r is shown.

A ray is impinging upon this interface with incidence angle θ_i, being partially reflected and transmitted with angles θ_r and θ_t. Usually, it is referred to

---

[10] Geometrical optics describes light propagation in terms of rays which approximate the propagation paths.

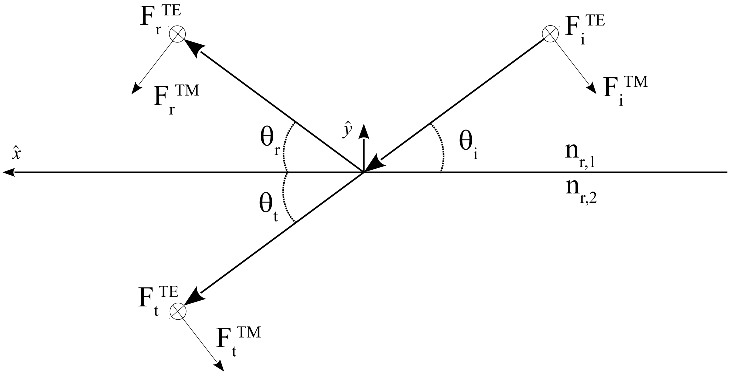

Figure 5: *Impinging, reflected and transmitted rays on an optical interface.*

the electric field polarization as Transverse Electric (TE) or Transverse Magnetic (TM). The electric field vector is transverse to the plane of incidence [11] in the first case, while contained in it in the latter (i.e. the magnetic field is transverse to the plane of incidence). An arbitrary polarization of the electric field can be expressed in terms of TE and TM components.

The electric field magnitude for the reflected and transmitted rays can be determined using Snell's law and Fresnel equations. The resulting reflectance and transmittance coefficients are reported in eqs. (42), (43), (44) and (45).

$$R_{TE} = \frac{\left|F_r^{TE}\right|^2}{\left|F_i^{TE}\right|^2} = \left|\frac{n_{r,1}cos\theta_i - n_{r,2}cos\theta_t}{n_{r,1}cos\theta_i + n_{r,2}cos\theta_t}\right|^2 \tag{42}$$

$$R_{TM} = \frac{\left|F_r^{TM}\right|^2}{\left|F_i^{TM}\right|^2} = \left|\frac{n_{r,2}cos\theta_i - n_{r,1}cos\theta_t}{n_{r,2}cos\theta_i + n_{r,1}cos\theta_t}\right|^2 \tag{43}$$

$$T_{TM} = \frac{\left|F_t^{TE}\right|^2}{\left|F_i^{TE}\right|^2} = \frac{n_{r,2}cos\theta_t}{n_{r,1}cos\theta_i}\left|\frac{2n_{r,1}cos\theta_i}{n_{r,1}cos\theta_i + n_{r,2}cos\theta_t}\right|^2 \tag{44}$$

$$T_{TM} = \frac{\left|F_t^{TM}\right|^2}{\left|F_i^{TM}\right|^2} = \frac{n_{r,1}cos\theta_t}{n_{r,2}cos\theta_i}\left|\frac{2n_{r,2}cos\theta_i}{n_{r,2}cos\theta_i + n_{r,1}cos\theta_t}\right|^2 \tag{45}$$

The light intensity rate I_{opt} can be expressed in terms of the electric field magnitude as in eq. (46), where V is the medium volume, c the speed of

---

[11] The plane of incidence is identified by the vector normal to the optical interface and by the ray trajectory – the x-y plane as shown.

light, ε_0 the vacuum dielectric constant, h the Planck constant and ν the optical frequency.

$$I_{opt} = \frac{cn_r\varepsilon_0}{2Vh\nu}|F|^2 \tag{46}$$

The optical generation rate G_{opt} is reported in eq. (47). Here, $\|r\|$ is the distance between the optical interface and the point in space where the intensity is being evaluated, γ is the photogeneration quantum yield and α_{abs} is the absorption coefficient of the medium.

$$G_{opt} = \gamma I_{opt}[1 - \exp(-\alpha_{abs}\|r\|)] \tag{47}$$

The information needed to calculate optical intensity and generation is summarized in the complex refractive index n_c [eq. (48)]. Here, k is called the extinction coefficient and λ is the optical wavelength. The complex refractive index for a broad range of materials can be usually found in literature in tabular or graphical form as a function of λ.

$$n_c = n_r + ik = n_r + i\left(\frac{\lambda\alpha_{abs}}{4\pi}\right) \tag{48}$$

Computing the optical generation using the complex refractive index and geometrical optics has the benefit of decoupling the electrical and optical problems, that can be solved separately and then combined in a modular fashion.

2.2.6 Boundary Conditions

The electrical problem needs boundary conditions to be solved. These model the effect of electrical contacts as they are applied to a device.

The most common boundary conditions are Ohmic and Schottky. A contact is Ohmic when charge carriers immediately recombine when reaching the contact interface, leading to non-rectifying characteristics. At an Ohmic contact charge neutrality and equilibrium are assumed to hold. This leads to the boundary conditions of eqs. (49), (50) and (51), where V_T is the thermal voltage (i.e. k_BT/q).

$$n = \sqrt{\frac{(N_D - N_A)^2}{4} + n_i} + \frac{N_D - N_A}{2} \tag{49}$$

$$p = \sqrt{\frac{(N_D - N_A)^2}{4} + n_i} - \frac{N_D - N_A}{2} \tag{50}$$

$$\psi = \frac{E_F}{q} + V_T \operatorname{asinh}\left(\frac{N_D - N_A}{2n_i}\right) \tag{51}$$

As a result, the Fermi potential E_F/q at the contact is within some V_T from the electrostatic potential ψ in the semiconductor [12].

A contact is of Schottky type when the difference between the metal workfunction Φ and the semiconductor electron affinity χ creates a potential barrier between the metal and the semiconductor, leading to rectifying characteristics (Schenk (2012); Sze (1981)). For an n-type contact (i.e. an electron barrier is formed), the boundary conditions reported in eqs. (52), (53) and (54) hold. Those relations can be readily generalized for p-type contacts.

$$n = N_C \exp\left(-\frac{\Phi - \chi}{kT}\right) \tag{52}$$

$$p = N_V \exp\left(-\frac{\Phi - \chi + E_G}{kT}\right) \tag{53}$$

$$\psi = \frac{E_F}{q} - \frac{\Phi - \chi}{q} + V_T \ln\left(\frac{N_C}{n_i}\right) \tag{54}$$

As a result, the Fermi potential E_F/q at the contact is a barrier height away ((Φ-χ)$/q$) – minus some V_T factor – from the electrostatic potential ψ in the semiconductor. Note that the Fermi potential is equal to the applied voltage for non-resistive contacts, for both Ohmic and Schottky cases.

Interfaces between metallic electrodes and OSCs play a crucial role in the performance of organic devices (Scott (2003)). Metal-organic interfaces are usually characterized by a significant vacuum level offset – the origins of which are not yet fully understood – on which the Fermi level in the OSC and the injection barrier mostly depend on. The charge injection process is usually described as a thermally assisted tunneling from delocalized states of the metal into localized of the OSC, which is generally characterized in terms of Space Charge Limited Conduction (SCLC) (Lampert and Mark (1970)). There is no completely satisfactory analytic theory for the field and temperature dependence of the injection current, which, for well characterized interfaces, exhibits behavior relating to both thermionic emission and field-induced tunneling. This effects are usually taken into account by applying thermionic boundary conditions (Horio and Yanai (1990)), which considers the energy jump a carrier must be subject of when crossing a metal-organic interface.

---

[12] For non-doped semiconductors, E_F/q and ψ coincide.

2.3 Discretization

The PDEs describing semiconductors behavior are non-linear and tightly coupled, as shown in the previous section. TCAD tools handle the problem of their solution from a numerical point of view. This approach is enabled by a discretization process well-known as box integration method (Bank et al. (1983); Selberherr (2012)) – also called Finite Volume Method (FVM), which transforms PDEs into difference equations.

In order to perform box integration, the physical space onto which the simulation is carried on must be discretized. The resultant set of points is known in the device simulation jargon as "mesh". A popular algorithm employed to this extent is based on the Delaunay triangulation method (Delaunay (1934)).

A Delaunay mesh is a general triangular mesh in which any circle circumscribing each triangle does not contain any other point in the mesh (fig. 6a). One important feature of a Delaunay mesh is that it corresponds to the dual graph of a Voronoï diagram (Aurenhammer (1991)).

Specified a set of points – called seeds – into a given plane, a Voronoï diagram is a partitioning technique that associate each seed with a plane region. Each region is formed by all the points closer to its seed than to any other seed in the plane. A Delaunay mesh has the properties that each mesh point is a seed and that the center of each circumscribing circle belongs to a Voronoï diagram, as shown in figs. 6b and 6c. This considerations can be readily extended in a tridimensional space, in which a triangle is translated into a tetrahedron and a circle into a sphere.

Given a device structure with an associated Delaunay mesh, the complementary Voronoï diagram is employed as space tessellation in order to perform box integration.

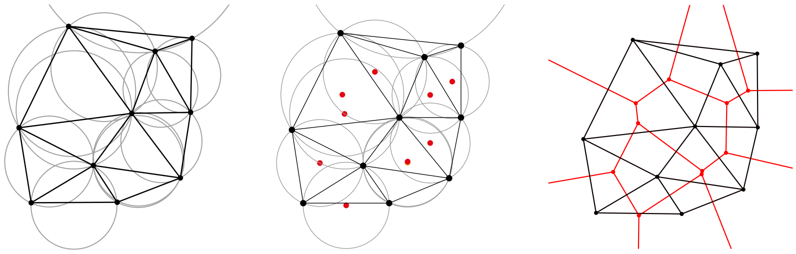

(a) **(b)** **(c)**

Figure 6: *Delaunay mesh: a) circumscribing circles, b) seeds, c) complementary Voronoï grid (red).*

The box integration method consists, for each point in the mesh, in the application of flux conservation to the related Voronoï region. More in detail, a PDE in semiconductor simulation can be generalized as in eq. (55).

$$\nabla \cdot \vec{A} + B = 0 \tag{55}$$

This relation can be transformed in non-local form using the divergence theorem on the volume V_i of the Voronoï box related to the i-th mesh point. The result gets discretized to a first order approximation as in eq. (56), where k_{ij} is a coefficient related to box geometry and the sum is carried among each confining mesh point.

$$\sum_{i \neq j} k_{ij} a_{ij} + V_i b_i = 0 \tag{56}$$

The value of a_{ij} and b_i for Poisson and continuity equations [13] are reported in tab. 1. Here, $\Delta_{ij} = (\psi_i - \psi_j)/V_T$ is the electrostatic potential difference between mesh points normalized to the thermal voltage V_T and $B(x) = x/(\exp(x) - 1)$ is the Bernoulli function (Synopsys (2015); Triebl (2012)).

Table 1: *Box integration coefficient for Poisson and continuity equations.*

Eq.	a_{ij}	b_i
Poisson	$\varepsilon \Delta_{ij} V_T$	$-\rho_i$
Electron Cont.	$q\mu_n V_T [n_i B(\Delta_{ij}) - n_j B(-\Delta_{ij})]$	$R_i - Gi + \frac{d}{dt} n_i$
Hole Cont.	$q\mu_p V_T [p_j B(-\Delta_{ij}) - p_i B(\Delta_{ij})]$	$R_i - Gi + \frac{d}{dt} p_i$

2.4 Solving Methods

Once difference equations are established on a discretized simulation space, the actual solution is usually achieved by algorithms based on the Newton's method (Bank et al. (1983)).

This method solves a non-linear system of difference equations $g(x) = 0$ by iteratively linearizing it around a guess solution x_i. Considering that $g(x_{i+1}) = 0$, this can be expressed as in eq. (57). The parameter λ is chosen close to 1 but such that $\|g(x_{i+1})\| < \|g(x_i)\|$, in order to aid numerical stability. Convergence criteria are usually based on the right-hand side norm (strong convergence)

---

[13] These are evaluated for a Drift-Diffusion transport model.

and/or relative error (weak convergence) becoming less than a certain limit, as indicated in eqs. (58) and (59).

$$g(x_i) + \frac{x_{i+1} - x_i}{\lambda} g'(x_i) = 0 \tag{57}$$

$$\|g(x_{i+1})\| < \varepsilon_{RHS} \tag{58}$$

$$\left\| \lambda \frac{x_{i+1} - x_i}{x_i} \right\| < \varepsilon_R \tag{59}$$

Newton's method iterations can be fully-coupled (fig. 7a) and de-coupled (fig. 7b) [14]. For fully-coupled iterations, equations are evaluated all together until convergence is reached. For de-coupled iterations, one equation at a time is considered. In the latter case the solution is exploited with respect to the primary unknown which gets updated at each step. Once convergence is reached for one equation, the process is applied to the following one.

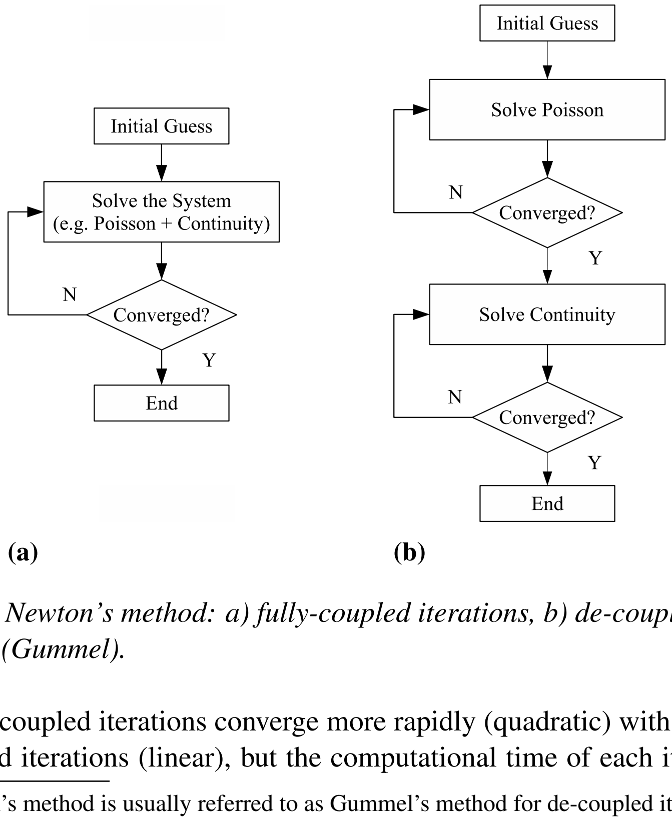

(a) **(b)**

Figure 7: *Newton's method: a) fully-coupled iterations, b) de-coupled iterations (Gummel).*

Fully-coupled iterations converge more rapidly (quadratic) with respect to de-coupled iterations (linear), but the computational time of each iteration in

---

[14] Newton's method is usually referred to as Gummel's method for de-coupled iterations

the latter case is smaller. Another important difference is that de-coupled iterations better tolerates a poor initial guess with respect to the fully-coupled case. As a general rule-of-thumb, de-coupled iterations perform better in the low-field regime.

For the solutions of eq. (57) several engines are available that performs better for various dimensionalities. For a mono-dimensional space usually direct methods based on systematic triangularization of the matrices performs well, for higher dimension it is usually better to employ parallel solvers (Cleveland Ashcraft et al. (1987); Dagum and Menon (1998); Schenk (2000)).

2.5 Application to Organic Semiconductors

Academic debate points out models derived from band-theory are sufficiently good to describe a broad range of organic devices characteristics, in addition to the historical description based on hopping/percolation theory. In this regard, the DD model is a well suited and supported alternative to the computational-demanding atomistic/Monte Carlo (MC) approach. The practical implication of the matter is that accurate simulations can be performed in reasonable time, exploring bigger simulation domains [15].

In this section, a brief survey on the use of the DD and TCAD tools for organic devices simulation is given. Far from being exhaustive, the list of works reported here shows the validity of this approach. The first applications of a DD model to organic device analysis and optimization have been exploited in OLEDs and Organic Photovoltaic (OPV). This methodology has been readily extended to OFET, as they represent the ideal testbed for OSCs transport properties.

Several reports in this field have been pointed out that commercial TCAD tools can be modified to account for models peculiar to OSCs and readily applied in order to solve the DD problem. The TCAD approach has been recently extended to Organic Photodiodes (OPDs) and novel devices concept, to which this thesis contributes. In most cases, this led to insights into organic devices physical behavior. The success of this process shows how such tools are promising in bridging the gap between device modeling and technology, playing a central role in the development of organic circuits and systems in the future.

---

[15] Simulations can be scaled at device or system level.

2.5.1 *Organic Light Emitting Diodes*

Davids et al. (1997) used the DD model to describe the transport properties of a single-layer OLED. In particular, they were able to explain the transition from a Schottky-limited conduction to SCLC based on the model. The authors validated their assumption comparing numerical data to the experimental response of a MEH-PPV OLED.

Using a similar approach, Ruhstaller et al. (2003) analyzed the behavior of a multilayer blue-emitting OLED. Notably, the authors were able to model also the optical response in addition to the electrical one. In adapting the DD model to this device, they considered field-dependent PF mobility and Langevin recombination. Simulations laid out the charge density profile throughout the OLED in various bias situations, allowing to explain the short-lived luminescence overshoot observed at turn-on. Based on these considerations, the author were able to determine the emission zone in the device depending on layer thickness and energy barrier, consequently using this insights to engineer the luminous output of a red-emitting OLED.

2.5.2 *Organic Photovoltaics*

For what concern OPV, DD simulations have been successfully exploited despite the class of materials used in these devices consist in a blend of two different OSCs to form a medium with intertwined morphology – the so called Bulk Heterojunction (BHJ).

In this regard, Koster et al. (2005) described the behavior of solar cells based on the P3HT:PC$_{61}$BM BHJ. Their simulations consist in iteratively solving Poisson, Continuity and DD equations using Gummel iterations. Boundary conditions have assumed to be Ohmic and recombination has been described using the Langevin model, while the photogeneration has been explained using the Onsager-Braun theory (Braun (1984); Onsager (1938)). The authors take out rule of-thumb for BHJ-based OPV optimization after the fitting of experimental data, suggesting to increase material mobility and more carefully position the electrodes workfunction to obtain an higher conversion efficiency.

The approach employed in this work is based on the assumption of a Virtual Semiconductor (VS), which is an equivalent semiconductor with intermediate properties with respect to the BHJ single phases. This is considered in order to yield reasonable simulation times, since there is no need for the mesh being too dense at interfaces in order to correctly describe the BHJ morphology. The VS approach still takes separately into account the characteristics of the two phases as, for instance, the HOMO of the donor and the LUMO of the acceptor are taken as E_V and E_C respectively [16], leading to reasonable results.

The VS approach has been extensively used since then, as Monestier et al. (2007) followed a similar train-of-thought in exploiting the DD model to study the short-circuit current of BHJ solar cells. Interestingly, they integrated in the electrical model plane-wave propagation in order to calculate the optical generation. The authors studied the dependency of the short-circuit current on the BHJ thickness, concluding the layer should balance photon absorption and recombination in order to maximize the former. This considerations can readily be applied to device fabrication.

Blakesley and Greenham (2009) employed DD simulations to show band bending effects at metal-organic interfaces limit the open-circuit voltage in OPV. Considering a Gaussian DOS across the interface, they show that band offset is increased upon disorder due to charge transfer in the tail states of the DOS itself. Based on numerical simulations, they propose that contact engineering in solar cells is a key factor in increasing efficiency.

2.5.3 Organic Field-Effect Transistors

Scheinert and Paasch (2004) have laid out a design process that starts with TCAD simulations of current and impedance, the latter performed on the OFET Metal-Insulator-Semiconductor (MIS) structure. They employed a DD model comprising a Gaussian DOS to improve accuracy and realistically describe device characteristics. The authors have used simulations results to lay down analytical estimations depending on device geometrical parameters. Those are employed as design rules during devices fabrication in order to show how the former steps can be used for device optimization. This process have been further extended considering several OSCs.

Bolognesi et al. (2004) employed TCAD simulations to study the effect of OSC morphology in Pentacene-based OFET. The polycrystalline nature of the OSC is initially taken into account by placing a single trap level at grain boundaries, to successively define with results obtained using an homogeneous OSC characterized by a PF mobility. Given the substantial accord between the two with experimental data, the authors conclude that a PF mobility is originated combining intra-grain and inter-grain transport.

---

[16] Only those two molecular levels are considered significant in the charge-transfer process after exciton separation.

TCAD simulations have been used by Gupta et al. (2009) to explain the difference in performance between bottom-contacts and top-contacts OFET. The lower mobility detected in bottom-contacts OFET is attributed to the poor morphology formed by the OSC in proximity of the electrodes. Varying the device structure to leave unfilled region and/or low mobility regions around the electrodes to simulate this effect, the authors were able to gain insights into conduction mechanisms at the contact, extracting guidelines to improve the experimental procedures.

MC simulations are still useful to calculate microscopic physical properties when applied to a small portion of a the organic material. They can be applied to calculate mobility dependencies upon electric field and temperature using hopping equations, to consequently insert the results into a DD model.

Following this approach, the current-voltage characteristics of OFET and Schottky diodes realized with different OSCs have been successfully described using TCAD simulations (Bolognesi et al. (2003)). The DD model considered in addition two exponential deep and shallow trap distributions in the bandgap of the semiconductor (adapting them from amorphous Silicon), constant DOS for electrons and holes (namely the density of molecules) and effective doping to simulate n- or p-type OSCs. Results were in good agreement with experimental data among a range of OSCs, showing the robustness of a mixed MC-DD approach.

2.5.4 Organic Photodiodes

More recently, Popescu et al. (2013) have extended the VS approach in exploiting TCADs for OPD analysis. They have been focusing especially on the optimization of the dynamic response when different Hole Injection Layer (HIL) are present. Trap distributions are considered in the bandgap of the VS to accurately reproduce the transient behavior. In particular, both Gaussian and Exponential distributions are considered in the bulk of the active material, while fixed charge and an Exponential distribution are employed at the BHJ/HIL interface.

Simulations consist in solving Poisson, Continuity and DD equations in both the steady-state and dynamic conditions. Based on these, the authors attribute the poor cut-off frequency observed under low light intensity conditions to the presence of interface traps, considering that the majority of carriers are photogenerated in the vicinity of the HIL/BHJ interface. The differences in performance when different HILs are considered is instead attributed to band misalignment.

2.6 Materials Modeling

DD simulations performed using TCAD tools are extensively used in this work and applied to OSCs. This section includes models and parameters employed for materials considered in the following chapters and is referred to throughout the thesis for sake of simplicity. It will be recalled in the text where those models have been refined or modified from what reported here.

2.6.1 Electrodes

In most cases, the effect of electrodes on a device can be modeled considering properly chosen boundary conditions. In organic electronics, electrodes actively play a central role in device operation (Shen et al. (2004); Tengstedt et al. (2006)) and situations arise where it is convenient to explicitly take into account their physical presence.

In order to do that, metals and ITO can be modeled as degenerate semiconductors having E_G=0 [17]. In this case, the electron affinity χ is simply equal to the work function Φ. The DOS and mobilities may be considered to be constant and symmetrical for both charge carriers, i.e. μ_n=μ_p=μ and N_C=N_V=N_{DOS}. Recombination and optical generation are not important and their contribution can be set to zero.

For metals, the number of free charge carriers can be computed as in eq. (60), where d is the density, w is the atomic weight, N_{AV} is the Avogadro number and N_{shell} is the number of electrons in the outer electronic shell.

$$n = p = \frac{d}{w} N_{AV} N_{shell} \tag{60}$$

Free charge carriers concentration can be accounted for by properly setting N_{DOS}. From Boltzmann statistics and in the case of degenerate semiconductors with E_G=0 this is simply given by n = N_{DOS}. Lastly, the mobility can be tuned as in eq. (61) in order to obtain the appropriate conductivity σ.

$$\mu = \frac{\sigma}{2qn} \tag{61}$$

---

[17] The ITO is a degenerately n-doped semiconductor with $\chi \approx 4.75$ eV (Sugiyama et al. (2000)). The E_G=0 assumption still holds for this material since typical HOMO/LUMO levels of photoactive OSCs are in the $5-3$ eV range, i.e. the energy range of ITO conduction band.

The modeling of ITO follows an analogous procedure, with typical quantities taken from Kim et al. (1999). The values of electrode model parameters are summarized in tab. 2. Data for the complex refractive index n_c has been taken from the Sentaurus©database and from Synowicki (1998) in the case of ITO.

Table 2: *Electrode model parameter values.*

	d	w	N_{shell}	N_{DOS}	χ	ρ	μ
	$[g/cm^3]$	$[g/mol]$	$[1]$	$[cm^{-3}]$	$[eV]$	$[\Omega cm]$	$[cm^2V^{-1}s^{-1}]$
Au	19.30	196.97	1	$5.9 \cdot 10^{22}$	5.0	$2.0 \cdot 10^{-6}$	26.0
Al	2.70	26.98	3	$18.1 \cdot 10^{22}$	4.1	$2.5 \cdot 10^{-6}$	7.1
Ca	1.55	40.08	2	$4.7 \cdot 10^{22}$	2.9	$3.3 \cdot 10^{-6}$	15.6
ITO	-	-	-	$5.0 \cdot 10^{20}$	4.75	$4.0 \cdot 10^{-4}$	20.3

2.6.2 PEDOT:PSS

The PEDOT:PSS is a conductive polymer which is generally used to favor injection of holes from an anode into an OSC, i.e. it is used as HIL. This material can be modeled as an intrinsic semiconductor with $E_G = 1.8\ eV$, which is in the limit of infinitely long chain with bandgap saturation (Zade and Bendikov (2006)). The workfunction Φ of PEDOT:PSS is reported in the range of $4.7-5.4\ eV$ (Brown et al. (1999); Crispin et al. (2006); Greczynski et al. (2001); Huang et al. (2005)). This can be considered coincident with the Fermi level E_F, resulting in an electron affinity χ of $3.8-4.5\ eV$. The DOS can be considered symmetric and chosen accordingly to eq. (62).

$$N_{DOS} = \frac{\sigma}{q\mu_p} \exp\left(\frac{E_G}{kT}\right) \tag{62}$$

The PEDOT:PSS conductivity σ has been reported between $0.05-50\ S\ cm^{-1}$ (Jönsson et al. (2003)), depending on solvent doping and post-processing treatment. Recombination in PEDOT:PSS can be described using SRH with E_T located at midgap. Optical generation in this material can be neglected.

The salient features of the model are summarized in tab. 3. For typical applications contained in this thesis, values of $\Phi = 4.8\ eV$ and $\sigma = 0.05\ S\ cm^{-1}$ (pristine) will be employed in simulations. Since the PEDOT:PSS is an hole transporter, the electron mobility has been taken three order of magnitude lower than the hole mobility, chosen as μ_p equal to 10^{-3} cm^2 V^{-1} s^{-1} (Petrosino and Rubino (2011)). The complex refractive index n_c has been extracted from Pettersson et al. (2002).

Table 3: *PEDOT:PSS model parameter values.*

	Φ $[eV]$	E_G $[eV]$	χ $[eV]$	σ $[Scm^{-1}]$	μ_p $[cm^2V^{-1}s^{-1}]$
PEDOT:PSS	4.8	1.8	3.9	0.05	10^{-3}

2.6.3 P3HT

The P3HT is a p-type semiconducting polymer belonging to the tiophenes family. It has been widely studied due to its properties as solubility, good hole mobility and optical absorption. The salient features of the P3HT model are summarized in tab. 4. The absorption coefficient α_{abs} has been extracted by Hoppe and Sariciftci (2004). The relative dielectric constant is reported to be 3 (Juška et al. (2003)).

Table 4: *P3HT model parameter values.*

	χ $[eV]$	E_G $[eV]$	N_{DOS} $[cm^{-3}]$	ε_r $[1]$
P3HT	2.7	1.9	$5 \cdot 10^{20}$	3

2.6.4 PC$_{61}$BM

The PC$_{61}$BM is a n-type semiconducting molecule and it is a derivative of C$_{60}$. It is a more practical choice as n-type semiconductor if compared to C$_{60}$ because of its enhanced solubility. This allows for solution processable donor/acceptor mixes, and PC$_{61}$BM has mostly been studied blended with P3HT to enhance the absorption of OPV devices. However, considering the costs of fabrications, it is not certain that this derivative can be synthesized on a large scale for commercial applications.

The salient features of the $PC_{61}BM$ model are summarized in tab. 5. The relative dielectric constant is reported to be 3.9 (Blom et al. (2007)). The absorption coefficient α_{abs} has been extrapolated by Hoppe and Sariciftci (2004).

Table 5: *$PC_{61}BM$ model parameter values.*

	χ $[eV]$	E_G $[eV]$	N_{DOS} $[cm^{-3}]$	ε_r $[1]$
$PC_{61}BM$	3.7	2.1	$5 \cdot 10^{20}$	3.9

2.6.5 P3HT:$PC_{61}BM$

The P3HT:$PC_{61}BM$ blend is one of the most widely characterized photoactive Bulk Heterojunction and it is extensively used as benchmark material. For DD simulations contained in this thesis, this BHJ is modeled using the VS approach (see section 2.5.2).

The electron affinity χ and the energy gap E_G of the VS are taken to be 3.7 eV and 0.9 eV respectively, which correspond to conduction and valence band edges of 3.7 eV and 4.6 eV. These values have been chosen considering that only the HOMO of the donor (Tsoi et al. (2011)) and LUMO of the acceptor (Larson et al. (2013)) are relevant to charge transfer and exciton dissociation processes. The relative dielectric constant ε_r and the absorption coefficient α_{abs} of the VS have been taken to be the average of those in the single phases, considering a commonly used weight ratio of 1:1 (Chen et al. (2010)).

The key parameters in the model are highlighted in tab. 6. The refractive index n_r has been taken from Dennler et al. (2007).

Table 6: *P3HT:$PC_{61}BM$ model parameter values.*

	χ $[eV]$	E_G $[eV]$	N_{DOS} $[cm^{-3}]$	ε_r $[1]$
P3HT:$PC_{61}BM$	3.7	0.9	$5 \cdot 10^{20}$	3.45

2.6.6 Al_2O_3

The Al_2O_3 is the native oxide growing on Aluminum and it is often used in organic devices as gate insulator due to the high dielectric constant and the possibility to achieve very thin layers.

This material is simply modeled as an ideal insulator having E_G equal to 9.9 eV (Jimenez-Gonzalez and Schmeisser (1991)) and relative dielectric constant ε_r equal to 7 (Voigt and Sokolowski (2004)).

The key parameters in the model are summarized in tab. 7. The complex refractive index n_c has been extrapolated from French et al. (1998).

Table 7: *Al_2O_3 model parameter values.*

	E_G	ε_r
	$[eV]$	[1]
Al_2O_3	9.9	7

2.7 Conclusion

In this chapter, the application of Technology Computer Aided Design (TCAD) tools to the simulation of organic electronic devices has been discussed. These tools integrates various physical models – both electrical and optical – as a set of Partial Differential Equation that gets evaluated on a spatial discretization of the device structure and solved through iterative techniques based on the Newton's method. The models contained in TCAD tools belong to the band-structure description of semiconductor materials. These models are still relevant for the analysis of Organic Semiconductors in a Multiple Trapping and Release framework and – with the opportune modifications – have been demonstrated to yield accurate results and physical insights in reasonable simulation times.

In the first part of this chapter, TCAD models for the description of electrostatic potential, carrier transport and recombination, electronic traps, optical generation and boundary conditions have been highlighted. Models peculiar to the behavior of Organic Semiconductors have been debated where appropriate. Then, an brief introduction on the discretization and solving strategies relevant to the TCAD architecture have been discussed. While the application of TCADs to the broad spectrum of organic electronics is fairly new, relevant examples of tools exploitation for design and analysis of conventional devices are present in the literature. Those have been discussed as well. In the last part, the models employed inside this thesis for organic and inorganic materials have been rolled out as a basis for the discussion of following chapters.

Chapter 3
The Organic Field-Effect Transistor

3.1 Introduction

Over the last decade, Organic Photodiodes (OPDs) and Organic Phototransistors (OPTs) have emerged as promising technologies to be exploited in light sensing systems (Baeg et al. (2013)). Several exciting applications have been successfully demonstrated taking advantage of the conformal features (Ng et al. (2008)) and biocompatibility (Scarpa et al. (2010)) of photosensitive Organic Semiconductors (OSCs), as the realization of near infrared detectors (Rauch et al. (2009)) and prosthetic apparel to restore sensitivity in the retina of blind rats (Ghezzi et al. (2013)). Nevertheless, the realization of reliable systems to be employed in commercial applications is subordinate to a full device optimization. In this regard, the Organic Field-Effect Transistor (OFET) can be used as a testbed device to analyze the properties of a given OSC.

In this chapter, the characteristics of P3HT:$PC_{61}BM$-based OFETs are analyzed in order to study the electrical properties of this archetypal photoactive OSC. A comparison is performed between a device realized using neat P3HT and one comprising the complete Bulk Heterojunction (BHJ), in order to spot relevant differences due to the addition of $PC_{61}BM$. Both Direct Coupling (DC) and Alternate Coupling (AC) characteristics of the OFETs are taken into account. The measured current-voltage relationships are compared to an existing DC empirical model to estimate important figures-of-merit as field-effect mobility, threshold voltage and subthreshold swing. Further deductions are made analyzing the admittance of the devices in function of the frequency, which carries information about charge relaxation processes inside the OSC. The analysis is performed comparing the experimental data with an empirical model based on a RC equivalent circuit, in order to extract the relevant relaxation time constants.

In both the DC and AC cases, the measured curves are also compared with

Technology Computer Aided Design (TCAD) simulations of current and admittance in a way to lay a physical background to the fitting models, refine the estimations of relevant quantities and the interpretation of devices behavior. This analysis allows to clarify – on various levels of abstraction – the electrical characteristics of those important OSCs and can be applied to device optimization, as similar OFETs can be directly exploited as OPT.

3.2 State of the Art

This section gives a brief survey on the state-of-the-art of OFET modeling and characterization in the steady-state and under dynamic conditions. The aspects most relevant to the present discussion are highlighted. OFETs are planar transistors that rely on the presence of an electric field to modulate the current flowing into a thin-film of an OSC. This electric field is controlled by a gate electrode, which is separated from the OSC by an insulating layer called gate dielectric. In other words, the gate electrode, dielectric and OSC form a Metal-Insulator-Semiconductor (MIS) capacitor, which – conveniently biased with a gate voltage V_G – is responsible for the accumulation of free charge at the semiconductor/insulator interface, with the consequent modulation of the OSC conductivity. Therefore, with two metal contacts attached to the OSC – the source and the drain – the electric current flowing through the transistor can be efficiently controlled (Klauk (2010)).

Depending on the relative position of the gate electrode and dielectric with respect to the source and drain contacts, several configurations are possible (fig. 8). Those can be divided in:

- Bottom-Gate Top-Contacts (BGTC), in which the gate electrode is below the gate dielectric and source/drain contacts are on top of the OSC (fig. 8a);
- Bottom-Gate Bottom-Contacts (BGBC), in which the gate electrode is below the gate dielectric and source/drain contacts are below the OSC (fig. 8b);
- Top-Gate Bottom-Contacts (TGBC), in which the gate electrode is on top of the gate dielectric and source/drain contacts are below the OSC (fig. 8c);
- Top-Gate Top-Contacts (TGTC), in which the gate electrode is on top of the gate dielectric and source/drain contacts are on top of the OSC (fig. 8d).

Each configuration offer slight advantages or disadvantages under an oper-

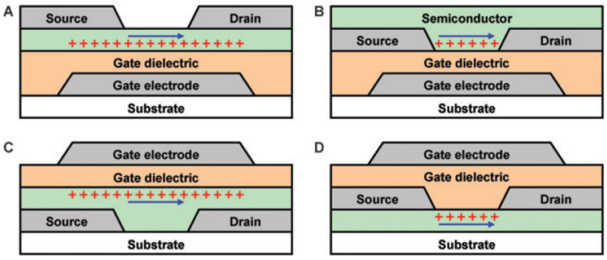

Figure 8: *OFET configurations: a) BGTC, b) BGBC, c) TGBC, d) TGTC (Klauk (2010)).*

ational and technological point of view. However, in any case the geometrical characteristics of the source and drain contacts greatly influence the performance of the OFET. In this regard, the two key factors are the channel length L_{CH}, which is the distance between source and drain contacts, and the channel width W_{CH}, which is the extension of those contacts perpendicularly to the current flow.

As said, the OFET is often used to asses the electrical properties of new materials. The Charge Control Model (CCM) [18] (Shur (1990)) is widely accepted and used in the organic electronics community to estimate the field-effect mobility μ_{FE} associated to the OSC. In the CCM, the drain current I_D is expressed as reported in eq. (63), where a linear region (top expression) and a saturation region (bottom expression) are distinguished.

$$I_D = \begin{cases} \frac{\mu_{FE} C_{ins} W_{CH}}{L_{CH}} \left[(V_{GS} - V_{TH}) V_{DS} - \frac{V_{DS}}{2}^2 \right] & |V_{DS}| < |V_{GS} - V_{TH}| \text{ (lin.)} \\ \frac{\mu_{FE} C_{ins} W_{CH}}{2 L_{CH}} (V_{GS} - V_{TH})^2 & |V_{DS}| > |V_{GS} - V_{TH}| \text{ (sat.)} \end{cases} \tag{63}$$

Here, C_{ins} is the gate dielectric capacitance, V_{TH} is the threshold voltage, V_{GS} is the gate-source voltage and V_{DS} is the drain-source voltage. The gate dielectric capacitance C_{ins} is expressed per unit area, simply being the ratio between the insulator dielectric constant ε_{ins} and thickness t_{ins}.

An OFET can be considered in the on-state when $|V_{GS}| > |V_{TH}|$. However, a non-negligible drain current usually flows even when the V_{GS} is below the threshold. This is known as subthreshold region. In this region, the drain current is determined by diffusion rather than drift and assumes an exponential trend (Gosney (1972)). The voltage at which the drain current increase significantly over the off-state value is usually indicated as the onset voltage V_{ON}

---

[18] This has been initially developed for the Silicon MOSFET.

(Meijer et al. (2002)). The field-effect mobility μ_{FE} can be estimated by both linear and saturation regions, as reported in eqs. (64) and (65) respectively.

$$\mu_{FE} = \frac{|\partial I_D/\partial V_G| L_{CH}}{C_{ins} V_{DS} W_{CH}} \tag{64}$$

$$\mu_{FE} = \frac{\left|\partial \sqrt{I_D}/\partial V_G\right|^2 2L_{CH}}{C_{ins} W_{CH}} \tag{65}$$

3.2.1 DC Characteristics

A more thorough estimation of the steady-state OFET figures-of-merit can be performed by applying DC compact models to the experimental curves. These models are developed in order to: i) include realistic device behavior, taking into account non-idealities related to higher order effects; ii) be applicable in circuit simulators, i.e. having a well-behaved mathematical formulation to avoid convergence issues (Kim et al. (2014)). Three main approaches can be considered in this regard. These are reported here for p-type OFETs, but can be generalized to n-type transistors as well. Those DC models lay their framework to a common ground, so it is useful to define some quantities beforehand. A gate overdrive voltage can be defined as in eq. (66) for the above threshold region (V_{GOV}^{abv}) and eq. (67) for the subthreshold region (V_{GOV}^{sub}). Similarly, a drain overdrive voltage can be defined as in eq. (68).

$$V_{GOV}^{abv} = V_{GS} - V_{TH} \tag{66}$$

$$V_{GOV}^{sub} = V_{GS} - V_{ON} \tag{67}$$

$$V_{DOV} = (V_{GS} - V_{TH}) - V_{DS} \tag{68}$$

The Marinov model (Deen et al. (2009); Marinov, Deen, Zschieschang and Klauk (2009)) starts from the CCM assumptions and considers a V_{GS}-dependent field-effect mobility μ_{FE}, which follows a power-law relationship as in eq. (69).

$$\mu_{FE}(x) = \mu_{FE0}\left[-\frac{V_{GOV}^{abv} - \psi(x)}{V_{AA}}\right]^{\zeta} \tag{69}$$

Here, ψ is the longitudinal electrostatic potential into the channel, whereas μ_{FE0}, ζ and V_{AA} are empirical parameters. The choice of a power-law mobility is related to the transport of charge in an exponential Density Of States (DOS). Extensive physical correlation is found in Marinov, Deen and Datars (2009), in which the analysis of various materials also shows realistic ranges of empirical parameters. Integration of the channel charge along the x direction yields the I_D expression of eq.(70).

$$I_D = \mu_{FE0} C_{ins} \frac{W_{CH}}{L_{CH}} \frac{[-V_{DOV}]^{\zeta+2} - [-V_{GOV}^{abv}]^{\zeta+2}}{(\zeta+2) V_{AA}^{\zeta}} \tag{70}$$

In addition, to account for realistic below-to-above threshold transition, an arbitrary gate overdrive function is introduced as in eq. (71), where V_{SS} defines the slope of the current in the subthreshold region.

$$f_a(V) = V_{SS} \ln \left\{ 1 + \exp \left[- \frac{V_{GOV}^{abv} - V}{V_{SS}} \right] \right\} \tag{71}$$

The final I_D expression is given in eq. (72), having also taken into account the channel length modulation factor λ_{CH}.

$$I_D = \mu_{FE0} C_{ins} \frac{W_{CH}}{L_{CH}} \frac{f_a(V_{DS})^{\zeta+2} - f_a(0)^{\zeta+2}}{(\zeta+2) V_{AA}^{\zeta}} (1 - \lambda_{CH} V_{DS}) \tag{72}$$

The Estrada model separately accounts for each operating region in the device, merging the expressions into one with the aid of suitable transition functions (Estrada et al. (2005); Kim et al. (2013)). Also in this case, the field-effect mobility μ_{FE} is V_{GS}-dependent with a power law relationship. The μ_{FE} expression is reported in eq. (73) and has been related to hopping transport in an exponential DOS (Castro-Carranza et al. (2012); Estrada et al. (2010, 2008)).

$$\mu_{FE} = \mu_{FE0} \left[- \frac{V_{GOV}^{abv}}{V_{AA}} \right]^{\zeta} \tag{73}$$

The starting point for I_D computation above the threshold is the linear region of the CCM model. This is given in eq. (74), where the V_{DS} quadratic term has been neglected and a contact resistance R_C has been considered.

$$I_{DS}^{abv} = -\mu_{FE} C_{ins} \frac{W_{CH}}{L_{CH}} [V_{GOV}^{abv} (V_{DS} - I_{DS}^{abv} R_C)] \tag{74}$$

By substituting eqs. (73) into (74) and rearranging terms, the I_D expression above the threshold is obtained as in eq. (75). Here, to have better control over the shape of the output curves of the OFET, a fitting function f_b is introduced to tailor the V_{DS} shape. This is reported in eq. (76), where α_S and m are fitting parameters. Also, the channel modulation length factor λ_{CH} is considered.

$$I_{DS}^{abv} = \frac{\mu_{FE0} C_{ins} \frac{W_{CH}}{L_{CH}} \frac{(-V_{GOV}^{abv})^{\zeta+1}}{V_{AA}^{\zeta}}}{1 + \mu_{FE0} C_{ins} \frac{W_{CH}}{L_{CH}} R_C \frac{(-V_{GOV}^{abv})^{\zeta+1}}{V_{AA}^{\zeta}}} f_b V_{DS} (1 - \lambda_{CH} V_{DS}) \tag{75}$$

$$f_b = \left\{ 1 + \left[\frac{V_{DS}}{\alpha_S V_{GOV}^{abv}} \right]^m \right\}^{-\frac{1}{m}} \tag{76}$$

The I_D expression in the subthreshold region is given by the exponential relation of eq. (77), where I_{OFF} is the off-state current and SS is the subthreshold swing.

$$I_{DS}^{sub} = I_{OFF} \exp\left[-\frac{\ln(10)}{SS} V_{GOV}^{sub} \right] \tag{77}$$

The different working regions of the OFET are merged into one expression by using the transition functions of eq. (78), where B and V_B are fitting parameters. The total current is obtained as in eq. (79).

$$f_c^{(\pm)} = \frac{1}{2} \{ 1 \pm \tanh[B(V_{GS} - V_B)] \} \tag{78}$$

$$I_{DS} = I_{DS}^{above} f_c^{(-)} + I_{DS}^{sub} f_c^{(+)} + I_{OFF} \tag{79}$$

The Li model (Li et al. (2010)) considers the potential barrier between grains in a polycrystalline organic thin film. An analytical expression for the V_{GS}-dependent field-effect mobility is empirically derived considering hopping transport between OSC grains. This is reported in the exponential relationship of eq. (80), where the empirical parameters κ and s can be correlated to the DOS of the OSC.

$$\mu_{FE} = \mu_{FE0} \exp\left(\frac{s}{V_{GS} - \kappa} \right) \tag{80}$$

The I_D expression is derived by substituting eqs. (80) into the linear region CCM model relationship, replacing V_{TH} with V_{ON} and accounting for the fitting function f_b as reported in eq. (76). The final relationship is shown in eq. (81), where the channel length modulation factor λ_{CH} is added again.

$$I_{DS} = -\mu_{FE0} C_{ins} \frac{W_{CH}}{L_{CH}} \exp\left(\frac{s}{V_{GS} - \kappa}\right) \left[V_{GOV}^{sub} - (V_{GOV}^{sub} - V_{DS} f_b)^2\right] (1 - \lambda_{CH} V_{DS}) \tag{81}$$

The salient features of the three models reported above are summarized in tab. 8, highlighting empirical and fitting parameters. Given their abundant presence, the application of those models to the same set of experimental data provides enough adjustment precision to satisfactorily reproduce the measured curves. Note that μ_{FE0}, V_{TH} [19] and λ_{CH} are not listed in tab. 8 since they are considered in each model as empirical parameters.

Table 8: *Empirical and fitting parameters in the Marinov, Estrada and Li OFET DC compact models.*

Model	*Equation*	*Empirical Parameters*	*Fitting Parameters*
Marinov	(72)	ζ, V_{AA}	V_{SS}
Estrada	(79)	ζ, V_{AA}, R_C, I_{OFF}, V_{ON}, S	α_S, m, B, V_B
Li	(81)	s, κ	α_S, m

These considerations indicate the underlying physical assumptions gain more importance to check the reliability of a model, in contrast to the mathematical accuracy of the fitting, as the introduction of arbitrarily shaped functions is limiting the applicability of the reported equations to a semi-empirical context. Moreover, in all the reported models V_{TH} is constant and results as an additional empirical parameter, while to be accurate the effect of interface traps and fixed charge should be taken into account.

3.2.2 AC Characteristics

OFETs are not only characterized in terms of steady-state characteristics, since for any applicability minimum requirements on the speed of operation must be fulfilled. The figure-of-merit employed at this purpose is the cut-off frequency f_c, which is defined as the frequency in which the voltage gain becomes equal to 1. The cut-off frequency is determined by the transconductance gain g_m and gate capacitance, which is larger than the insulator capacitance C_{ins} due to overlap regions. An upper-bound estimation to the cut-off frequency can

---

[19] This is replaced by V_{ON} in the Li model.

therefore be given as in eq. (82) (Miyadera et al. (2007); Scheinert and Paasch (2004)).

$$f_c \leq \frac{\mu_{FE}}{2\pi L_{CH}^2} V_{GOV}^{abv} \tag{82}$$

The cut-off frequency of an OFET can be experimentally determined by manufacturing a ring oscillator, i.e. a circuit formed by an odd number of logic inverters connected in a feedback loop. The signal between the two extremes of the feedback loop is characterized by a delay originated from the OFETs capacitive elements. Evaluation of the delay normalized on the number of ring oscillator stages leads to the average inverter response time and – in turn – to f_c (Zschieschang et al. (2011)). Often, the manufacturing of a ring oscillator is not feasible, hence the dynamic features of an OFET should be estimated by other means. One possibility is to use spectroscopic techniques. Of particular importance is admittance spectroscopy, which consists in the evaluation of the small-signal steady-state parallel admittance of a given device varying the excitation frequency. The admittance Y_P is often expressed in terms of the capacitance C_P and loss L_P functions, as in eq. (83), where ω is the angular frequency.

$$Y_P = \omega L_P(\omega) + i\omega C_P(\omega) \tag{83}$$

The analytical expressions of loss and capacitance functions for a relaxation process with lifetime τ_0 are reported in eqs. (84) and (85) respectively, for both a single-level DOS and distributed DOS (Nicollian and Goetzberger (1967); Nicollian and Brews (1982); Stallinga (2009)).

$$L_P(\omega) = \begin{cases} qN_{DOS}\frac{1}{1+\omega^2\tau_0^2} & \text{single level} \\ qN_{DOS}\frac{\ln\left(1+\omega^2\tau_0^2\right)}{2\omega\tau_0} & \text{distribution} \end{cases} \tag{84}$$

$$C_P(\omega) = \begin{cases} qN_{DOS}\frac{\omega\tau_0}{1+\omega^2\tau_0^2} & \text{single level} \\ qN_{DOS}\frac{\operatorname{atan}(\omega\tau_0)}{\omega\tau_0} & \text{distribution} \end{cases} \tag{85}$$

According to eq. (84) and for a single-level DOS, the L_P function possesses a peak located at ω equal to $1/\tau_0$, with a peak magnitude that coincides with the C_P value at the same angular frequency. In addition, the C_P function is subject to an inflection point at ω equal to $1/\tau_0$ [20]. When the L_P dispersion can be attributed to the response of free charge in the channel, the peak frequency can

---

[20] The situation is slightly different for a distributed DOS, as the L_P peak occurs at ω equal to $1.98/\tau_0$.

be taken as an estimation of f_c. In addition, this f_c estimation can be related to free charge carriers diffusivity – hole or electron depending on device type and bias – for an OSC thickness t_{OSC}, as reported in eq. (86) (Stallinga et al. (2008)).

$$D_{n,p} = \frac{t_{OSC}^2}{\tau_0} = t_{OSC}^2 2\pi f_c \tag{86}$$

3.3 Bulk Heterojunction-Based Transistors

In spite of the impressive experimental improvements achieved for OFET, there is still a lack of theoretical understanding on their behavior. This is attributable to the fact that is difficult to individuate a circumscribed experimental framework, as especially true for devices realized with BHJ semiconductors. The huge variety of materials, the high sensitivity of OSCs microstructure on process conditions, and the instabilities caused by the gradual formation of degradation-related species hinders the development of general models. As a result, first principles governing charge transport in OSCs are difficult to readily be extended for a current-voltage description of the devices. In this section, the characteristics of P3HT and P3HT:PC$_{61}$BM-based OFETs are analyzed through models and TCAD numerical simulations in order to study the electrical properties of this archetypal photoactive OSC. Both ad DC and AC analysis are conducted, in terms of current-voltage relationships and admittance spectroscopy.

The OFETs were realized in a BGTC configuration, with an interdigitated channel geometry having W_{CH} of 18 mm and L_{CH} of 50 μm, i.e. a form factor W_{CH}/L_{CH} equal to 360. The devices were fabricated on thermally oxidized p-type Silicon substrates having nominal Silicon Oxide thickness t_{ins} of 300 nm (Ossila), which served as both gate electrode and insulator. The substrates were cleaned with standard procedures comprising ultrasonic baths in Isopropanol and Acetone and UV-Ozone sterilization.

The semiconductors were deposited from solution on the cleaned substrates by spin-coating deposition, occurring at 2000 rpm for 60 s, with an acceleration ramp of 5 s. Solutions were prepared in oDCB with concentrations of 1:100 (1:1:100) %wt for P3HT (P3HT:PC$_{61}$BM), stirred for 2 hours on an hot plate at 333.15 K and filtered before utilization. Morphology analysis of the resulting films were performed with a stylus profilometer (KLA-Tencor P-6). The resultant semiconductor thicknesses t_{OSC} were of 30 ± 3 nm for P3HT and 69 ± 6 nm for P3HT:PC$_{61}$BM, with average roughness and waviness of approximately 2.7 ± 0.5 *nm* and 0.6 ± 0.2 *nm* as measured on a scan domain with a 400 μm side. The OFETs were completed by the Gold source and drain contacts deposition by thermal evaporation through a shadow mask. The process was performed from a base pressure of $4 \cdot 10^{-7}$ *mbar* at an evaporation rate of 0.15 $nm\ s^{-1}$, resulting in a thickness of 46 *nm*.

The samples were held in vacuum until the electrical characterization was performed. The current-voltage curves of the devices were measured with a semiconductor parameter analyzer (Agilent 4155B). The admittance of the MIS diode formed between the gate and the short-circuited drain/source contacts was evaluated with an *LCR* meter (Agilent 4980A) for gate biases between -40 *V* and 40 *V*, considering a sinusoidal excitation of 100 *mV*. The admittance were expressed per unit area, as normalized on the total source/drain contacts surface of approximately 0.025 cm^2. All measurements were performed at room temperature, in ambient air and under dark conditions.

3.3.1 Current-Voltage Analysis

The transfer curves of the P3HT and P3HT:PC$_{61}$BM OFETs are shown in fig. 9 for V_{DS} equal to -10 *V* (symbols). Only the drain current is reported since the gate leakage are considered negligible, i.e. not larger than 10 *nA* in any case. The transfer curves are compared to a simplified version of the Estrada model (see section 3.2.1), which is also shown in fig. 9 (line).

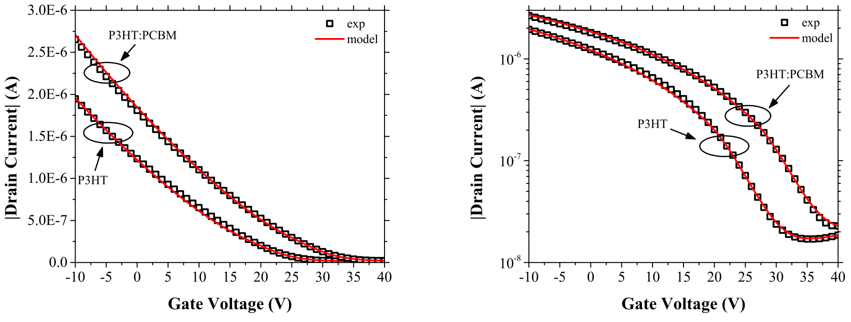

(a) **(b)**

Figure 9: *Experimental and modeled OFETs transfer curves: a) linear scale, b) logarithmic scale.*

In the simplified model, the expression of the current in the above threshold region is simply the linear portion of the CCM with a V_{GS}-dependent field-effect mobility. The latter is reported in eq. (73). In other words – following the Estrada model derivation – the V_{DS} quadratic term is not neglected. Moreover, R_C, λ_{CH} and $1/\alpha_S$ are considered equal to zero and m is considered equal to one in eq. (75). On the other hand, the expressions for subthreshold and total currents are identical to those reported in eqs. (77) and (79). The parameters used in the generation of the fitting model curves are reported in tab. 9, which can be used to have an idea of the fabricated OFET performance in terms of figures-of-merit.

Table 9: *The parameters employed in the fitting model of the OFET currents.*

	μ_{FE0} $[cm^{-2}V^{-1}s^{-1}]$	V_{AA} $[V]$	ζ $[1]$	V_{TH} $[V]$	V_{ON} $[V]$	I_{OFF} $[A]$	SS $[Vdec^{-1}]$
P3HT	$2.1 \cdot 10^{-4}$	1	0.5	27.0	31.2	$1.7 \cdot 10^{-8}$	9.8
BHJ	$2.1 \cdot 10^{-4}$	1	0.5	34.5	38.2	$1.7 \cdot 10^{-8}$	10

As said before, given the high number of fitting and empirical parameters, even a simplified version of the Estrada model can describe very accurately the experimental transfer curves of the devices in both linear and logarithmic scales. In this regard, employing a V_{GS}-dependent mobility is a key factor to achieve an accurate fit the measured data. A field-effect mobility estimation based on the linear region of the CCM [eq. (64)] for V_{DS} equal to $-10\ V$ yields to μ_{FE} of $1.7 \cdot 10^{-3}\ cm^{-2}\ V^{-1}\ s^{-1}$ for P3HT and $1.8 \cdot 10^{-3}\ cm^{-2}\ V^{-1}\ s^{-1}$ for the BHJ. On contrast, the μ_{FE} values obtained with a V_{GS}-dependent model span one order of magnitude, from the low-field values of μ_{FE0} [21] to the maximum values obtained for V_{GS} equal to $-10\ V$, which are $1.28 \cdot 10^{-3}$ $cm^{-2}\ V^{-1}\ s^{-1}$ (P3HT) and $1.4 \cdot 10^{-3}\ cm^{-2}\ V^{-1}\ s^{-1}$ (P3HT:PC$_{61}$BM). These considerations show the effect of electric field enhancement as V_{GS} becomes more negative, allowing the model to follow the curvature of the current as the OFETs are brought more and more into accumulation. Considering a constant mobility, as estimated from the CCM, would only account for the maximum mobility values. In addition, it is worth noting how the μ_{FE} values are similar between P3HT and BHJ OFETs, suggesting the addition of PC$_{61}$BM does not lower the transport properties.

On the other hand, V_{TH} is found to be large and positive in both devices, shifting towards increasing positive voltages with consecutive gate polariza-

---

[21] The μ_{FE0} represents a low-field mobility since a normalization value of V_{AA} equal to 1 V is employed.

tion, denoting bias stress effects (data not shown). Since in the fabricated OFETs no interface treatments have been employed, it is likely this behavior is attributable to the poor quality of the insulator/semiconductor interface. The interface traps concentration N_{if} can be estimated by the subthreshold region of the transfer curves. The relationship relating N_{if} to the subthreshold swing SS is reported in eq. (87) (Sze (1981)).

$$SS = \ln(10)\frac{k_B T}{q}\left(1 + \frac{qN_{if}}{C_{ins}}\right) \tag{87}$$

Inverting this expression, N_{if} results to be $1.17 \cdot 10^{13}$ cm^{-2} V^{-1} and $1.19 \cdot 10^{13}$ cm^{-2} V^{-1} for P3HT and P3HT:PC$_{61}$BM respectively.

In order to investigate the physical framework behind the high V_{TH} values, the transfer and output curves of the OFETs are also compared with TCAD simulations. The experimental and simulated curves are shown in fig. 10.

The simulations are performed with the state-of-the-art commercial tool Sentaurus©(Synopsys (2015)). In this regard, the source/drain contacts and gate electrode effect is taken into account using Schottky boundary conditions (Gold and Silicon), while the SiO$_2$ insulating layer is explicitly considered. The models for those materials are taken from the Sentaurus©database. On the other hand, the models for P3HT and the BHJ are specifically introduced into the simulator as reported in section 2.6. In particular, the Virtual Semiconductor (VS) approach is employed for P3HT:PC$_{61}$BM modeling (see section 2.5.2). Both constant and Power Law (PL) [see section 2.2.2, eq. 28] mobility models are considered for μ_p. On contrast, μ_n has been evaluated as a constant and varied in a broad range (10^{-6} through 10^{-3} cm^{-2} V^{-1} s^{-1}) without observing appreciable changes in the simulation data. The PL model was implemented and added to the device simulator using the Sentaurus©Physical Model Interface (PMI) [22]. The insulator/semiconductor interface has been characterized by an exponential acceptor traps distribution (see section 2.2.4) and a negative fixed charge N_{fix}. The parameter values employed for mobility, traps and fixed charge are reported in tab. 10. Those values are the result of an iterative process aimed to obtain the best fit for what concern the transfer curves of the OFETs.

Once again, the use of a field-dependent mobility model has been revealed of foremost importance in order to achieve accordance to the experimental

---

[22] The PMI allows to extend existing Sentaurus©models in the semiconductor transport equations. The new models are provided as C++ functions which shall compute the main quantity and derivatives with respect to independent variables. Those functions are loaded at run time during simulations.

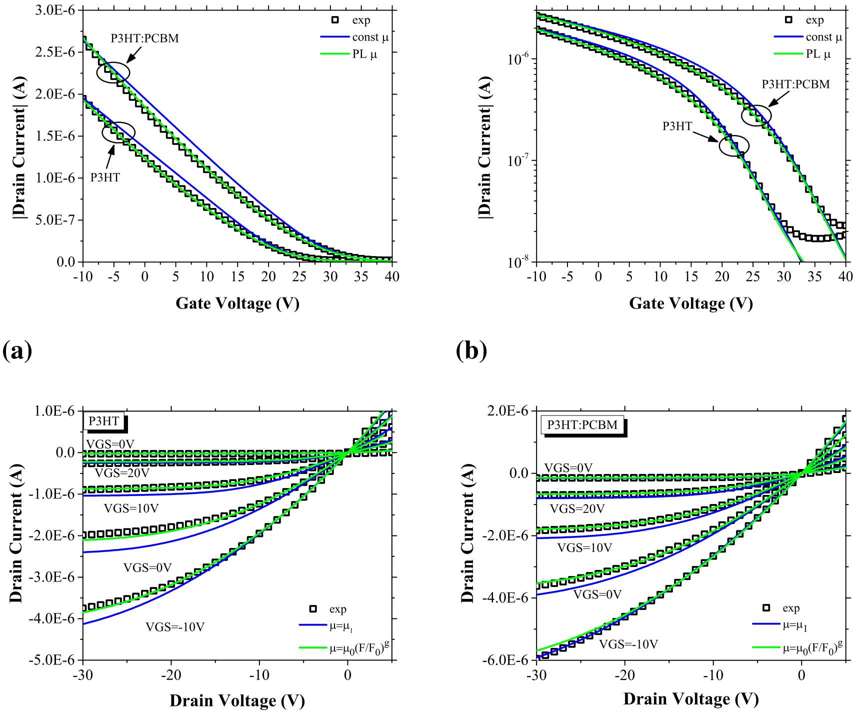

(a) **(b)**

(c) **(d)**

Figure 10: *Experimental and simulated OFETs currents: a) transfer curve (lin. scale), b) transfer curve (log. scale), c) P3HT output curves, d) BHJ output curves.*

data. The constant mobility simulations (blue lines) fail to reproduce the slope of the I_D between the threshold and the maximum current value, as it is evident by the linear scale graph (fig. 10a). On contrast, the PL mobility simulations (green lines) show a perfect match with the experimental data. In this case, μ_p varies from the low-field values of μ_0 to maximum values of $1.3 \cdot 10^{-3}$ $cm^2\ V^{-1}\ s^{-1}$ (P3HT) and $1.6 \cdot 10^{-3}$ $cm^2\ V^{-1}\ s^{-1}$ (BHJ), as obtained when $F_\perp$ reaches approximately $5 \cdot 10^5\ V\ cm^{-1}$.

The output curves (fig. 10d and fig. 10d) have been simulated when the set of parameters in tab. 10 has been established from transfer curves analysis. The enhanced fitting capabilities achieved with the PL mobility (green lines) are evident if compared with the constant mobility simulations (blue lines). This is remarkable considering that no further refinement steps are performed

Table 10: *The parameters employed in OFET DC simulations.*

		Const. Mob.		*PL Mob.*	
Parameter	*Unit*	P3HT	BHJ	P3HT	BHJ
N_{fix}	$[C\ cm^{-2}]$	$-1.8 \cdot 10^{12}$	$-2.2 \cdot 10^{12}$	$-2 \cdot 10^{12}$	$-2.4 \cdot 10^{12}$
$N_{DOS}(E_\mu)$	$[cm^{-2} eV^{-1}]$	$1 \cdot 10^{13}$	$1.3 \cdot 10^{13}$	$2.3 \cdot 10^{13}$	$2.3 \cdot 10^{13}$
$E_{F,i}$-E_μ	$[eV]$	0.32	0.34	0.32	0.36
E_σ	$[eV]$	0.1	0.1	0.1	0.1
x_p=x_n	$[cm^2]$	$1 \cdot 10^{-18}$	$1 \cdot 10^{-18}$	$1 \cdot 10^{-18}$	$1 \cdot 10^{-18}$
μ_p	$[cm^2 V^{-1} s^{-1}]$	$1.5 \cdot 10^{-3}$	$1.7 \cdot 10^{-3}$	n.a.	n.a.
μ_0	$[cm^2 V^{-1} s^{-1}]$	n.a.	n.a.	$1.74 \cdot 10^{-6}$	$1.61 \cdot 10^{-5}$
F_0	$[V cm^{-1}]$	n.a.	n.a.	1	1
ζ	$[1]$	n.a.	n.a.	0.5	0.35

in this regard. It is worth noting how the output curves cross the zero I_D point at zero V_{DS}, which again show how gate leakages are negligible. The effect of interface trap concentration on the transfer curves obtained by simulations is shown in fig. 11.

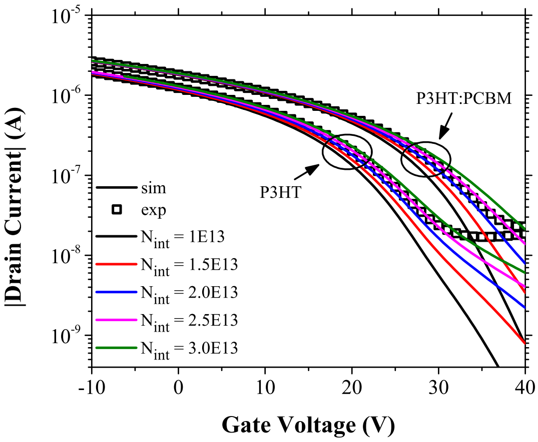

Figure 11: *Simulations of OFETs transfer curves varying the interface traps concentration.*

The V_{TH} shift and subthreshold slope are reproduced by an interface fixed charge N_{fix} of approximately $-2 \cdot 10^{12}\ C\ cm^{-2}$ and a total trap concentration N_T of approximately $2 \cdot 10^{12}\ cm^{-2}$. As the trap concentration is increased, more charge carriers is trapped at the interface, leading to further accumulation of free charge in the channel as traps are of acceptor type. This results in an increase of the drain current. This behavior and the order of magnitude involved are similar to those reported for OFETs realized with small-molecules and polymers (Scheinert et al. (2002, 2007)).

3.3.2 Admittance Analysis

The admittance as measured for the P3HT and P3HT:PC$_{61}$BM OFETs is shown in fig. 12 (symbols), in terms of capacitance and loss functions. The experimental data is compared with the admittance of equivalent circuit models based on *RC* branches. The curves arising from the equivalent circuit admittance are also shown in fig. 12 (line).

A multiple peak behavior is observed in the loss diagrams, where each peak can be associated to a different relaxation process. For the P3HT device, the low-frequency peak shows a dependence in both frequency and magnitude on the applied gate bias, while the high-frequency peak possesses a V_{GS} independent frequency and a magnitude with minor polarization effects. The latter peak is attributed to parasitics in the measurement setup and will not be taken into further consideration. For the BHJ OFET, two peaks and an high-frequency shoulder are visible. The peaks show a frequency and magnitude dependence on the gate bias similarly to the P3HT device, while the shoulder moves below the middle peak for voltage going from positive to negative. It is worth noting how the low-frequency capacitance is approximately equal to C_{ins}, which is 1.15 $F\ cm^{-2}$. On the same way, the high-frequency capacitance is approximately equal to the geometrical capacitance, which is the series combination of C_{ins} and the semiconductor capacitance [23]. The equivalent circuits employed to describe the measured admittance are depicted in fig. 13.

Each *RC* branch is associated to a peak in the loss diagram and the circuit time constant is chosen to match the considered peak relaxation lifetime, i.e. *RC* equal to τ_0. In this context, the dispersion relations of capacitance and loss functions reported in eqs. (84) and (85) for a single-level DOS arise by a series-parallel transformation of the *RC* branch. The values of equivalent cir-

---

[23] For P3HT the value between 10^4 and $10^5\ Hz$ should be considered, since the high-frequency peak is fictitiously dropping the C_P value.

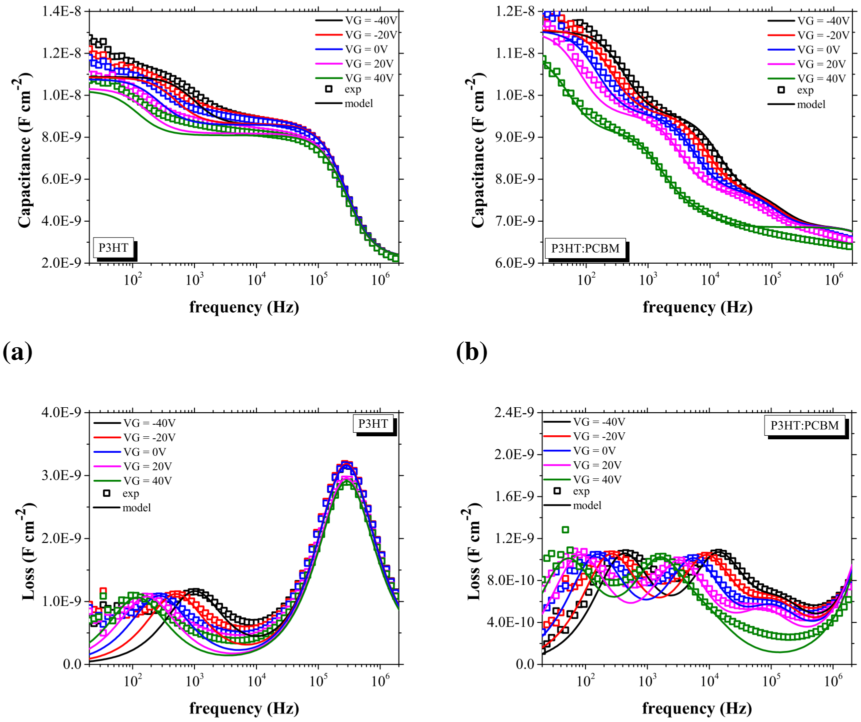

(a) **(b)**

(c) **(d)**

Figure 12: *Experimental and modeled OFETs admittance: a) P3HT capacitance, b) BHJ capacitance, c) P3HT loss, d) BHJ loss.*

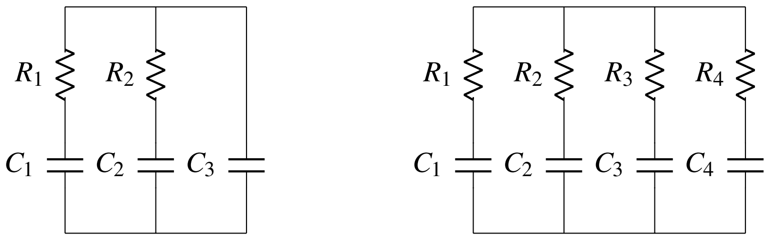

(a) **(b)**

Figure 13: *Equivalent circuits for a) P3HT OFET admittance and b) BHJ OFET admittance.*

cuit model parameters varying the gate bias are reported in tab. 11 (P3HT) and tab. 12 (BHJ). The ones not shown are considered to be constants. In particular, for the P3HT OFET C_3 is 50 pF (base capacitance at high-frequencies), while for the BHJ OFET R_4 is 56.2 Ω and C_4 is 177 pF (base capacitance at high-frequencies).

Table 11: *The parameters employed in P3HT OFET admittance equivalent circuit.*

Parameter	*Unit*	$-40V$	$-20V$	$0V$	$20V$	$40V$
R_1	$[M\Omega]$	3.2	6.6	12.3	19.8	28.5
R_2	$[k\Omega]$	4.06	4.03	4.08	4.34	4.35
C_1	$[pF]$	50.0	48.5	47.5	47.0	46.5
C_2	$[pF]$	138.0	139.0	138.0	129.0	127.0

Table 12: *The parameters employed in BHJ OFET admittance equivalent circuit.*

Parameter	*Unit*	$-40V$	$-20V$	$0V$	$20V$	$40V$
R_1	$[M\Omega]$	7.5	12.0	20.2	37.9	63.7
R_2	$[M\Omega]$	0.24	0.37	0.59	1.01	2.14
R_3	$[k\Omega]$	50.9	56.6	64.3	90.0	1220.0
C_1	$[pF]$	52.5	52.5	52.5	52.5	50.0
C_2	$[pF]$	49.0	48.5	48.0	47.8	46.5
C_3	$[pF]$	21.0	22.5	22.5	22.1	13.0

The equivalent circuits parameter values are chosen to fit the peaks occurring in the loss diagrams and some discrepancies arise due to the model simplification. In particular, the low-frequency dispersion of the capacitance curves is believed to be originated by parasitic effects due to a non-structured semiconductor layer (Nowy et al. (2010)). Furthermore, the peak fit in the loss diagrams is slightly inaccurate between consecutive peaks. This can be associated to the fact peaks are originated by distributed DOS relaxation processes, which are failed to be described accurately by a single-level DOS model due to the broadening of the peaks (Stallinga (2009)). To gain physical insights in the relaxation processes involved in the C_P and L_P diagrams, the admittance of the P3HT and P3HT:PC$_{61}$BM OFETs is also compared with TCAD simulations, as shown in fig. 9.

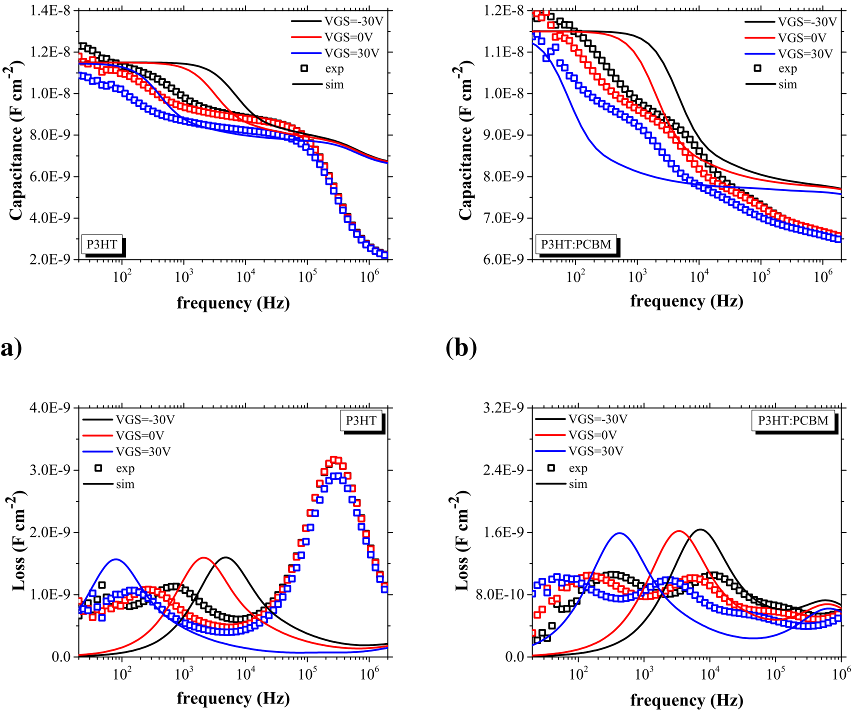

(a) (b)

(c) (d)

Figure 14: *Experimental and simulated OFETs admittance: a) P3HT capacitance, b) BHJ capacitance, c) P3HT loss, d) BHJ loss.*

The simulation framework is identical of that highlighted in section 3.3.1 for a PL mobility. The simulated curves (lines) follow qualitatively the shape and trend of the experimental data. The discrepancies between the two can be related to the degradation of the OFETs between the current and admittance measurements due to ambient factors and electrical stress, which move the V_{TH} of the devices towards further positive voltages. The low-frequency peaks in the loss functions can be attributed to the response of charge in the channel. Owing to a limited lateral flow, this charge is no longer excited when a certain frequency is exceeded. This mechanism originates a drop in capacitance from an accumulated regime (responsive charge) to a depleted regime (unresponsive charge), which is evident as a peak in the loss function (Kim and Kim (2010); Zaki et al. (2014)). In other words, when the excitation frequency is low the free charge carriers in the channel can oscillate between the insulator/semiconductor interface and the source/drain contacts. In this regime, the capacitance is equal to the insulator capacitance C_{ins}. On the other hand, when the excitation frequency is too high the charge cannot reach the insulator/semiconductor interface and C_P decreases to approximately the geometrical capacitance. The drop in C_P originates a dispersion in the loss function whose peak is located at a frequency that can be considered as the amount of time in which free charge carriers vertically travels the device. This interpretation can be further inferred by the effect of interface trap concentration on the loss function, as shown in fig. 15.

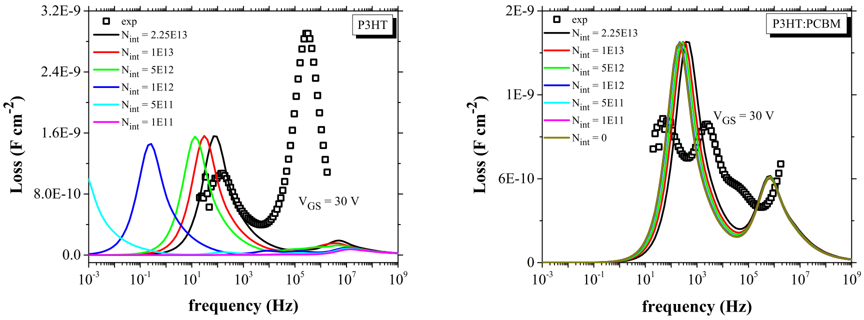

(a) **(b)**

Figure 15: *Simulations of OFETs loss function varying the interface traps concentration.*

The L_P is evaluated in the subthreshold region of the OFETs, i.e. V_{GS} equal to 30 V. As the trap concentration decreases the peaks move to lower frequencies, as the current decreases due to less charge in the channel (fig. 11). This effect is less pronounced in the P3HT:PC$_{61}$BM device since this is characterized by an higher threshold voltage V_{TH} and onset voltage V_{ON}.

Using the relaxation lifetimes for each peak when the device is in accumulation – i.e. V_{GS} equal to -40 V – the hole diffusivity can be estimated as in eq. (86). This yields values of D_p equal to $5.7 \cdot 10^{-8}$ cm^2 s^{-1} for P3HT and $4.3 \cdot 10^{-6}$ cm^2 s^{-1} BHJ. Interestingly, these results suggest the presence of PC$_{61}$BM in the blend aid the vertical diffusivity of holes with respect to the neat P3HT layer. The presence of a double peak in the BHJ device is not well understood. Since this features is not replicated in simulations, it is likely this behavior is related to the morphology of the BHJ, as separated percolation paths can lead to different vertical travel times. Based on this physical understanding, the cut-off frequency f_c for the P3HT and BHJ OFETs can also be estimated by the peak frequency. These values are reported in fig. 16 along with the evaluation of eq. (82).

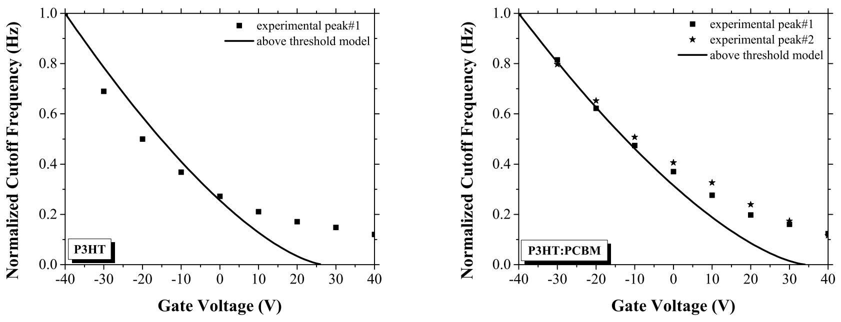

(a) **(b)**

Figure 16: *OFETs cut-off frequencies.*

The cut-off frequencies for P3HT are normalized to $1 \cdot 10^3$ Hz, while those of the BHJ device are normalized to 405 Hz (peak no. 1) and $13.8 \cdot 10^3$ Hz (peak no. 2). The extracted values follow pretty well the calculated f_c behavior when the OFETs are into the accumulation regime, while deviating significantly in the subthreshold region. This can be expected, as eq. (82) follows from the hypothesis of a fully turned-on device. In order to describe this effect, more accurate models could be introduced to take into account the variation of the threshold voltage on traps and interface potential at the insulator/semiconductor interface (Licciardo et al. (2016)).

3.4 Conclusion

In this chapter, Organic Field-Effect Transistors (OFETs) have been used as a testbed device to study the electrical properties of the P3HT:PC$_{61}$BM Bulk Heterojunction. Devices realized using the blended Organic Semiconductor and neat P3HT have been compared to asses the differences due to the presence of PC$_{61}$BM. The OFET were realized as p-type devices on commercial Si/SiO$_2$ substrates by means of spin-coating. Both DC and AC analyses have been performed. The experimental characteristics have been compared to fitting models to perform an analytical estimation of relevant quantities, while physical background has been laid using Technology Computer Aided

Design (TCAD) simulations. Following this approach, important physical parameters have been evaluated.

The curvature of the current-voltage transfer curves in accumulation is well described only if a non-constant mobility is considered. The field-effect mobility μ_{FE} has been estimated to depend over the gate-source voltage V_{GS} with a power-law relationship having a mobility prefactor μ_{FE0} of $2.1 \cdot 10^{-4}$ $cm^2\ V^{-1}\ s^{-1}$. This has been associated to a Power Law hole mobility [eq. (28)] with a low-field mobility μ_0 of $1.74 \cdot 10^{-6}$ ($1.61 \cdot 10^{-5}$) $cm^2\ V^{-1}\ s^{-1}$ and an exponent ζ of 0.5 (0.35) for P3HT (P3HT:PC$_{61}$BM). The presence of PC$_{61}$BM does not influence the hole transport for the employed concentration, as no significant difference between the performance of the neat P3HT OFET and that of the Bulk Heterojunction one has been detected.

The threshold voltage V_{TH} of the devices has been found to be high and positive. This has been associated to the presence of insulator/semiconductor interface fixed charge and traps. Those have been inferred using TCAD simulations to reproduce the subthreshold region of the current-voltage transfer curves. The transfer curve behavior is well described by a fixed charge of $-2 \cdot 10^{12}$ ($-2.4 \cdot 10^{12}$) $C\ cm^{-2}$ and an exponential acceptor trap distribution having peak concentration of $2.3 \cdot 10^{13}$ $cm^{-2}\ eV^{-1}$, $E_{F,i}$-E_{μ} of 0.32 (0.36) eV and E_{σ} of 0.1 eV for P3HT (P3HT:PC$_{61}$BM).

The physical parameters evaluated for current-voltage curves have been directly applied to admittance simulations without any further modifications. The above values well describe the capacitance behavior and the peaks in the loss function [24]. The latter have been associated to the response of free charge carriers in the channel of the devices, and have been used to estimate the hole diffusivity, which has resulted to be $5.7 \cdot 10^{-8}$ ($4.3 \cdot 10^{-6}$) $cm^2\ s^{-1}$ for P3HT (P3HT:PC$_{61}$BM). Furthermore, peak frequencies gives an estimation of the OFETs cut-off frequency f_c, which is approximately 1.0 (0.4-13.8) kHz for the P3HT (P3HT:PC$_{61}$BM) device. Again, the presence of PC$_{61}$BM does not lower the performance of the OFET and also – on the contrary – seems to aid the vertical diffusion of holes and the switching mechanisms of the device. However, the presence of a double low-frequency peak in the P3HT:PC$_{61}$BM OFET is not well understood. This has been associated to the Bulk Heterojunction morphology, as it is not shown in simulations, which are performed

---

[24] Discrepancies between model and measured data arise from device degradation and not optimal model tuning. However, it is worth to point out reaching a fit to measured characteristics does not necessarily mean the values employed for the various parameters have a direct physical meaning or can be transferred to other device layouts or types. The latter point is important when TCAD models are employed for device optimization and design, while in this chapter they have been employed for device analysis only.

using the Virtual Semiconductor approximation.

In conclusion, this chapter gives a full example on how TCAD tools can be applied to the study and analysis of organic devices realized with photoactive Organic Semiconductors.

Chapter 4
The Vertical Organic Transistor

4.1 Introduction

The term Vertical Organic Transistor (VOT) is used to indicate a set of novel device concepts in the organic transistor technology, having in common an operating current that flows perpendicularly to the substrate across the thickness of an organic semiconducting layer. This is opposed to the conventional Organic Field-Effect Transistor (OFET) planar architecture, in which the current flows longitudinally to the substrate between source and drain electrodes.

VOTs have gained interest in the last few years since they are promising in overcoming limitations affecting OFETs, whose performance are strongly dependent on geometrical factors and are limited by the channel length [25]. The channel length cannot be hardly downscaled into the 100 *nm* regime due to issues with contact resistances and processing costs. In VOTs, the thickness of the Organic Semiconductor (OSC) represents the active length of the device. This can be controlled with nanometer precision through common and affordable deposition processes. The VOT reduced active length leads to several benefits: higher output currents, lower operating voltages and a state-of-the-art bandwidths (Lüssem et al. (2015)). The technological processes employed in fabrication and the similar performance of n-type and p-type devices (Lin et al. (2015)) also promote VOTs to an easier integration in complex applications such as displays (Furno et al. (2015)) and nonvolatile memories (She et al. (2017)).

The VOT architecture has also advantages when the devices are exploited as Organic Phototransistors (OPTs). In planar OFETs, the source and drain electrodes must be closely spaced to achieve good electrical performance, resulting in a small photosensitive area which is currently limiting their use as OPTs in real-world scaled applications. In VOTs, the horizontal dimension is

---

[25] The distance between the source and drain electrodes.

unencumbered by performance-related design constraints and can be used to achieve a sufficiently large photosensitive area (Woon and Yeo (2014); Yang et al. (2015); Zan et al. (2011)).

This chapter offers a survey on the VOT subject and shows how numerical simulations are employed to perform a comparison between vertical and planar devices, with the aim of laying a feasibility study for OPT applications.

4.2 State of the Art

Over the years, several concepts for controlling a vertical current in an OSC have been reported. In the following, the nomenclature proposed by Lüssem et al. (2015) will be employed to classify the different types of devices (fig. 17).

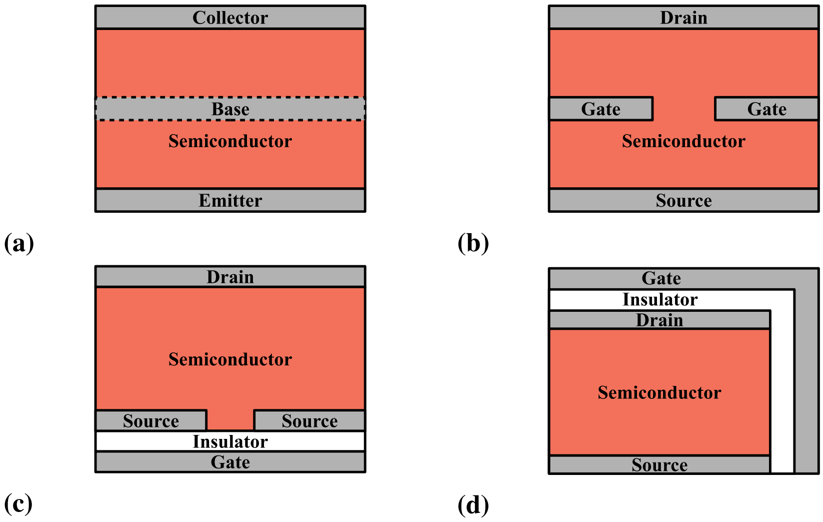

Figure 17: *The various VOT structures: a) OPBT, b) OSIT, c) OSBT, d) VOFET.*

Specifically, VOTs can be divided in:

- Organic Permeable Base Transistor (OPBT) (fig. 17a), in which a control electrode permeable to charge carriers is used to modulate the charge flow between the injection electrodes;
- Organic Static Induction Transistor (OSIT) (fig. 17b), in which a structured electrode is used to create a controllable potential barrier between the injection contacts;

- Organic Schottky Barrier Transistor (OSBT) (fig. 17c), in which the control electrode is placed below the injection electrodes and used to modulate the Schottky barrier width at the source electrode;
- Vertical Organic Field Effect Transistor (VOFET) (fig. 17d), which relies on the field-effect as planar OFET, but combine both vertical and horizontal transport under different device concepts.

Although researchers have a basic understanding of the working mechanisms of these devices, the scaling laws governing VOT are mostly unknown and a realistic estimation of the maximum switching frequency are currently missing. Although these transistors show extremely short channel lengths, which should result in high switching frequencies, their footprint is usually large. This leads to significant capacitances slowing down their high-frequency response.

4.2.1 Organic Permeable Base Transistor

In OPBTs, the charge flow between emitter and collector electrodes is modulated by a third control electrode inserted in between. The latter – referred to as the base [26] – is permeable to charge carriers, hence the name of the device. Electrodes are generally metal foils placed in direct contact with the OSC. Operationally, the current injected at the emitter is transmitted through the permeable base creating a transmission current I_{EC}, which is gathered by the electric field generated at the collector. The current transmission ratio α is defined as in eq. (88) and the current gain β can be evaluated as in eq. (89).

$$\alpha = \frac{I_{EC}}{I_E} \leq 1 \tag{88}$$

$$\beta = \frac{\alpha}{1-\alpha} \tag{89}$$

In principle, a nonzero current flows from the base into the collector and the transmission current is not equal to the collector current I_C, as these leakage has to be accounted for when calculating α. However, if the base-collector parasitic current is low, I_C can be considered a good estimation for I_{EC}.

The switching mechanism of the OPBT is believed to be the electrostatic shielding of emitter and collector through the metal base potential, as confirmed by numerical simulations by Lüssem et al. (2014). On the other hand,

---

[26] The nodes names follows after the BJT.

several mechanisms have been considered for the transmission of charge carriers across the base. Though it has been claimed that hot-electron can be injected across the permeable metal base (Ou et al. (2006)), the high transmission values measured in some devices ($\alpha > 0.99$) suggest that carriers are transmitted through small pinholes in the base electrode (Fischer, Siebeneicher, Kleemann, Leo and Lüssem (2012)), which are naturally formed upon base deposition – i.e. through Physical Vapor Deposition (PVD) techniques – as experimentally determined through Transmission Electron Microscopy (TEM) and Atomic Force Microscopy (AFM) measurements. If the pinholes are small, the metal base is still effective in shielding emitter and collector, modulating the current while retaining an high transmission value. The size of this pinholes can be adjusted by varying the process parameters, leading to device optimization (Kaschura et al. (2015)). Furthermore, it has been established that the on-off ratio R_{OFF}^{ON} of the transistor is increased upon air exposure and/or annealing in air of the metal base. This can be explained considering that the metal oxidation favors the reduction of leakage current between base and collector.

The OPBTs with the best performance are n-type transistors, which have been reported with an R_{OFF}^{ON} of 10^5, β of 180, maximum J_C of 10^3 $mA\ cm^{-2}$ and switching operations at 1.5 MHz. The p-type devices are slightly less performing than the n-type devices, with R_{OFF}^{ON} of 10^5 and β of 77.

These results are summarized in tab. 13. Data for n-type OPBT are taken from Fischer, Scholz, Leo and Lüssem (2012); Fujimoto et al. (2005); Nakayama et al. (2009), while data for p-type OPBT are taken from Umetsu et al. (2013).

From a dynamic viewpoint, OPBT have been compared to conventional planar OFET. A first order analysis pointed out that OFET can switch faster than OPBT if $L_{CH} < 10\ \mu m$. However, the current per footprint area of the OPBT remains approximately constant (although this point is not investigated), while that of an OFET is strongly dependent on material mobility and contact resistance. Furthermore, if OPBT performance are improved by an order of magnitude the switching speed would reach values not accessible by current OFET, unless contact resistance is scaled down. The first systematic modeling study of OPBTs has been performed by Chen et al. (2014). They deduce the intrinsic delay of the transistor from the charging or discharging time of the different regions of the device. Assuming an OSC with μ of 10 $cm^2V^{-1}s^{-1}$, they predict an intrinsic delay well below 1 ns. Even for μ equal to 1 $cm^2V^{-1}s^{-1}$, which is nowadays routinely reached, a delay in the 10 ns regime would be possible.

Table 13: *The salient features of state-of-the-art n-type and p-type OPBTs.*

n-type OPBT	*Parameter*	*Value*	*Unit*
	R_{OFF}^{ON}	$3 \cdot 10^5$	1
	β	180	1
	Max. J_C	10^3	$mA\ cm^{-2}$
	f_c	1.5	MHz
	$\|V\|_{range}$	3	V
p-type OPBT	*Parameter*	*Value*	*Unit*
	R_{OFF}^{ON}	$1.5 \cdot 10^5$	1
	β	77	1

4.2.2 Organic Static Induction Transistor

In OSITs, a grid-shaped gate electrode is buried between the source and drain injection electrodes. The voltage applied to the gate creates an electrostatic potential barrier – referred to as intrinsic gate – that modulates the charge flow in the semiconducting media.

The OSIT has been first exploited by the Kudo group (Kudo et al. (1999, 2000); Watanabe and Kudo (2005)), its concept and nomenclature borrowed from the inorganic Static Induction Transistor (SIT) introduced by Nishizawa and Terasaki (1972). The OSIT features current-voltage characteristics that show a non-saturating shape with increasing drain voltage (Wang et al. (1999)). This happens because the intrinsic gate is lowered by electrostatic induction from the drain, hence the name of the device (Ng (2002)). In that, the OSIT can be considered the organic electronics equivalent of the old vacuum-tube.

The OSIT structures is somewhat similar to that of the OPBTs, with the difference that the base electrode is structured using top-down methods. In several works, Polystyrene spheres have been employed as shadow mask to structure the base electrode, forming holes with diameter around $100-200$ *nm* (Chao, Ku, Tsai, Zan, Meng, Tsai, Horng et al. (2010); Chao, Tsai, Chen, Zan, Meng, Jiang, Chiang and Ku (2009)). With this technique, a β of 10^4-10^5, an $R_{OFF}^{ON} \geq 10^5$ and a maximum J_D of $50-110\ mA\ cm^{-2}$ have been reached. Using a conventional shadow mask with a distance between gate grid branches $L_{PO} \leq 7\ \mu\ m$, transistors with R_{OFF}^{ON} of 10^3 have been reported. These device have been also compared against planar OFET showing better static and dynamic performance (Kudo et al. (2001)). Also in this case, insulating the base leads to significantly increase in the device performance (Chao, Lai, Chen, Meng, Zan and Horng (2009); Chen et al. (2008); Lin et al. (2014)).

The most notable OSIT realizations are summarized in tab. 14. Data are taken from Chao, Chen, Zan and Meng (2010); Chao, Niu, Zan, Meng and Ku (2011); Chao, Tsai, Zan, Hsu, Meng and Horng (2011); Iechi et al. (2010); Watanabe and Kudo (2005); Zan et al. (2012).

Table 14: *The salient features of state-of-the-art OSITs.*

Parameter	*Value*	*Unit*
R_{OFF}^{ON}	$10^3 - 10^5$	1
β	$10^4 - 10^5$	1
Max J_D	$50 - 110$	$mA\ cm^{-2}$
$\lvert V\rvert_{range}$	2	V

The performance of the OSIT are mostly determined by the gate geometry, on which the height of the intrinsic gate depends. The key parameter is L_{PO}, which should be minimized to obtain an higher R_{OFF}^{ON}. From this point of view, promising is the use of novel structuring techniques as nanoimprint lithography, which can lead to very small L_{PO} in the order of $85 - 125$ *nm* (Hsu et al. (2014); Wu et al. (2013)). The underlying switching mechanism has been assumed to be same of that in OPBTs, i.e. shielding of the emitter and collector by the metal base potential. In some works researcher have been argued that this effect is also enhanced by an increase in thickness of a depletion layer around the base (Watanabe et al. (2006, 2007)), however it is reported that depletion region in non-doped OSCs are rather thin (Kleemann et al. (2012)) – in the range of few tenths of nanometers. For which concerns the transport mechanisms leading to non-saturating voltage characteristics, it is believed to be due to Space Charge Limited Conduction (SCLC) (Shockley (1952)) rather than diffusion over the intrinsic gate (Ng (2002)).

4.2.3 Organic Schottky Barrier Transistor

The architecture of the OSBT is different from that of the transistors previously discussed, as the gate electrode is usually placed below the source and separated from it by an insulating layer. A Schottky injection barrier is usually formed at the source/OSC boundary and the gate potential is used to modulate its width in order to accustom the transistor effect.

In order for this to occur, a key technological point is that the source electrode shall be permeable to DC electric fields. This feature has been exploited with three different approaches from as many research groups.

The Yang group employed a metal source electrode with a roughness comparable to its thickness (Ma and Yang (2004)), since a continuous foil would completely screen the gate field from the active layer due to the short Debye length of metals (in the *nm* range). They employed an ionic LiF insulator as gate dielectric and n-type C_{60} as OSC. The latter has been endowed with a 0.7 *eV* Schottky barrier employing an Aluminum source, which also has the advantage of an additional insulating layer of native Al_2O_3 (Xu et al. (2007)). With this setup, Yang and co-workers reported R_{OFF}^{ON} up to $4 \cdot 10^6$ and a maximum J_D of $4 \cdot 10^3$ $mA\ cm^{-2}$ at 5 V. They have also extended their device concept to p-type and ambipolar transistors based on Pentacene (Li et al. (2007)) and P3HT (Li et al. (2008)). Unfortunately, these devices only worked in a humid ambient because of the ionic dielectric. Furthermore, on the ion diffusion process severely limited the frequency behavior of the device.

The Tessler group employed a source electrode structured via shadow masking, using a self assembled block copolymer layer in a lift-off lithographic process. In this way, they managed to obtain openings in the source electrode below 100 *nm* (Ben-Sasson et al. (2009)). Interestingly this device has been optimized by means of numerical simulations, as the employed structuring methods allowed for the direct variations in real devices (Ben-Sasson and Tessler (2011)). Design rules for opening size, aspect ratio and source electrode thickness have been reported by the authors. With this setup, the Tessler group reported R_{OFF}^{ON} of 10^4 and a maximum J_D of of $3 \cdot 10^3$ $mA\ cm^{-2}$ at 3 V.

The Rinzler group employed a CNT source electrode realized by a filtration/transfer method (Liu et al. (2008)). The first devices based on this concept exhibit large hysteresis which can be controlled adding an additional organic charge storage layer placed between the CNT source electrode and the gate dielectric (Liu et al. (2010)). Further implementations reached R_{OFF}^{ON} of $10^4 - 10^5$ and a maximum J_D of 50 $mA\ cm^{-2}$ at 4 V (McCarthy et al. (2010)).

These results are summarized in tab. 15. Data for the Yang OSBT is taken from Ma and Yang (2004); data for the Tessler OSBT are taken from Ben-Sasson et al. (2013, 2009); Ben-Sasson and Tessler (2012); Greenman et al. (2013); data for the Rinzler OSBT are taken from Liu et al. (2010); McCarthy et al. (2010)).

Table 15: *The salient features of the OSBTs reported by Yang, Tessler and Rinzler groups.*

Yang et al.	*Parameter*	*Values*	*Unit*
	R_{OFF}^{ON}	$4 \cdot 10^6$	1
	Max J_D	$4 \cdot 10^3$	$mA\ cm^{-2}$
	$\|V\|_{range}$	5	V
Tessler et al.	*Parameter*	*Values*	*Unit*
	R_{OFF}^{ON}	10^4	1
	Max J_D	$50 - 3 \cdot 10^3$	$mA\ cm^{-2}$
	$\|V\|_{range}$	3	V
Rinzler et al.	*Parameter*	*Values*	*Unit*
	R_{OFF}^{ON}	10^4–10^5	1
	Max J_D	50	$mA\ cm^{-2}$
	$\|V\|_{range}$	4	V

For non-CNT source electrodes, the operational principles of the OSBT are well understood from numerical simulations (Ben-Sasson et al. (2009, 2014); Ben-Sasson and Tessler (2012)). These show that the side facet of the patterned source metal electrode inject charge carriers into the semiconductor upon application of the gate voltage, which results in a thinning of the Schottky barrier due to band bending at the source electrode openings. An accumulation layer is formed at the gate dielectric interface, which is considered a virtual contact for the vertical transport. By application of a drain voltage, a change in the vertical transport from diffusion- to drift-controlled regime can be achieved, with highest current densities obtained above the center of the openings. For the CNT realization, it is known that the height of the Schottky barrier can be also modulated in addition to its width due to the low Density Of States (DOS) of the OSC.

The OSBT has been successfully employed in real world-scaled laboratory applications. McCarthy et al. (2011) employed this device [27] to drive Organic Light Emitting Diodes (OLEDs). The emitting device has been directly integrated on the driving transistor structure by stacking of the respective layers, effectively realizing an Organic Light Emitting Transistor (OLET) with R_{OFF}^{ON}

---

[27] The version with a CNT source electrode.

of $10^3 - 10^4$ for both light and current – comparably to other OLED driving approaches.

Furthermore, the OLED stack has been realized with or without the transistor stack, showing that the latter does not significantly influence the light-emitting performance of the integrated structure. The vertical structure, together with the transparent anode, enables an increased pixel fill factor and a pixel aperture ratio of 98%, which outperform current display realization.

It is important to note that all the reported OSBT employ a native Schottky barrier between the source and the OSC, whose is decreased by the gate voltage to turn the transistor on. However, also normally-on depletion transistors have been realized. In these devices the source-drain current is suppressed by inducing a potential barrier inside the semiconductor, laterally oriented between the patterned electrode and the drain (similarly to what has been argued for OSIT). The performance of these devices are poor if compared to the normally-off transistor due to the non-depletive behavior of OSCs (R^{ON}_{OFF} between 10^1 and 10^3) (Ben-Sasson et al. (2012); Hirashima et al. (2005); Woon and Yeo (2014)).

4.2.4 Vertical Organic Field Effect Transistor

The most investigated VOFET is the so-called step-edge structure, which is identical to the conventional OFET unless for the fact that the channel is formed in a vertical fashion. This is exploited by creating a step in the substrate or in the gate insulator layer prior to the deposition of the OSC (Chen and Shih (2007); Naruse et al. (2008); Parashkov et al. (2003)).

Impressive performance has been achieved using the step-edge configuration, with R^{ON}_{OFF} of 10^6, maximum J_D of 1 $mA\ cm^{-2}$ (Uno et al. (2009, 2010)), $|V|_{range}$ of 1 V and f_c up to 5 MHz (Johnston et al. (2012)). Notably, the step-edge VOFET have also been realized on flexible substrates using epoxy resin pre-patterned structures (Uno et al. (2011)) and bottom thick gate electrodes (Kudo et al. (2010)), with performance comparable to those of devices realized on SiO_2.

The major drawbacks of this simple and elegant device concept are two: i) a less than perfect vertical step-edge will automatically decrease R^{ON}_{OFF} and a lot of effort has to be put on the fabrication process; ii) the step-edge structure does not easily allow for the stacking of OSC and integration with other device is difficult. Considering the latter point, a more recent approach consist to re-adapt a planar BGTC-OFET by stacking other semiconductor layers on top (Nakamura et al. (2006, 2008)). In such a way, the electrodes of the planar

OFET would become the source electrode of the VOFET and the electrode on top of the additional layers will became the drain. Source and drain electrodes are usually insulated by thick layer of SiO_2. Charge carriers are accumulated at the horizontal dielectric interface and migrate along this horizontal plane by diffusion, while transport in the vertical direction happens mainly in the form of drift due to the applied source-drain field. Novel realizations have reached an R_{OFF}^{ON} of 10^6 with an optimized vertical channel (Kleemann et al. (2013)).

4.3 Organic Phototransistor Application

As discussed, VOTs are at an initial stage of development in which structures, technological processes and materials are tailored to increase the transistor performance. Nevertheless, laboratory realizations of real-world scaled applications have been reported, notably highlighting the almost seamless way in which those transistors can be integrated into more complex systems (Furno et al. (2015); McCarthy et al. (2011); She et al. (2017)).

Besides the above reports, VOTs can also be exploited as OPTs, the new frontier in terms of organic photodetectors. OPTs combine the intrinsic advantages of organic electronics, i.e. a chemically-tunable spectral response, low-temperature processes on virtually every substrate and large deposition areas, with the versatility of the transistor effect to target exciting applications, as integrated sensors for Lab-on-a-chip, biomedical X-ray detection, large area scanners on flat and curved surfaces and short-range optoelectronic plastic fiber transceivers (Baeg et al. (2013)).

VOTs are especially prone to be exploited as OPT since they can be realized with an arbitrary photosensitive area [28], the horizontal dimension being free from relevant design constraints (Woon and Yeo (2014); Yang et al. (2015); Zan et al. (2011)). On contrast, the photosensitive area of OFET is limited by the need of a short channel length in order to achieve good electrical performance.

In the following, a modeling study that compares a conventional planar BGBC-OFET (Klauk (2010)) and an OSIT (Wang et al. (1999)) as OPT is proposed. The OFET is taken as a reference device and the OSIT is analyzed to point out weak and strong spot with respect to the former. The comparison is based on computer-based 2D numerical simulations carried out with the state-of-the-art TCAD Sentaurus©(Synopsys (2015)). This approach is based at a

---

[28] Practically, the photosensitive area is limited by the ability of up-scaling the deposition process. Areas of $\sim\ 1\ cm^2$ are easily achievable using state-of-the-art techniques.

deep physical level and allows to highlight the difference in devices behavior for their optimization.

4.3.1 *Simulated Device Structures*

Schematics of the simulated structures are shown in fig. 18. Unless specified, all the materials are explicitly taken into account. The OSC is the widely studied P3HT:PC$_{61}$BM BHJ, as this gives the possibility to build up a consistent model for the active material – supported by a wide literature of experimental data and use in real devices – to be employed as proof-of-concept. The modeling approach followed here for this material is that of the VS (see section 2.5.2). Both transistors feature an Al/Al$_2$O$_3$ insulated gate [29] with 5 *nm* Oxide thickness and a 500 *nm* OSC thickness.

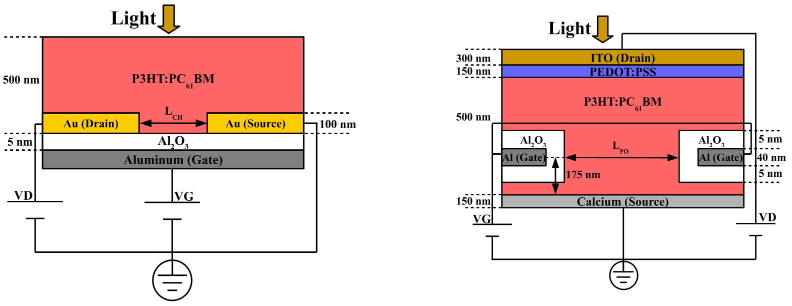

(a) **(b)**

Figure 18: *Simulated OPT structures (not in scale): a) BGBC-OFET, b) OSIT.*

For what concerns the OSIT (fig. 18a), an hole-injecting ITO/PEDOT:PSS drain and an electron-injecting Ca source are considered. The gate is vertically placed 175 *nm* away from the latter and simulations have been performed varying the spacing between adjacent gate branches (i.e. L_{PO}) in the $100 - 400$ *nm* range. Note only a limited vertical section is taken into account for simulations, since the gate is periodically arranged along the structure.

For the OFET (fig. 18b), hole-injecting source and drain contacts (Gold) are considered. The channel length L_{CH} is taken to be $5 \mu m$, as often the case in real devices. The geometric form factor of the OFET is evaluated as the channel width W_{CH} divided by the channel length L_{CH}. For 2D simulations, Sentaurus©considers a default extruded distance in the z direction of $1 \mu m$,

---

[29] The thin Al$_2$O$_3$ layer can be considered as native oxide (Kaschura et al. (2015)).

which in this case is identified as W_{CH}. In addition, the Al layer forming the gate electrode is only accounted for by using proper electrical and optical boundary conditions. The material models employed in simulations are specifically introduced into the TCAD database as reported in section 2.6.

4.3.2 Tuning the Bulk Heterojunction Model

The model of the P3HT:PC$_{61}$BM BHJ has been refined for OPT simulations with respect of that contained in section 2.6. In particular, electron and hole trap distributions are added in the bandgap of the Virtual Semiconductor (VS). In the bulk material, Gaussian donor and acceptor trap distributions are taken into account to model the structural disorder of the material. For the OSIT, two Exponential donor distributions and a fixed charge density are also added at the PEDOT:PSS/blend junction to describe interface imperfections (Popescu et al. (2013)). Trap distributions and physics are introduced in section 2.2.4.

In order to fine tune electrical and optical parameters of the Bulk Heterojunction (BHJ) model, a reference Organic Photodiode (OPD) is simulated and results are compared with existing experimental and theoretical studies. The OPD layers are identical to that of the OSIT architecture reported in fig. 18a. The relevant parameters used for trap distributions are summarized in tab. 16 and tab. 17, with similar values are reported by Popescu et al. (2013). The employed fixed charge density N_{fix} value is $2 \cdot 10^{13}$ $C\ cm^{-2}$.

Table 16: *P3HT:PC$_{61}$BM BHJ bulk traps model values.*

	N_T $[eV]$	$N_{DOS}(E_\mu)$ $[cm^{-3}eV^{-1}]$	$E_{F,i}$-E_μ $[eV]$	E_σ $[eV]$	x_p=x_n $[cm^2]$
Donor	$2.5 \cdot 10^{18}$	$1 \cdot 10^{19}$	-0.22	0.1	$1 \cdot 10^{-19}$
Acceptor	$2.5 \cdot 10^{18}$	$1 \cdot 10^{19}$	0.22	0.1	$1 \cdot 10^{-19}$

Mobilities are chosen to be constant and equal to $3 \cdot 10^{-4}$ $cm^2\ V^{-1}\ s^{-1}$, both for electron and holes. These values are in the range of that experimentally determined and/or used in different simulation approaches (Deibel, Wagenpfahl and Dyakonov (2008); Klauk (2010); Koster et al. (2005)). The quantum yield of the P3HT:PC$_{61}$BM BHJ is considered as γ = 0.5, in agreement with Piris et al. (2009).

The dark current of the OPD is shown in fig. 19c, while varying mobilities

Table 17: *P3HT:PC$_{61}$BM BHJ interface traps model values.*

	N_T $[eV]$	$N_{DOS}(E_\mu)$ $[cm^{-3}eV^{-1}]$	$E_{F,i}$-E_μ $[eV]$	E_σ $[eV]$	x_p=x_n $[cm^2]$
Dist. no. 1	$2 \cdot 10^{13}$	$1 \cdot 10^{14}$	0.3	0.1	$1 \cdot 10^{-18}$
Dist. no. 2	$2 \cdot 10^{13}$	$1 \cdot 10^{14}$	0.1	0.1	$1 \cdot 10^{-18}$

and adding trap distributions. It is evident how this parameters strongly affect the current of the OPD. The green curve is relative to the final model and it is calculated with μ equal to $3 \cdot 10^{-4}$ cm^2 V^{-1} s^{-1}. Other curves are calculated with μ equal to $1 \cdot 10^{-3}$ cm^2 V^{-1} s^{-1}. The OPD has also been simulated under illumination conditions with an impinging monochromatic light source having power density of 1 μW cm^{-2} and wavelength varied between 300 nm and 800 nm. The External Quantum Efficiency (EQE) of the device is calculated for an anode voltage of -5V using geometrical optics. This is shown in fig. 19d, along with the extinction coefficient taken from the literature.

The simulation results are in good agreement with experimental reports of OPDs for the same thickness of the BHJ layer (Falco et al. (2014)). As can be seen in the band diagram of fig. 19b, bulk traps are responsible for the increase in reverse dark current due to the creation of leakage paths in the VS. On the other hand, interface traps and fixed charge decrease the forward current by lowering the hole accumulation, which is equivalent to an increase in the injection barrier between the PEDOT:PSS and the VS.

4.3.3 Current-Voltage Analysis

The current-voltage characteristics for the simulated OFET and OSIT are reported in fig. 20. These are evaluated under dark conditions.

The output and transfer curves of the OFET are reported in fig. 20a and fig. 20b respectively. They assume the shape of a typical p-type device, with no ambipolar transport observed due to the high electron injection barrier (1.3 eV). As figures-of-merit, the field effect mobility μ_{FE} and the threshold voltage V_{TH} can be estimated by approximation of the Charge Control Model (CCM) model to the linear region of the transfer curve, as shown in fig. 20b. For details, please refer to section 3.2 and eq. (64). Using this method, μ_{FE} is $1.27 \cdot 10^{-4}$ cm^2 V^{-1} s^{-1}, which is in good agreement with the bulk mobility values employed. On the other hand, V_{TH} is -1.69 V.

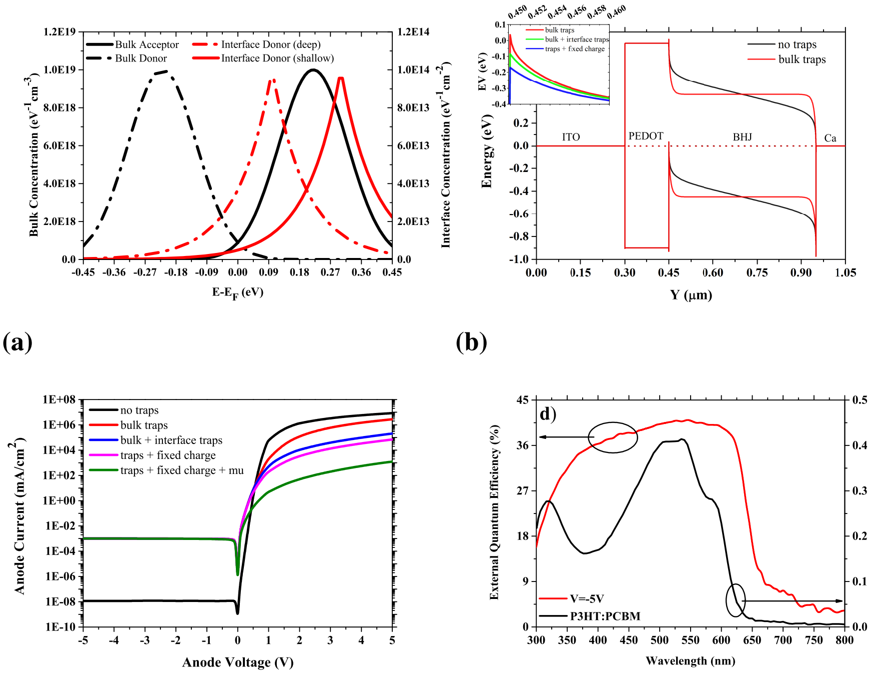

(a) **(b)**

(c) **(d)**

Figure 19: *Reference OPD simulations: a) trap distributions, b) band diagram (equilibrium), c) dark currents, d) k and EQE.*

The output curves of the OSIT are reported in fig. 20c for $L_{PO} = 100\ nm$ and several values of V_G. The transfer curves are reported in fig. 20d for $V_D = 5\ V$ and L_{PO} varied between between $100\ nm$ and $400\ nm$.

As can be observed, the device cannot be fully turned off due to an incomplete static induction effect. From the output curves is evident that a significant amount of current flows for $V_G = -1\ V$ when the device is forwardly biased, while from the transfer curves it can be observed how the V_G effect saturates at approximately $-3\ V$ giving rise to the residual baseline current. This behavior will be better explained by analyzing the band diagram in section 4.3.4.

The modulation effect of V_G can be quantitatively evaluated with the definition of a threshold voltage V_{TH} and a normalized transconductance g_m. A rather empirical evaluation is employed here, as shown in fig. 20d. A linear extrapolation of the J_D in the low-V_G regime is evaluated. The intercept with the baseline current (i.e. the current at which the modulation of the gate voltage is ineffective) is referred to as V_{TH}, while the slope is defined as g_m. For

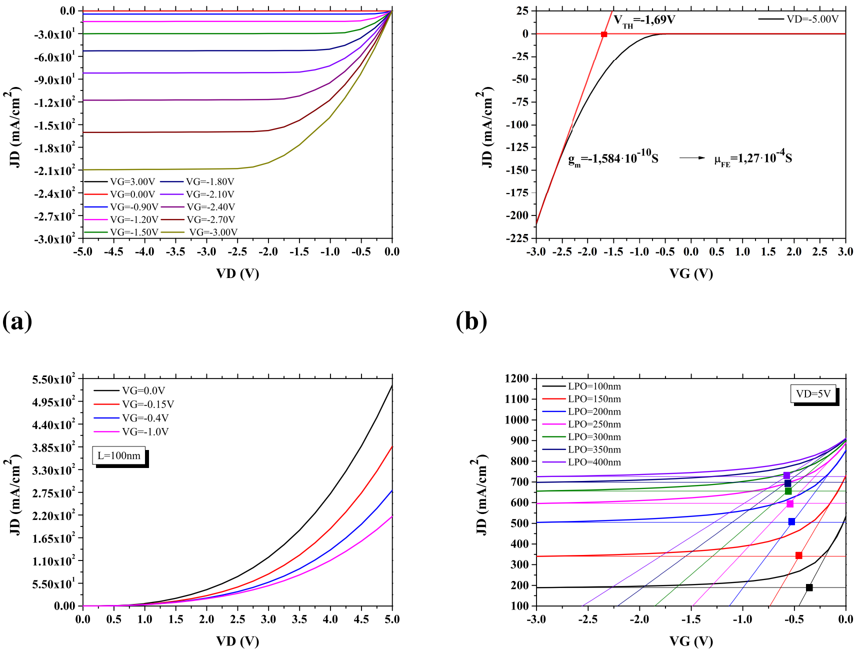

(a) **(b)**

(c) **(d)**

Figure 20: *J-V Characteristics: a) OFET output curves, b) OFET transfer curves, c) OSIT output curves, d) OSIT transfer curves.*

$L_{PO} = 100\ nm$, $V_{TH} = -0.57\ V$ and $g_m = 325\ mS\ cm^{-2}$ are found.

4.3.4 Band Diagram

The residual baseline drain current and the incomplete static induction of the OSIT can be justified by looking at the band structure of the device, as shown in fig. 21. All diagrams are displayed for L_{PO} equal to 100 *nm* except for what concern the space charge distribution of fig. 21c, which is evaluated for L_{PO} equal to 150 *nm*.

The band diagram at equilibrium (i.e. zero V_D) is shown in fig. 21a. The curves are taken by cutting the OSIT structure along the x dimension, 10 *nm* away from the gate insulator inside the semiconductor. The intrinsic gate barrier is clearly visible near the source electrode for negative V_G biases, as shown in the inset. However, by looking at the space charge distribution between gate

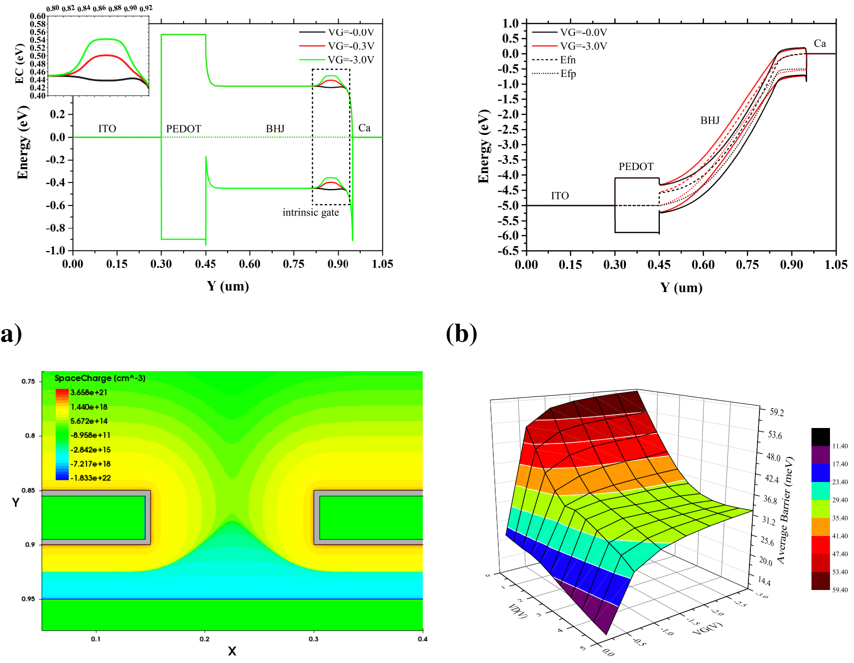

(a) **(b)**

(c) **(d)**

Figure 21: *The band diagram of the OSIT a) in equilibrium and b) under a drain bias; c) the space charge in the pinch-off region; d) the average intrinsic gate barrier.*

branches (fig. 21c), it can be concluded that the intrinsic gate is only formed near the gate insulator and the pinch-off region cannot be fully depleted of carriers – which translates in the impossibility of turning off the transistor. This can be attributed to the high trap concentration in the bulk of the VS.

In addition, the modulation effect of the gate voltage is greater at lower drain voltages. This is explained by considering the spatial average of the intrinsic gate barrier computed in the pinch-off region, which is shown in fig. 21d as a function of both V_G and V_D. As can be inferred, the average intrinsic gate decreases with increasing V_D as a result of the static induction from the drain. This causes the gate modulation effect on the average intrinsic gate barrier to be lower, with consequently lower drain current modulation. Note that the behavior is qualitatively the same for higher L_{PO} values.

The V_G-V_D interdependence is also visible in the band diagram out of equilibrium (fig. 21b), where the intrinsic gate barrier almost disappears under the influence of a positive V_D ($5\ V$), its effect being only that of pinning the energy bands in a way to influence the potential distribution and thus the current.

4.3.5 External Quantum Efficiency

The OFET and the OSIT have been simulated under illumination conditions to exploit their behavior as OPT. The EQE of the devices are calculated using geometrical optics, with an impinging monochromatic light source having power density of $1\ \mu W\ cm^{-2}$. The wavelength of the source is varied in the $300 - 800\ nm$ range. The relative diagrams are shown in fig. 22. Note that the EQE of the OSIT is shown for $L_{PO} =\ 100\ nm$, but no substantial changes in quantity and behavior are found for higher L_{PO} values.

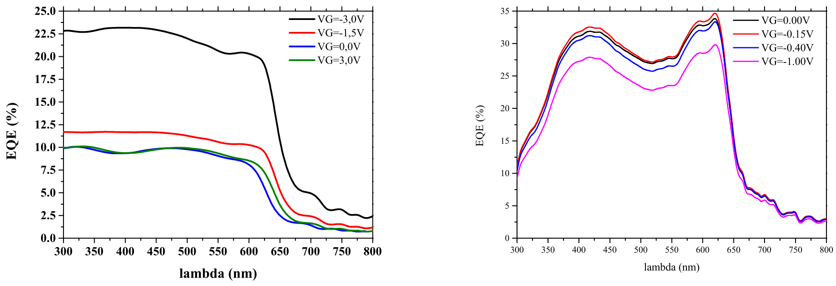

(a) **(b)**

Figure 22: *The EQE of a) the OFET and b) the OSIT.*

As can be observed, the OSIT performs better than the OFET, gaining an average 10% efficiency in the visible range of wavelengths [30]. This performance mismatch can be related to devices architecture.

In both transistors, charge carriers are equally generated upon photon absorption in the whole photoactive material, their number depending on the intensity of the propagating light beam.

For the OFET however, only carriers generated inside the channel region can be effectively collected by the drain-source electric field to create a photocurrent. Carriers generated elsewhere only give a small contribution, since they can move by diffusion for about $10\ nm$ prior to recombination (Wang et al. (2011)). This means that the majority of generated charge gets lost in the semiconductor bulk.

---

[30] It is worth noting how the V_G only little affects the overall OSIT EQE (changes confined within few percents), while this effect is more prominent for the OFET.

On the other hand, in the OSIT the majority of carrier are subjected to the drain-source electric field, since the semiconductor is entirely stacked between electrodes – showing a behavior very much similar to that of the OPD simulated in section 4.3.2.

The OFET EQE is rather flat if compared to that of the OSIT. Again, this is imputable to devices architecture and in particular to different filtering effects due to resonance at optical frequencies (Han et al. (2005)), as in the latter case the BHJ is stacked between semitransparent/opaque electrodes in the propagation direction of the impinging beams while this is not the case for the OFET.

4.3.6 Performance Improvements

As discussed in the previous sections, the OSIT cannot be turned off due to an incomplete static induction effect which originates a residual baseline drain current. This as been imputed to the high trap concentration characterizing in the P3HT:PC$_{61}$BM VS. From this point of view, performance can be improved by shaping the gate grid differently from the conventional coplanar architecture. This concept is shown in fig. 23.

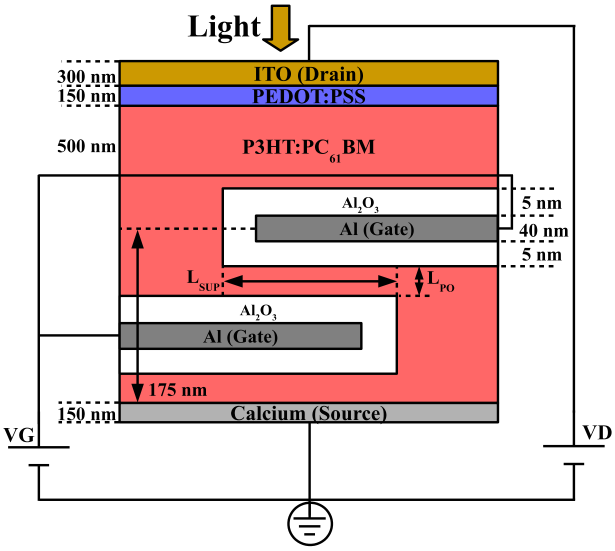

Figure 23: *The staggered-gate OSIT structure.*

Here – differently from the structure of fig. 18a – the wires of the grid are staggered and partially superimposed. The L_{PO} distance can now be considered as the vertical spacing between the wires and a new geometrical quantity is introduced as L_{SUP} – i.e. the length for which the staggered gate wires superimpose to each other.

The simulations of the staggered-gate OSIT are reported in fig. 24 for L_{PO} equal to 50 *nm* and L_{SUP} equal to 100 *nm*.

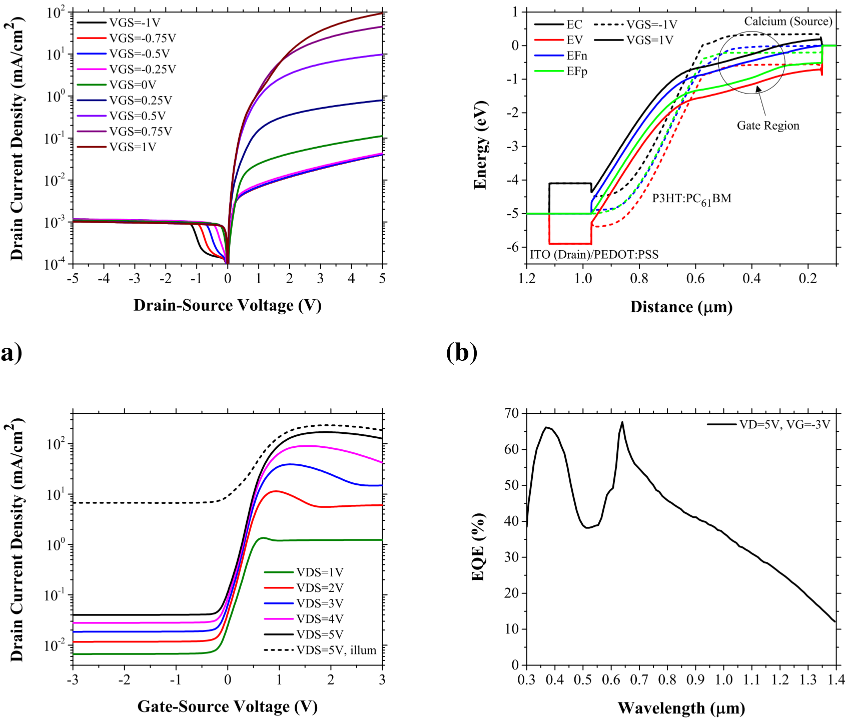

(a) **(b)** **(c)** **(d)**

Figure 24: *Simulations of the staggered-gate OSIT: a) output curves, b) band diagram, c) transfer curves, d) EQE.*

As can be observed from the output curves of fig. 24a, the current of the device follows a diode-like shape, with a forward-to-reverse drain current ratio of approximately 10^5. The gate voltage acts on the drain by primarily controlling the forward current, which can be switched almost down to the reverse current by applying a negative V_G of $-1\ V$.

The device turn-off mechanism is attributable to a drain-to-source shielding effect rather than the creation of an intrinsic gate barrier, as shown in the band diagram of fig. 24b [31]. For V_G equal to $-1\ V$ the bands are rather flat in the gate region near the source and carriers get considerably slowed down, leading to a small current. On the opposite, bands show an appreciable slope for V_G equal to $1\ V$, which means the drain voltage is no longer shielded from the source. Charge carriers can now get past the gate region with a sensible speed, leading to an on-state current much greater than the off-state one.

The R_{OFF}^{ON} of the staggered-gate OSIT is greater than 10^3, as can be observed in the transfer curves of fig. 24c. Interestingly, the drain current shows a negative differential transconductance region which broadens as the drain voltage is increased. This effect has not been cleared yet and it is still under investigation. Reported on the same diagram is the photocurrent originated by an AM1.5G solar spectrum for V_D equal to $5\ V$. The illuminated-to-dark current ratio is of approximately two orders of magnitude, which is more than sufficient for most OPT applications.

The EQE of the device is shown if fig. 24d. The magnitude of the EQE goes well beyond the quantum yield of the BHJ (i.e. $\gamma = 0.5$) with peaks of 70/80% [32], keeping to high values even in the Near Infrared (NIR) portion of the spectrum. This effect is still under investigation and can be allegedly associated with a photoconduction gain mechanism (Baeg et al. (2013)). This is in contrast with OFET and coplanar OSIT simulations, where the EQE never exceeds 35% and abruptly drop-off around 650 *nm*.

4.4 Conclusion

Vertical Organic Transistors (VOTs) have gained interest in the last few years since they are promising in overcoming limitations affecting Organic Field-Effect Transistors (OFETs), especially from the viewpoint of achieving channels length controlled with nanometer precision through affordable processing. Several benefits have been demonstrated in the state-of-the-art, as low operating voltages, high output currents and bandwidths. These devices possess an operating current that flows perpendicularly to the substrate across the thickness of an organic semiconducting layer, opposed to conventional planar transistors in which the current flows longitudinally to the substrate. VOTs have also advantages towards OFETs also when exploited as Organic Phototransistors (OPTs), since a very large photosensitive area can be achieved.

In this chapter, numerical simulations have been used to perform VOT

---

[31] The band diagram is evaluated considering a rotated S-shaped cut-line running from the drain through the staggered gate wires spacing to the source, for $V_D = 5\ V$.

[32] The peaks in the EQE shape correspond to the analogous found in the P3HT:PC$_{61}$BM α_{abs}

analysis and optimization with respect to light sensing applications. A comparative study between Organic Static Induction Transistor (OSIT) and OFET OPTs based on the P3HT:PC_{61}BM Bulk Heterojunction has been given, highlighting commonalities, strengths and weaknesses of both devices. For the modeling of the Bulk Heterojunction system, a Virtual Semiconductor approach has been employed.

As shown in the analysis, both OPTs show similar dark electrical performance in terms of threshold voltage and field-effect mobility. However, the OSIT cannot be completely turned off. This is due to an incomplete static induction effect in which the intrinsic gate is only formed near the gate insulator and the pinch-off region cannot be fully depleted of carriers. This can be attributed to the high trap concentration in the bulk of the Virtual Semiconductor, which models the high structural disorder of the material.

On the other hand, the OSIT OPT performs much better than the OFET one under illumination condition, with an average increase in External Quantum Efficiency of 10% over the visible spectrum. The reason for that is to be sought in the different device structures, being the OSIT more prone to collect photogenerated carriers. For the OFET, only carriers generated inside the channel region can be collected by the drain-source electric field. For the OSIT, this electric field is applied to most of the carriers since the device is entirely stacked between electrodes – much like an Organic Photodiode. The comparison of these two structures is qualitatively in line to what experimentally found by Yang et al. (2015) for Pentacene.

Improvements to the OSIT performance can be achieved by changing the gate metal grid to take on a staggered architecture, where adjacent gate wires are placed on different vertical planes and partially superimposed. With the staggered-gate structure, an on-off ratio greater than 10^3 can be attained, while the illuminated-to-dark current ratio is approximately of 10^2. Furthermore, this device shows photogain mechanisms as the External Quantum Efficiency of the device exceeds the quantum yield of the P3HT:PC_{61}BM Bulk Heterojunction with peaks of 70/80%, retaining high values even in the Near Infrared region of the spectrum. This is in contrast with previous OSIT simulations, where the External Quantum Efficiency never exceeds 35% and abruptly dropoff around 650 *nm*.

Chapter 5
The Polarized Organic Photodiode

5.1 Introduction

Organic electronics allow for materials that absolve multiple purposes in their usage. They can be deposited on a broad range of substrates – from the most conventional as glass and Silicon, to the most unpredictable as fabric and biological tissues. They can achieve a broad-range of properties as light-emission/absorption, fairly high conductivities, conformal shape to bendable surfaces, encapsulation and biocompatibility. They can be manufactured with low-cost techniques as spray-coating, inkjet printing, and doctor blading, suitable to continuous-flow manufacturing processes like roll-to-roll and integrable with novel technologies like 3D printing. All these aspects are highly interesting from the point of view of creating devices with new functionalities, in which several components are monolithically integrated to seamlessly work together.

In this chapter, these concepts are applied to the design and analysis of a novel organic electronic device – namely the Polarized Organic Photodiode (POPD), i.e. an Organic Photodiode (OPD) in which the current is sensitive to incident light polarization. A methodological approach based on numerical simulations is here employed in order to assess first-hand design parameters and minimize the experimental trial-and-error effort. Simulations are then compared to the fabricated POPD data to analyze its behavior and identify factors important to device optimization.

5.2 State of the Art

Polarization specifies the geometrical orientation of the electromagnetic field associated with light. This characteristic can be exploited for sensing, since changes to a known polarization can be caused by physical and geometrical properties of a particular object of interest, or polarization can be auxiliary used to improve and enhance the signal-to-noise ratio on a certain receiver (Snik et al. (2014)).

Measurement techniques based on light polarization have been exploited in several fields and applications as atmospheric remote sensing (Deschamps et al. (1994)), target detection (Tyo et al. (1996)), astronomy (Rodenhuis et al. (2012)), biomedical diagnostic (Jacques (2013); Novikova et al. (2012)), zoology (Johnson (1995)) and many others.

Organic devices have been employed in polarization sensing for Lab-on-a-Chip (LoC) applications (Williams et al. (2014)). Here, they have been applied by Banerjee et al. (2008) and Pais et al. (2008) to the fluorescence study of antigen/antibody biological systems. These works use a cross-polarization scheme, illustrated in fig. 25, to allow detection of small dye concentrations inside the solution under investigation.

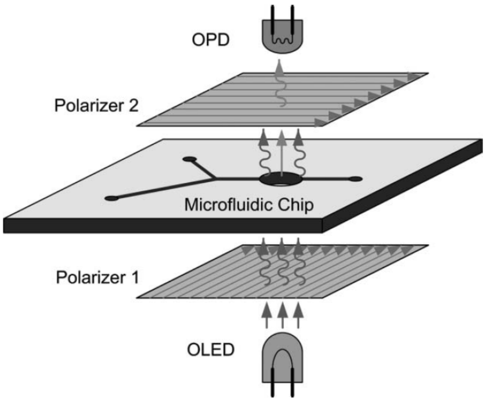

Figure 25: *OLED/OPD cross polarization scheme for LoC analytic applications (Pais et al. (2008)).*

The excitation light is sourced by an Alq_3-based OLED. This gets through a first polarizing film before reaching the microfluidic chip, where it impacts upon the solution containing the dye, stimulating its emission. A second polarizing film, orthogonally oriented with respect to the first, is responsible of filtering out the excitation light and retrieving part of the emission. A C_{60}/CuPc-based OPD is then used to measure the intensity of the dye fluorescence.

To achieve this cross-polarization scheme, the authors have mechanically attached commercially-available polarizing films to previously fabricated organic devices via glues or adhesives. However, this process is cumbersome, poorly suitable for manufacturing, characterized by heavy insertion losses and high-noise due to environmental factors.

To overcome current state-of-the-art limitations, it is instead possible to monolithically integrate a polarizing layer directly inside a conventional OPD device, as it is discussed in the following.

5.3 Monolithic Integration

The POPD concept – in which the monolithic integration between a polarizing layer and an OPD device is realized – is shown in fig. 26.

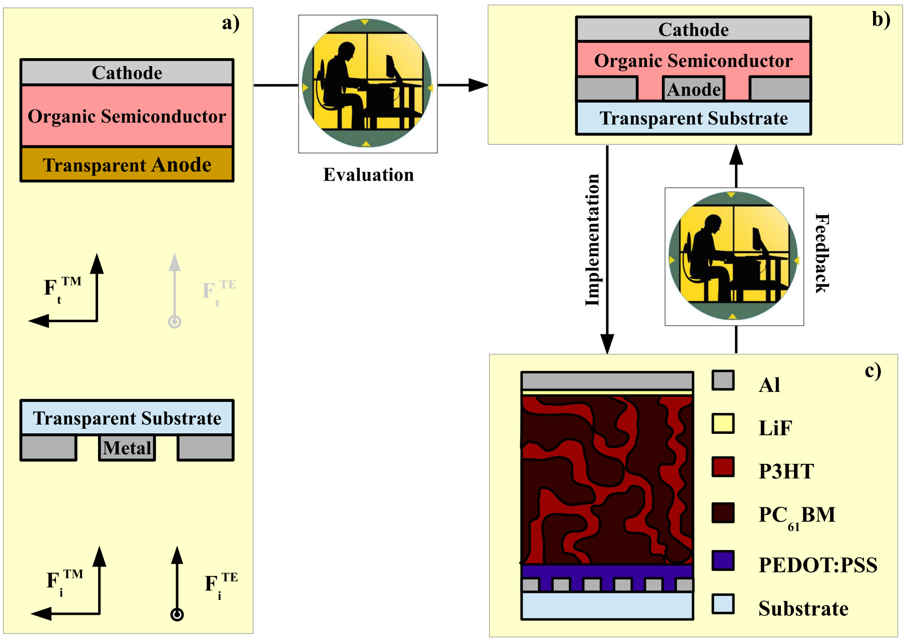

Figure 26: *Monolithic integration of a POPD: a) application of a WGP, b) integration of a WGP, c) realization of the POPD.*

The Wire Grid Polarizer (WGP) has been identified as a suitable candidate to perform the polarization of the light impinging on the OPD (fig. 26a).

The WGP is a type of linear polarizer constituted by a great number of parallel metallic lines in a plane, i.e. the wires, closely spaced among each other. If the electromagnetic wave associated with the incident light is polarized in the Transverse Electric (TE) mode, electrons are driven along the wires generating a forward traveling wave which cancels the incident one. On the other hand, for Transverse Magnetic (TM) polarization electrons cannot move through the metal across the wires – provided the grid spacing is smaller than the wavelength of the incident light (Hecht (2002)). As a consequence, WGPs can take as input an randomly polarized incident light, transmit the TM component and reflect the TE one. For this reason, they can also be employed as polarization beam splitters (Yu and Kwok (2003)).

A WGP can be integrated inside an OPD by conveniently patterning the anode metal of the device to assume a grid-shaped layout. Using the correct spacing among the wires and an appropriate metal thickness, the grid can be suitable to perform as both WGP and electrical contact (fig. 26b). The POPD concept can be implemented for a conventional P3HT:$PC_{61}BM$-based OPD (Falco et al. (2014)), in which a LiF/Al cathode and a PEDOT:PSS anode are used to facilitate the extraction of electrons and holes respectively (fig. 26c).

Being this a device architecture never realized before, a methodological approach based on numerical simulations has been employed in order to realize a proof-of-concept POPD implementation. The first step consists in the evaluation of WGP and OPD characteristics in order to asses the influence of architectural parameters on the POPD behavior. The second step consists in bringing into the model feedback from the proof-of-concept POPD implementation in terms of simulations refinement based on the experimental data.

5.3.1 Device Evaluation

In first instance, WGP simulations have been carried out solving Maxwell's equations with Finite-Difference Time-Domain (FDTD) methods (Taflove and Hagness (2005)), for both a single-layer and bi-layer architectures and a range of metals employed in organic electronics, i.e. Aluminum, Gold and Silver. The best performance have been assessed for an Aluminum bi-layer WGP, having employed squared wires with a metal thickness of 45 *nm* and a 50% duty cycle between upper and lower grids in the simulated structure. Details about those simulations can be found in Falco (2016). The WGP is characterized in terms of the Polarization Extinction Ratio (PER), as reported in eq. (90).

$$PER = \frac{T^{TM}}{T^{TE}} \tag{90}$$

Here, T^{TM} and T^{TE} are the TE and TM transmissions, respectively. Those are defined in eqs. (91) and (92) in terms of incident electric fields (F_i^{TM} and F_i^{TE}) and transmitted electric fields (F_t^{TM} and F_t^{TE}).

$$T^{TM} = \frac{\left|F_t^{TM}\right|^2}{\left|F_i^{TM}\right|^2} \tag{91}$$

$$T^{TE} = \frac{\left|F_t^{TE}\right|^2}{\left|F_i^{TE}\right|^2} \tag{92}$$

The transmissions and PER for the Aluminum bi-layer WGP in the visible spectrum are reported in fig. 27. The PER is contained between 10^2 and 10^4 mainly because the TE mode gets heavily reflected.

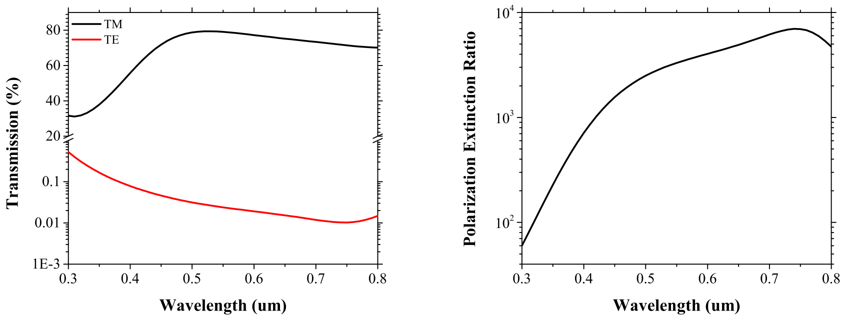

(a) **(b)**

Figure 27: *WGP FDTD simulations: a) transmissions, b) PER.*

The transmission values obtained by FDTD are directly employed for device simulations. The state-of-the-art TCAD Sentaurus©(Synopsys (2015)) is exploited to this purpose. The simulated POPD structure is schematically shown in fig. 28.

For the modeling of the P3HT:PC$_{61}$BM Bulk Heterojunction (BHJ), the Virtual Semiconductor (VS) approach is employed (see section 2.5.2). The material parameters are reported in section 2.6 and have been specifically added to the TCAD database. The model is refined by adding trap distributions, as previously specified in section 4.3.2. The quantum yield of the VS is chosen to be 0.5 and mobilities are considered equal to $3 \cdot 10^{-4}\ cm^2\ V^{-1}\ s^{-1}$, for both electron and holes. The proper workfunctions and complex refractive indexes are selected to model electrical and optical boundary conditions. In addition, the

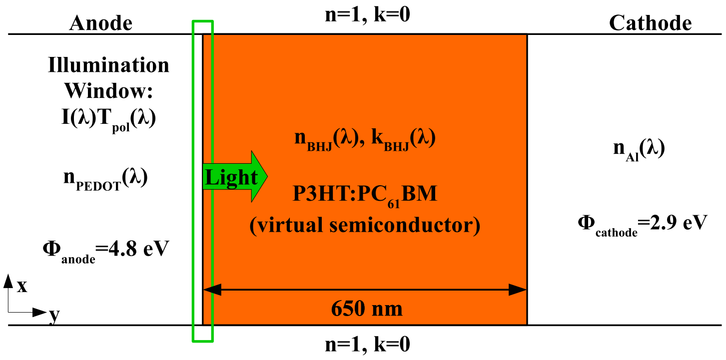

Figure 28: *POPD structure in TCAD simulations.*

transmissions are directly used to conveniently filter the illumination source to account for the WGP behavior. The simulation flow is shown in fig. 29.

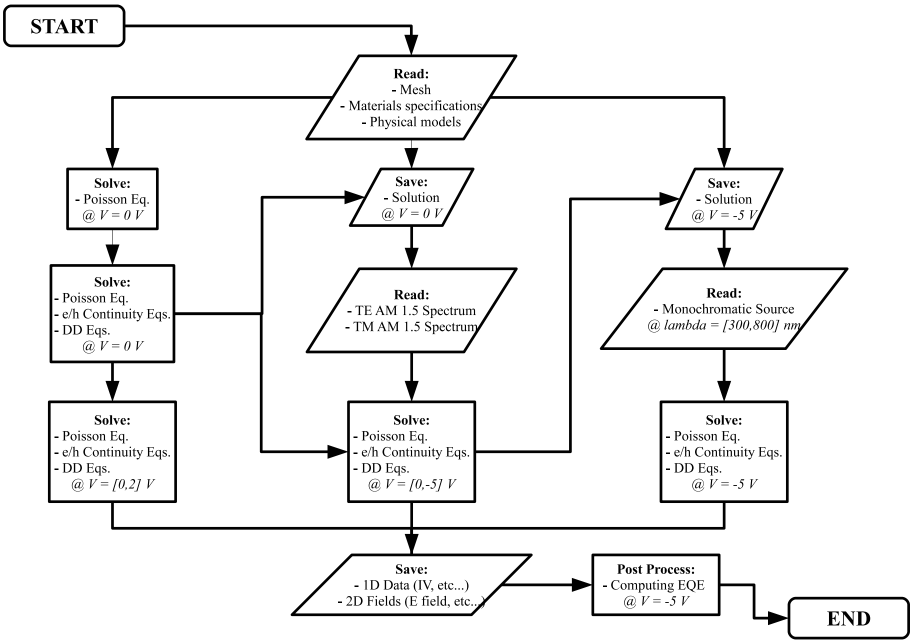

Figure 29: *A diagram showing the flow of POPD TCAD simulations.*

Three sets of simulations are performed, i.e. i) dark current simulation, ii) photocurrent simulations, iii) External Quantum Efficiency (EQE) simulations. In first place, dark current simulations are effectuated, ramping the anode voltage from $-5\ V$ to $2\ V$. In this context, bias points for the equilibrium (i.e. anode voltage equal to $0\ V$) and reverse (i.e anode voltage equal to $5\ V$) conditions are saved. The photocurrent simulations consider an AM1.5G solar spectrum filtered-out using WGP transmissions. The equilibrium bias point is loaded and the spectrum intensity for both polarizations is ramped up to its maximum. Then, the voltage sweep is performed in the selected range and response is collected. The EQE simulations consider a $1\ mW\ cm^{-2}$ monochromatic source filtered-out using WGP transmissions. The wavelength of the monochromatic source is ramped from $300\ nm$ to $800\ nm$ at the reverse bias point previously considered. The actual EQE is evaluated in a post-processing step, in which a `tcl` script is exploited to perform the calculation. In this context, simulation data are also exported to text file. The simulations results are shown in fig. 30.

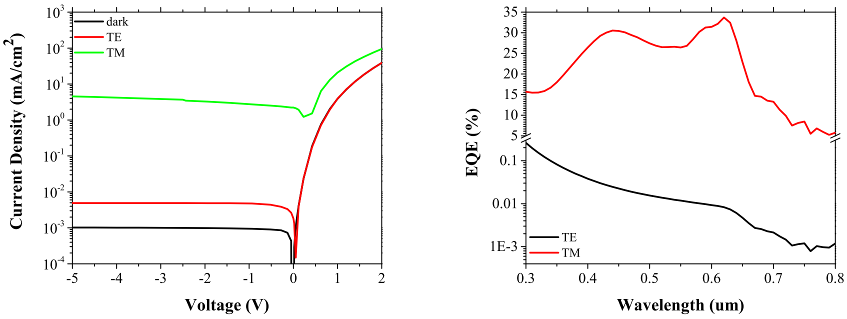

(a) **(b)**

Figure 30: *TCAD simulations of the POPD: a) currents, b) EQE.*

The dark currents and the photocurrents for TE and TM polarizations are shown in fig. 30a. The TM-to-TE photocurrent ratio is approximately of 10^3 for an anode voltage of $-5\ V$. The TM-to-TE EQE ratio is approximately of 10^3 at $600\ nm$. It is worth noting that the EQE for the TM case does not substantially differ from that of a simple OPD (section 4.3.2), indicating the WGP only little affects the efficiency of the device for the transparent polarization. Those performance are more then sufficient to employ the POPD for analytic applications.

5.3.2 Device Feedback

A proof-of-concept implementation of the POPD has been realized using a soft-lithography process for the WGP (Nagel et al. (2016)), with a subsequent spray-coating deposition of the organic layers (Abdellah et al. (2010)). Details about the experimental processes employed can be found in Falco (2016).

The measured POPD response is shown in fig. 31 along with the evaluation simulations performed in the previous section.

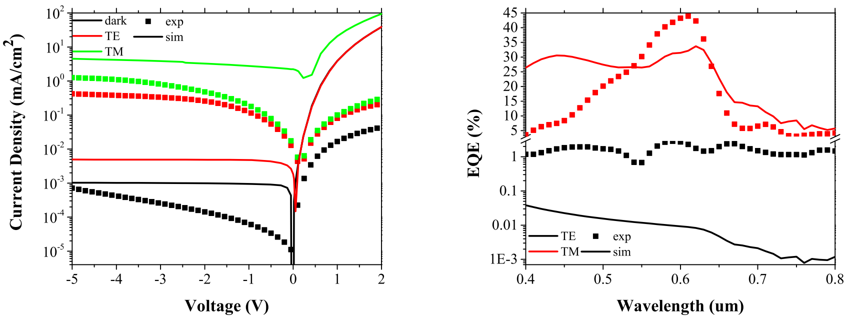

(a) **(b)**

Figure 31: *Comparison between experimental data and simulations: a) currents, b) EQE.*

As can be observed, performance are lower than predicted with TM-to-TE photocurrent and EQE ratios of approximately 10 and 50, respectively. This discrepancy in magnitude is mostly due to the fact the TE mode is not effectively reflected by the implemented WGP, as the TE photocurrent is two orders of magnitude lower than the simulated one and the EQE is in the 1% range while being between 10^{-1} and 10^{-3} in simulations.

The reason for that is to be sought in the structure of the implemented WGP. In fact, as pointed out by electron microscopy, it is observed the duty cycle between upper and lower metal grids is roughly 70% due to process conditions. Moreover, the Aluminum wires assume a rounded-shape against the square metal wires hypothesized before, as also pointed out by other reports (Ekinci et al. (2006)). Based on this evidence, more accurate outcomes can be obtained by refining the WGP structure in FDTD simulations. The results are shown in fig. 32. Here, both the simulations (solid line: original structure, dashed line: refined structure) and experimental data are reported (symbols).

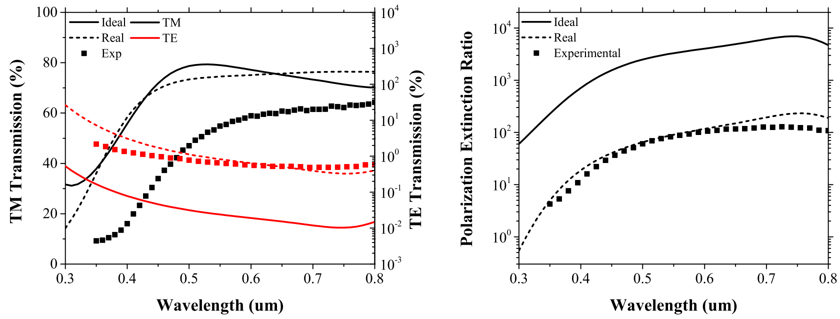

(a) **(b)**

Figure 32: *WGP FDTD simulations for a more realistic structure: a) transmissions, b) PER.*

Despite the fact transmission values for the TM mode still result roughly higher than the measured ones, the TE transmission reproduces the experimental data well. As a consequence, also the PER results fairly in accord with the measurements. This is in contrast with the initial transmission values, where the TE was much lower then the experimental one.

The POPD device simulations carried out using corrected transmission values to take into account the real structure of the WGP are reported in fig. 33.

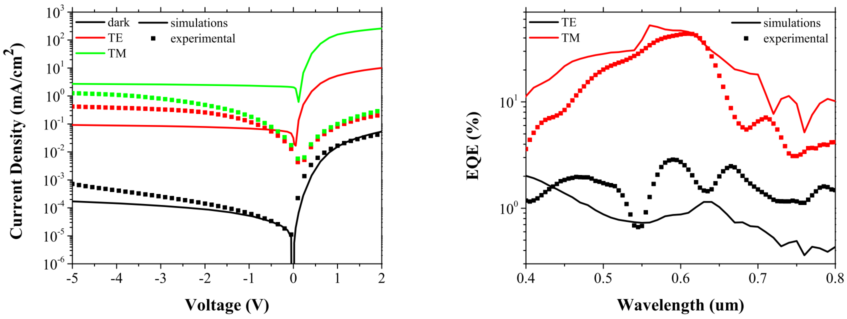

(a) **(b)**

Figure 33: *Refinement of POPD simulations using more accurate transmission value: a) currents, b) EQE.*

Electrical parameters have also been modified with respect to evaluation simulations in order to find the best resemblance with experimental curves. A

Gaussian DOS is considered in the form of a modified expression for N_C and N_V (see section 2.2.1), having N_{LUMO} (N_{HOMO}) equal to $1 \cdot 10^{20}$ $cm^{-3}eV^{-1}$, σ_n (σ_p) equal to 50 meV and E_{LUMO}-E_C (E_V-E_{HOMO}) equal to 0.1 eV. Hole mobility is lowered to 10^{-5} cm^2 V^{-1} s^{-1}. Fixed charge concentration N_{fix} at the interface between PEDOT:PSS and the P3HT:PC$_{61}$BM BHJ is also lowered to $3 \cdot 10^{11}$ C cm^{-2}. Interface trap distributions have been modified, having $N_{DOS}(E_\mu)$ equal to $4 \cdot 10^{14}$ $cm^{-3}eV^{-1}$ and x_n (x_p) equal to $1 \cdot 10^{-15}$ cm^2.

It can be noted how simulations better describe the experimental curves in this case. Nonetheless, some major discrepancies still occur. First of all, the reverse current in the dark shows a shunt leakage that is not picked up by simulations. Dongaonkar et al. (2010) have argued this shunt leakage is common in P3HT:PC$_{61}$BM-based OPV, associating its physical origin to percolation paths formed in the complex matrix of the BHJ and to molecular complexes or non-uniformities at interfacial layers. Hence, to take into account this effect, a more accurate modeling of the BHJ morphology is needed.

On the other hand, forward currents under illumination are still pretty far from the ones experimentally observed. This last issue can be mitigated introducing an Auger recombination rate with Γ_n (Γ_p) equal to 10^{-23} cm^6s^{-1}.

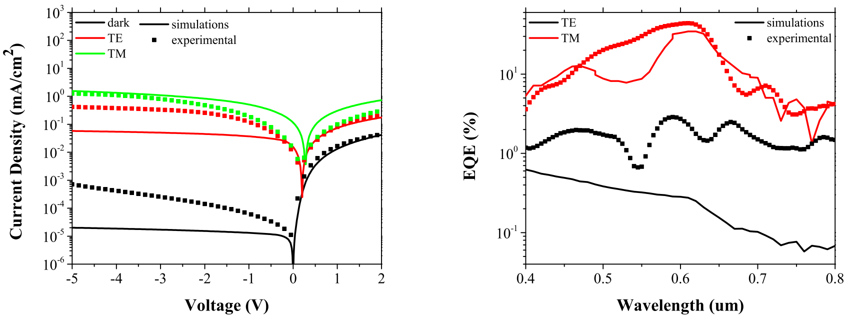

(a) **(b)**

Figure 34: *Refinement of POPD simulations using an Auger-like recombination rate: a) currents, b) EQE.*

The Auger recombination is a three carrier mechanism: an electron-hole couple is annihilated and the energy arising in the process is transferred to another electron which gets excited to the conduction band. Auger recombination rates have been observed in BHJ OPV devices (Deibel, Baumann and Dyakonov (2008); Juška et al. (2008)), although has been argued if this can be considered correct (Deibel and Dyakonov (2010); Street et al. (2010)).

The current understanding on the matter is that recombination rates with a cubic dependence upon the free charge carrier concentration are originated by a Langevin mechanism in which the recombination coefficient is not constant, but linearly dependent upon the concentration itself (Proctor et al. (2013)) [33]. However, it is worth noting how introducing an Auger-like recombination rate introduces further discrepancies on the TM mode EQE, in which a valley at approximately 550 *nm* is introduced.

5.4 Modeling the Bulk Heterojunction Morphology

As discussed in previous sections, tuning the VS parameters to obtain an accurate fit of the POPD experimental curves is a demanding task. In this regard, a more accurate description of phenomena occurring at the microscopic scale is needed. The first step toward this goal is taking into account the BHJ morphology.

5.4.1 Spin Exchange Algortihms

The BHJ morphology can be described using the Ising model – which was initially developed for the study of ferromagnetic materials (Ising (1925)). The Ising model considers a lattice having sites associated with positive (↑) or negative (↓) spin and allows for them to interact to exchange spin. As a consequence, the lattice can be evolved over time until an equilibrium is reached, based on thermodynamic considerations.

If the ↑ and ↓ spin values are used to represent the different phases in a BHJ, the Ising model can be applied to the study of this particular class of OSCs. The result of the evolution process is a net of intertwined connections that can be used to model experimentally-observed BHJ morphologies.

More in detail, the energy needed for a site i to swap spin with another site is given as in eq. (93), where J is the interaction energy.

$$\varepsilon_i = -J \sum_n (spin(i)spin(n) - 1) \tag{93}$$

Considering for simplicity only first-order nearest neighbors, the exchange

---

[33] The values of Γ_n and Γ_n employed for the photocurrent simulations are rather large and can be merely considered as fitting parameters. On the other hand – in the framework of a modified Langevin recombination – their dependence on carrier density could be investigated using phtocurrent measurement at different levels of optical power.

energy reduces to $\varepsilon_i = 2JN$ – in which N is the number of nearest neighbor having opposite spin from that of site i. Based on the exchange energy, an exchange probability can be defined as in eq. (94).

$$P_{ex} = \frac{\exp\left(-\frac{\Delta\varepsilon}{k_B T}\right)}{1+\exp\left(-\frac{\Delta\varepsilon}{k_B T}\right)} \tag{94}$$

Here, $\Delta\varepsilon$ is the energy difference between the swapped and original configuration states of the lattice [34]. Lattice evolution can be performed using spin-exchange algorithms, with two basic approaches available.

The first is a classical Monte Carlo (MC) process after Metropolis et al. (1953). A diagram showing a spin exchange algorithm for the Metropolis approach is reported in fig. 35a. For each iteration, a random number is generated and compared with the exchange probability of the swapped configuration. If the random number is smaller than the exchange probability, the swapped configuration is kept, otherwise it is discarded. Since not always a swapped configuration is kept and taken as a basis for a new iteration to run, the number of iterations will be higher than the number of times lattice evolution is progressed using this approach.

The second approach is an a-priori MC process after Bortz et al. (1975). A diagram showing a spin exchange algorithm for the Bortz approach is reported in fig. 35b. The lattice is characterized in term of classes for which the a-priori exchange probability can be calculated. Since the $[0:1]$ interval can be partitioned based on these a-priori probabilities, for each iteration a random number is generated and employed to select a class. Then, a random site can be chosen from the selected class population in order to be swapped with one of its first-order nearest neighbor. In this case, each iteration will produce a new lattice configuration.

The Bortz approach results usually faster than the Metropolis one. However, it demands a higher computational effort for large lattices since the class configuration burden grows in complexity. Nonetheless, the Bortz approach can be optimized in order to keep to a minimum class reconfiguration for each iteration by only updating sites affected by spin exchange.

Class characterization in the Bortz approach is performed in terms of the number of first-order nearest neighbor N. This characterization enables classes before and after a spin exchange to be coupled two-by-two, as shown in fig. 36 for example classes.

---

[34] $\Delta\varepsilon$ is negative if the swapped configuration is less stable than the original one, positive otherwise.

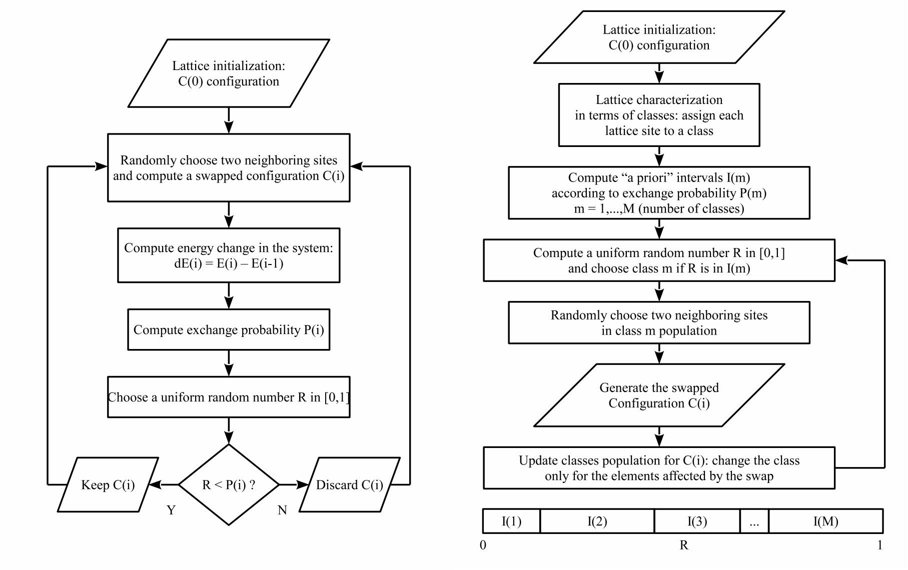

(a) **(b)**

Figure 35: *Spin exchange algorithms: a) Metropolis, b) Bortz.*

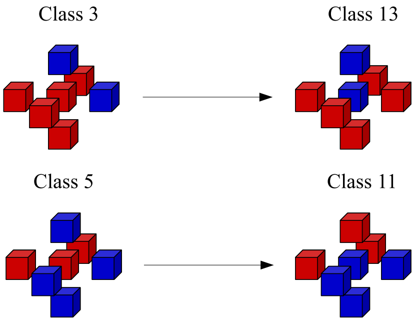

Figure 36: *Class coupling for a 3D lattice in the Bortz algorithm.*

The result of a swap for a site characterized by N=2 always results in a new configuration having N=5. In the same way, swapping a site characterized by N=4 always generates a site having N=3. Class coupling leads to the possibility of calculating $\Delta\varepsilon$ for each class in advance, which in turn results in the evaluation of a-priori probabilities.

Class characterization in the Bortz approach for a 3D lattice can be summarized as in tab. 18. Note that exchange probabilities are calculated for T

equal to 300 K. The very same approach can be considered for 2D lattices. Note that the interaction energy has been chosen equal to $J{=}k_BT/2$ in this case (Albes et al. (2014)).

Table 18: *Class characterization for a 3D lattice ($T=$ 300 K).*

Class	Spin	N	ε_i	Coupled Class	$\Delta\varepsilon/k_BT$	P_{ex}
1 (8)	↑ (↓)	0	0	1 (8)	0	0.5
2 (9)	↑ (↓)	1	$2J$	14 (7)	5	$6.7 \cdot 10^{-3}$
3 (10)	↑ (↓)	2	$4J$	13 (6)	3	$4.7 \cdot 10^{-3}$
4 (11)	↑ (↓)	3	$6J$	12 (5)	1	0.27
5 (12)	↑ (↓)	4	$8J$	11 (4)	-1	0.73
6 (13)	↑ (↓)	5	$10J$	10 (3)	-3	0.95
7 (14)	↑ (↓)	6	$12J$	9 (2)	-5	0.99

5.4.2 *Monte Carlo Simulations*

In this thesis, the Bortz approach has been considered to generate BHJ morphologies. The algorithm reported in fig. 35b has been implemented using MATLAB©. The implementation is based on the assumptions of periodic boundary conditions and only one exchange at a time. For this reason, it is not suitable to simulate lattices that are characterized by one dimension in which less then four sites are allocated. The MATLAB© implementation is here discussed using an `Octave` pseudo-code. The top level script of the program is reported in the following code snippet.

```
% Lattice initialization
if load_lattice == 1
  lattice = read_from_txt(filename);
else
  lattice = random('bino', 1, 0.5, lattice_size);
end
% Execute spin exchange algorithm
MCT = 0;
for i = 1:steps
  [lattice, class_population] = ising_lattice_bortz(lattice, dMCT);
  MCT = MCT + i*dMCT;
  write_to_txt(lattice, class_population);
end
% Plot lattice
fig = plot_lattice(lattice);
% Generate scheme file
generate_scheme_file(lattice);
```

The script provides the possibility of either loading a previously generated lattice from file or generating a new one as a starting point of the spin exchange algorithm. When the lattice is generated from scratches, a binomial distribution in which ones (representing ↑ spin) and zeros (representing ↓ spin) have equal probability weights is employed. The core of the spin exchange algorithm is contained in the `ising_lattice_bortz` function. This function takes as inputs the lattice and the number of MC iterations to be performed and returns as output the swapped lattice and the classes population. The `ising_lattice_bortz` function is inserted into a `for` loop to give the possibility of breaking the process in various steps in order to perform sampling and saving intermediate lattices. The latter operation is performed using the `write_to_txt` function, which save to text files the content of the lattice and statistics about classes population plus other quantities. The `lattice_plot` function is used to plot the lattice and save the figure to file. The last operation is the generation of a `Scheme` file for the batch drawing of the lattice structure into the Sentaurus$^{©}$structure editor, which is employed to simulate in TCAD the characteristics of the BHJ. This is performed by the `generate_scheme_file` function. The pseudo-code implementation of the `ising_lattice_bortz` function is reported below.

```
function [lattice, class_population] = ising_lattice_bortz(lattice, MCT)
  % Initial class characterization
  [class_population, elements, neighbors] = class_detection(lattice);
  for iteration = 1:MCT
    % Calculate intervals based on a-priori probabilities
    P = exchange_probability(dE, T);
    % Sample a class
    class = datasample(find(class_population), 1, 'Weights', P);
    % Sample a site in the selected class
    R1 = randi([1 class_population(class)]);
    selected_site = elements{class}(R1);
    % Sample a neighbor
    if lattice(selected_site) == 1
      N = class-1;
    else
      N = class-8;
    end
    R2 = randi([1,N]);
    selected_neighbor = neighbors{selected_site}(R2);
    % Save a previous version of the lattice and swap
    lattice_prev = lattice;
    selected_site_temp = lattice(selected_site);
    lattice(selected_site) = lattice(selected_neighbor);
    lattice(selected_neighbor) = selected_site_temp;
    % Create the subsytem of lattice to be updated
    sub_sys = subsystem(selected_site, selected_neighbor, lattice);
    % Update classes after swap
    [class_population, elements, neighbors] =
      class_update(lattice, lattice_prev, sub_sys, class_population, neighbor,
                   elements);
  end
end
```

The `class_detection` function is used to first characterize the lattice in terms of classes. This function takes the lattice as an input and outputs the class population, the elements belonging to each class and the first-order nearest neighbor for each element of the lattice. After this operation, MC iterations are performed. The exchange probability is calculated using the `exchange_probability` function, which is based on eq. (94). This probability is used to weight the `datasample` function in order to select the class that will be subjected to the spin exchange. Consequently, two random numbers are generated. The first number is used to select a lattice site inside the class population. The second chooses a neighbor of the selected lattice site. The lattice site and its neighbor are finally swapped generating a new lattice configuration. The previous lattice configuration (i.e. `lattice_prev`) is retained in order to update classes for the new configuration. This is performed by the `class_update` function. This function also need a subsystem of the new lattice configuration, in which only the lattice site affected by the spin exchange are contained. This is determined by the `subsystem` function. The following snippet contains the code for the `class_detection` function.

```
function [class_population, elements, neighbors] = class_detection(lattice)
  for lattice_site = 1:size(lattice)
    % Count 1st order nearest neighbors
    [N, neighbors{lattice_site}] = count_opposite_nn(lattice, lattice_site, 1);
    % Compute site class
    if lattice(lattice_site) == 1
      class = N+1;
    else
      class = N+8;
    end
    % Update class population and elements
    class_population(class) = class_population(class) + 1;
    elements{class}(class_population(class)) = lattice_site;
  end
end
```

Each lattice site is scanned and the first-order nearest neighbors are counted and identified using the `count_opposite_nn` function. This function takes as inputs the lattice itself, the site being analyzed and the order, while it returns N and the neighbors coordinate for the particular site received as an input. Note that in the considered case `nn_order` is simply equal to 1. Based on the value of N the class of each site is detected, the class population and elements being updated while the detection goes by. The content of the `count_opposite_nn` function is shown below.

```
function [N, neighbors] = count_opposite_nn(lattice, lattice_site, nn_order)
  % Retrieve lattice_site xyz coordinates
  x = lattice_site(1);
  y = lattice_site(2);
  z = lattice_site(3);
  % Initialize the number of nearest neighbor with opposite spin
  N = 0;
```

```
  % Scan 1st dimension
  for i = x-nn_order:x+nn_order
    % Apply periodic boundary conditions
    i_periodic = periodic_boundary(i, lattice_size_along_x);
    % Nearest neighbor spin evaluation
    if lattice(i_periodic) ~= lattice(x)
      N = N+1;
      neighbors(N) = [i_periodic,y,z];
    end
  end
  % Scan 2nd dimension
  ...
  % Scan 3rd dimension
  ...
end
```

The coordinates of the input site along x, y and z dimensions are retrieved and – based on the nearest neighbor order `nn_order` – each dimension is scanned counting for opposite-spin neighbors. Note that periodic boundary conditions are applied (i.e. the `periodic_boundary` function) to account for the possibility `lattice_site` is belonging to the most external shell of the lattice. Lastly, the `class_update` pseudo-code is reported below.

```
function [class_population_up,elements_up,neighbors_up] =
  class_update(lattice, lattice_prev, class_population, neighbor, elements)
  % Initialize quantities to update
  class_population_up = class_population;
  elements_up = elements;
  for sub_sys_site = 1:size(sub_sys)
    % Compute class before swap
    [N, ~] = count_opposite_nn(lattice_prev, sub_sys_site, 1);
    if lattice_prev(sub_sys_site) == 1
      class = N + 1;
    else
      class = N + 8;
    end
    % Neighbors update and compute class after swap
    [N_up, neighbors_up] = count_opposite_nn(lattice, sub_sys_site, 1);
    if lattice(sub_sys_site) == 1
      class_up = N_up + 1;
    else
      class_up = N_up + 8;
    end
    % Class population update
    class_population_up(class) = class_population_up(class) - 1;
    class_population_up(class_up) = class_population_up(class_up) + 1;
    % Elements update
    [~, row] = ismember(elements_up{class}, sub_sys_site, 'rows');
    index = find(row, 1);
    elements_up{class}(index)=[];
    elements_up{class_up} = [elements_up{class_up};sub_sys_site];
  end
end
```

For each site belonging to the input subsystem, the classes before and after the spin exchange are retrieved, contextually updating the neighbors population using the `count_opposite_nn` function. Consequently, classes are managed. For what concern the class prior to spin exchange, population is decreased by 1 and the site is removed from its elements. For what concern the class after spin exchange, population is increased by 1 and the site is added to its elements. The morphologies generated with the above MATLAB© implementation have been characterized in terms of an average grain size d_{av} as expressed in eq. (95).

$$d_{av} = \frac{3V_{BHJ}}{A_{BHJ}} = \frac{3N_{TOT}\,l_{BHJ}^{3}}{A_{BHJ}} \tag{95}$$

Here, V_{BHJ} is the volume of the BHJ – which is equal to the total number of lattice site N_{TOT} multiplied the cube of the lattice constant l_{BHJ} – and A_{BHJ} is the interfacial area between the phases of the BHJ. This relation is readily transferred to 2D morphologies.

The evolution of the average grain size d_{av} for 3D lattices of different sizes is shown in fig. 37a, while the classes population for a 3D lattice of forty sites per side is shown in fig. 37b.

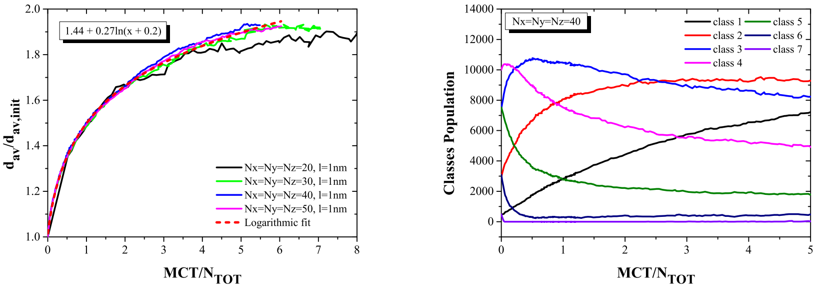

(a) **(b)**

Figure 37: *Lattice evolution MC simulations: a) average grain size, b) classes population.*

It can be observed that the average grain size follows a logarithmic growth, which saturates when the number of MC trials reach approximately 6 N_{TOT}. In this regime, the average grain size is almost doubled with respect to its initial value and the lattice can be said to be close its equilibrium point. The trend followed by the classes population is pretty informative from this point of view. It can be observed that very unstable classes like class 5, 6 or 7 decay in population quite a lot in the early stages of execution. This decay in turn favors the population of stable classes, like class 1, 2 or 3.

It is worth noting that is not the most stable class – class 1 – to get the greater population as the number of MC trials increases. Instead, class 2 and

3 are the most populated since they are characterized by a much lower exchange probability then all the others. This leads the algorithms to damp the d_{av} increase after the population of instable classes is brought down – hence explained the logarithmic growth of the average grain size. It is advised that d_{av} can be growth beyond this limit by changing the expression of the exchange probability or even artificially tailoring the P_{ex} for each class. This however, would only have a fictional meaning since exchange probabilities are no longer physically-based [35].

Examples of generated BHJ morphologies are depicted in fig. 38. Both 2D and 3D lattices before (fig. 38a and fig. 38c) and after (fig. 38b and fig. 38d) the spin exchange algorithm execution are shown. The 2D lattices consist of 100 sites per side, while the 3D lattices consist of 50 sites per side.

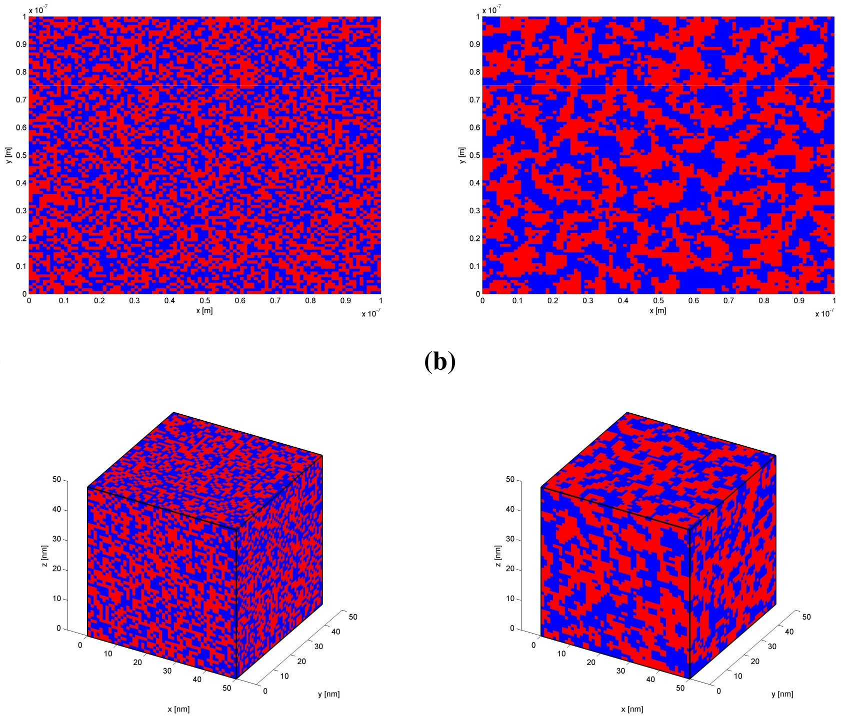

(a) **(b)**

(c) **(d)**

Figure 38: *Generated morphologies: a 2D lattice a) before and b) after the evolution; a 3D lattice a) before and b) after the evolution.*

---

[35] The limited growth of d_{av} it is not an algorithmic flaw but it can just be considered as a physical limit to the aggregation of phases at the given temperature.

The aggregation of the two phases is evident, originating intertwined connections that closely resemble the morphology of a real BHJ. It is worth noting how the generated morphologies are parametric, since the lattice constant l_{BHJ} can be opportunely chosen to vary the extension of the domain.

5.4.3 *TCAD Simulations*

The generated morphologies can be inserted into a TCAD environment to simulate BHJ electrical characteristics. Accordingly with the POPD analysis presented in the first part of this chapter, P3HT and $PC_{61}BM$ are taken as hole and electron transporting phases of the BHJ, respectively. Schottky boundary conditions are considered, with Gold on one side on the BHJ (anode) and Calcium on the other (cathode). The material parameters employed are those described in section 2.6, which have been added to the Sentaurus$^{©}$database without any further modification. An hole (electron) mobility μ_p (μ_n) equal to 10^{-3} cm^2 V^{-1} s^{-1} is considered for P3HT ($PC_{61}BM$). No trap distributions have been added to the OSCs models. The qualitative results of current-voltage simulations under dark conditions are shown in fig. 39.

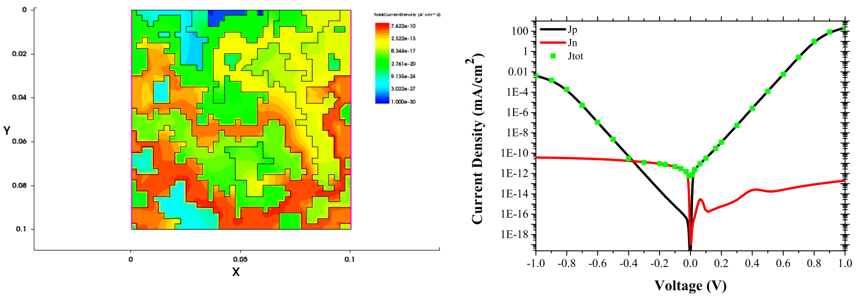

(a)

(b)

Figure 39: *TCAD simulations of BHJ morphologies: a) 2D current density distribution (V=-1 V), b) J-V characteristics.*

From the 2D plot of fig. 39a it can be observed how the current density is mostly determined by the percolation path between electrodes. In the case shown, this path resides on the hole transporting phase, i.e. the P3HT. This consideration is especially true when the electric fields are high, e.g. $|1|$ V over a 100 nm domain, as can be observed in fig. 39b. Here, the hole, electron and total currents are shown. The only voltage range in which the electron current dominates over the hole one is for low electric fields, i.e. $[-0.4,\ 0]\ V$ over a 100 *nm* domain. It is worth noting how the current density for negative voltages is characterized by a slope that resembles the one observed in the reverse current of the POPD. As pointed out before, Dongaonkar et al. (2010) associated shunt leakage in P3HT:PC$_{61}$BM-based OPV devices to complex structures formed by the BHJ morphologies. It is evident that microscopic features of the OSC cannot be ignored in the task of accurately modeling a POPD, as well as BHJ devices in general. Morphology generation algorithms – as the one employed in this chapter – could be used in MC simulation engines or inserted into a TCAD environment. Results could be directly accessible to existing higher-level models or used to create new ones. A successful and feasible integration of microscopic-scale models into higher-level simulation methods has not yet been assessed for organic electronics. The debate on how to reach this goal is still vivid among experts and it will likely animate the scientific community in years to come, leading to new, exciting findings and achievements.

5.5 Conclusion

This chapter have dealt with the application of numerical simulations to the implementation of a novel Organic Photodiode (OPD) device in which the photocurrent is sensible to incident light polarization. This concept demonstrates the potentiality of organic electronics, in which modular designs can be realized exploiting native compatibilities of processes and materials in order to create room for new applications. In particular, the anode metal of a conventional P3HT:PC$_{61}$BM OPD has been patterned using soft-lithographic techniques in order to function as both Wire Grid Polarizer (WGP) and electrode.

This innovative device – which has been denominated Polarized Organic Photodiode (POPD) – has been implemented using a first evaluation step based on numerical simulation, in order to realize an application-performant OPD with less waste of resources and experimental effort. The WGP and the OPD have been simulated to show performance are, in principle, largely sufficient for Lab-on-a-Chip applications.

However, a proof-of-concept implementation of the POPD based on the above results has been found to posses a TE mode shielding capacitance lower then expected. While this is has still been considered enough for analytic purposes, the origins of this behavior have been investigated. The low reflection of the TE mode has been imputed to the WGP structure, which results different from the ideal one employed in simulations. As a result, a second step has been introduced in which feedback from the experimental data have been taken in order to refine structures and models employed in the simulation to better resemble the measured curves.

It has been found that the forward current under illumination conditions can be reproduced by introducing an Auger-like recombination rate. On the other hand, the shunt leakage paths present in the reverse current cannot be taken into account using continuum simulations. One of the reasons is the application of a Virtual Semiconductor approach to describe the features of the Bulk Heterojunction semiconductor.

As an alternative, an approach based on the description of the Bulk Heterojunction morphology using spin exchange algorithms has been proposed to overcome the latter point. A priori-probability are used in the applied spin exchange model in order to speed up the process of generating realistic morphologies through Monte Carlo iterations. Current-voltage analysis carried out using a generated Bulk Heterojunction morphology show – at least qualitatively – that a shunt leakage current can be reproduced in reverse bias and associated to percolation paths arising in the complex blend connections, as initially proposed by Dongaonkar et al. (2010).

Conclusion And Outlook

The organic electronics field has grown particularly in recent years, culminating with the exploitation of organic devices in flexible displays and lighting panels which are today commercially available. As organic electronics further expands, new scenarios are envisioned. The focus is rapidly shifting from the study of basic material properties to the exploitation of complex system architectures as new device concepts are introduced. For instance, the request of organic photodetectors is growing. Those devices rely on the exploitation of Bulk Heterojunction (BHJ) materials, whose properties in devices like Organic Phototransistor (OPT) are to be assessed. Besides the conventional planar architectures, an OPT can be realized as a Vertical Organic Transistor (VOT), as the horizontal dimension is unencumbered by electrical performance-related constraints and can be used to achieve a sufficiently large photosensitive area. VOTs can also be applied to organic power electronics, since they can overcome the limitations of conventional transistors in terms of channel length and structuring techniques in order to achieve substantial current densities. Organic electronics is also growing due to the fact materials are in most cases biocompatible and devices can be exploited directly in conjunction with biological systems.

The process of device analysis, design and implementation cannot be ported outside an academic environment without the aid of computer-based tools to perform those tasks with. In addition, numerical simulations need to be accurate and fast, not having to waste unnecessary computing resources in order to guarantee an adequate product time-to-market to be competitive. At this purpose, Technology Computer Aided Design (TCAD) tools can be exploited. Following this considerations, the aim of this dissertation has been to demonstrate that existing commercial TCAD tools can be conveniently applied and modified for the study and realization of novel organic electronic devices, paving the way to development of new applications in the multifaceted shades of organic electronics.

In Chapter 3, we studied the transport properties of an archetypal BHJ through Organic Field-Effect Transistor (OFET) simulations. The first part of this study concerned current-voltage characteristics in the steady state. The results show that a transverse electric field-dependent mobility should be accounted for in order to correctly describe the experimental curves. In addition, electronic traps are shown to greatly influence the device behavior and should be considered to correctly describe the subthreshold current regime. The OFETs have been further investigated using admittance spectroscopy techniques. The analysis shown the presence of bias-dependent peaks in the loss-frequency diagram, which are attributed to the response of charge in the transistor channel. Using this interpretation, the vertical diffusivity for holes was calculated.

In Chapter 4, having this knowledge in mind, we proposed a modeling study to compare a planar OFET to a vertical Organic Static Induction Transistor (OSIT). Both devices have been considered for OPT applications, being BHJ-based, where the OFET was taken as reference to analyze strong and weak spots of the OSIT architecture. We shown that both planar and vertical OPTs are characterized by similar electrical performance under dark, in terms of threshold voltage and field-effect mobility. On the other hand, the vertical OPT outperforms the planar one under illumination conditions, with an average increase in efficiency of 10% over the visible spectrum. The reason for that is to be sought in the different device structures, being the vertical one more prone to collect photo-generated carriers. For the planar OPT, only carriers generated inside the channel region can be collected by the drain-source electric field, while for the vertical OPT this electric field is applied to most of the carriers since the device is entirely stacked between electrodes. Performance can be further improved by changing the gate metal grid of the OSIT to take on a staggered architecture, where adjacent gate wires are placed on different vertical planes and partially superimposed. With this structure it is possible to improve both the on-off ratio and efficiency, with the latter above the quantum-yield of the material due to photoconduction gain mechanisms.

In Chapter 5, we have applied numerical simulations to the implementation of a novel device, the Polarized Organic Photodiode (POPD), which is a conventional BHJ photodiode with the innovative feature of having a monolithically integrated Wire Grid Polarizer (WGP) functioning as anode. As a result, the photocurrent of the POPD is dependent on the light polarization as well as intensity. This device can be applied to cross-polarization schemes in order to achieve high signal-to-noise ratios in lab-on-a-chip applications for fluorescence studies of antigen/antibody biological systems. Using the POPD-approach it should be indeed possible to directly integrate detector and light source on the microfluidic chip in a way to overcome current state-of-the-art limitations, as nowadays devices are mechanically attached to the former in a cumbersome and ineffective process. Computer-based tools have been employed to solve both Maxwell's and semiconductor equations prior to device realization. This allowed to assess the POPD performance being largely sufficient for analytical applications. The experimental evaluation of the polarized photodiode as based on simulations shown slightly lower performance, since the real polarizer structure is not equal to the simulated one. Refinement of the optical and electrical models obtained as based on the experimental observations are indeed capable of more realistic description of device behavior. However, it is evident how correctly tuning all the simulation parameters to fit the experimental curves is a demanding task. A good accord with the experimental data is not possible unless taking into account microscopic properties related to the BHJ morphology. In this regard, we have simulated BHJ morphologies using spin-exchange algorithms based on the Ising model. In this model, the BHJ is represented as a lattice in which each site is associated with a spin value representing one of the two blended phases. The lattice can be evolved over time based on an exchange probability. Simulations are based on a Monte Carlo (MC) approach, resulting in a realistic morphology generation. These morphologies can be inserted into a TCAD to simulate the current under dark conditions. The results were qualitatively in accord with the dark current experimentally measured in the POPD, as a non-ohmic slope is observed for negative voltages that can be attributed to the presence of percolation paths inside the material.

In conclusion, this work describes a complete framework in which TCAD tools are applied to device analysis (Chapter 3), design (Chapter 4) and implementation (Chapter 5). These approaches are based at a deep physical level and allow to highlight the important parameters influencing device behavior, with an analysis aimed to a reduction of the experimental effort following a methodological and/or design-through-experiment process. All the simulations reported are based on the commercial software Sentaurus©, a state-of-the-art Technology Computer Aided Design (TCAD) by world-leading Electronic Design Automation (EDA) company Synopsys©. The models contained in the simulator have been modified and extended where necessary to describe organic devices. With this, we have contributed to demonstrate the applicability of these tools to organic electronics is ready to be exploited on the next level of abstraction, i.e. taken from the academic to the industrial world. Nevertheless, we noticed that in particular cases the TCAD framework fails to describe phenomena related to the organic material. This can be overcome shifting the subject to a multiscale approach, integrating in the simulator methods for the resolution of microscopic features that are important in BHJ devices. We strongly believe numerical simulations would greatly contribute to a broader diffusion of organic electronic devices in real-world applications and it is our opinion this approach will set the basis for a better understanding and design of organic electronic devices in the near future.

Appendix A
Material Parameters

The material parameters used in numerical simulations throughout this thesis are taken from the literature. Those are reported in the following. For each material, the parameters are reported in tabular fashion along with values, units and measurement method (where available). References are listed in the text.

The parameters of PEDOT:PSS are reported in tab. 19. The energy gap is taken from Zade and Bendikov (2006), the complex refractive index is taken from Pettersson et al. (2002), the electrical conductivity is taken from Crispin et al. (2006); Huang et al. (2005); Jönsson et al. (2003); Kim et al. (2011), the work function is taken from Brown et al. (1999); Crispin et al. (2006); Greczynski et al. (2001).

Table 19: *PEDOT:PSS characterization in the literature.*

PEDOT:PSS			
Parameter	*Values*	*Unit*	*Methods*
E_G	$1.68 - 1.80$	eV	DFT
n_c	graphical	1	–
σ	$0.005 - 1400$	$S\ cm^{-1}$	4PP
Φ	$4.7 - 5.4$	eV	KP, PS

The parameters of P3HT are reported in tab. 20. The energy gap is taken from and the HOMO energy level are taken from Tsoi et al. (2011), the complex refractive index is taken from Hoppe and Sariciftci (2004), the hole mobility is taken from Deibel, Wagenpfahl and Dyakonov (2008); Klauk (2010); Koster et al. (2006), the relative dielectric constant is taken from Juška et al. (2003), the photogeneration quantum yield is taken from Piris et al. (2009).

The parameters of $PC_{61}BM$ are reported in tab. 21. The energy gap is

Table 20: *P3HT characterization in the literature.*

P3HT			
Parameter	*Values*	*Unit*	*Methods*
E_G	$1.9 - 2.2$	eV	Optical
E_{HOMO}	$4.6 - 4.9$	eV	PS
n_c	graphical	1	–
μ_p	$1.1 \cdot 10^{-6} - 1.0 \cdot 10^{-3}$	$cm^2\ V^{-1}\ s^{-1}$	IV, OFET
ε_r	3.0	1	IV
γ	0.15	1	–

taken from Tsoi et al. (2011), the LUMO energy level is taken from Larson et al. (2013), the complex refractive index is taken from Hoppe and Sariciftci (2004), the electron mobility is taken from Deibel, Wagenpfahl and Dyakonov (2008); Koster et al. (2006, 2005), the relative dielectric constant is taken from Blom et al. (2007).

Table 21: *$PC_{61}BM$ characterization in the literature.*

$PC_{61}BM$			
Parameter	*Values*	*Unit*	*Methods*
E_G	1.8	eV	Optical
E_{LUMO}	$3.66 - 3.88$	eV	PS
n_c	graphical	1	–
μ_n	$2.5 \cdot 10^{-5} - 0.25$	$cm^2\ V^{-1}\ s^{-1}$	IV, OFET
ε_r	3.9	1	

The parameters of P3HT:PC_{61}BM are reported in tab. 22. The complex refractive index is taken from Dennler et al. (2007); Lee et al. (2010), the photogeneration quantum yield is taken from Piris et al. (2009).

The parameters of ITO are reported in tab. 23. The energy gap, the electrical resistivity, the free electron concentration and the mobility are taken from Kim et al. (1999). The complex refractive index is taken from Synowicki (1998), the work function is taken from Brown et al. (1999); Park et al. (1996); Sugiyama et al. (2000).

Table 22: *P3HT:PC_{61}BM characterization in the literature.*

P3HT:$PC_{61}BM$			
Parameter	*Values*	*Unit*	*Methods*
n_c	graphical	1	RTA, Ellipsometry
γ	0.5	1	–

Table 23: *ITO characterization in the literature.*

ITO			
Parameter	*Values*	*Unit*	*Methods*
E_G	$3.76-4.20$	eV	Optical
n_c	graphical	1	Ellipsometry
Φ	$4.3-5.2$	eV	PS
ρ	$2-5\cdot10^{-4}$	$\Omega\ cm$	4PP
n	$1.63-7.10\cdot10^{20}$	cm^{-3}	VDPM
μ_n	$28-41$	$cm^2\ V^{-1}\ s^{-1}$	VDPM

The parameters of Al_2O_3 are reported in tab. 24. The energy gap is taken from Jimenez-Gonzalez and Schmeisser (1991), the complex refractive index is taken from French et al. (1998). The relative dielectric constant and the electrical resistivity are taken from Voigt and Sokolowski (2004).

Table 24: *Al_2O_3 characterization in the literature.*

Al_2O_3			
Parameter	*Values*	*Unit*	*Methods*
E_G	9.9	eV	Spectroscopy
n_c	graphical	1	EELS
ε_r	$7-10$	1	Impedance
ρ	$2.5\cdot10^{11}$	$\Omega\ cm$	Leakage Current

For Calcium, the complex refractive index n_c is taken from Nilsson and Forssell (1977), where it is reported in graphical form as estimated by RTA.

Appendix B
Names Of Chemical Compounds

The IUPAC names of materials and compounds mentioned in this thesis are reported below with relative abbreviations or common names.

Acetone	Propan-2-one
Ag	Silver
Al	Aluminum
Al_2O_3	Aluminum Oxide
Alq_3	Tris(8-hydroxyquinolinato)aluminium
Au	Gold
C	Carbon
Ca	Calcium
C_{60}	Buckminsterfullerene
CNT	Carbon Nanotubes
CuPc	Copper Phthalocyanine
Ethylene	Ethene
FIrpic	Bis[(4,6-di-fluorophenyl)-pyridinate-N,C2?]picolinate
ITO	Indium Tin Oxide
Ir	Iridium
$Ir(MDQ)_2$	Iridium(III)bis(2-methyldibenzo[f,h]quinoxaline)(acetylacetonate)

Ir(ppy)$_3$	Fac-tris(2-phenylpyridinato)Iridium(III)
Isopropanol	Propan-2-ol
LiF	Lithium Fluoride
MEH-PPV	poly[2-methoxy, 5-(2’-ethyl-hexyloxy)-1,4-phenylene vinylene]
oDCB	ortho-Dichlorobenzene
P3HT	Poly(3-hexylthiophene-2,5-diyl)
PC$_{61}$BM	[6,6]-Phenyl C$_{61}$ butyric acid methyl ester
PEDOT:PSS	Poly(3,4-ethylenedioxythiophene)-poly(styrenesulfonate)
Pentacene	Pentacene
PPV	Poly(paraphenylene vinylene)
Si	Silicon
SiC	Silicon Carbide
SiO$_2$	Silicon Oxide

Bibliography

Abdellah, A., Fabel, B., Lugli, P. and Scarpa, G. (2010), ‘Spray deposition of organic semiconducting thin-films: Towards the fabrication of arbitrary shaped organic electronic devices’, *Organic Electronics* **11**(6), 1031–1038.

Albes, T., Lugli, P. and Gagliardi, A. (2016), ‘Investigation of the blend morphology in bulk-heterojunction organic solar cells’, *IEEE Transactions on Nanotechnology* **15**(2), 281–288.

Albes, T., Popescu, B., Popescu, D., Loch, M., Arca, F. and Lugli, P. (2014), Kinetic monte carlo modeling of low-bandgap polymer solar cells, *in* ‘Photovoltaic Specialist Conference (PVSC), 2014 IEEE 40th’, IEEE, pp. 0057–0062.

Ambegaokar, V., Halperin, B. and Langer, J. (1971), ‘Hopping conductivity in disordered systems’, *Physical review B* **4**(8), 2612.

Apanovich, Y., Blakey, P., Cottle, R., Lyumkis, E., Polsky, B., Shur, A. and Tcherniaev, A. (1995), ‘Numerical simulation of submicrometer devices including coupled nonlocal transport and nonisothermal effects’, *IEEE Transactions on Electron Devices* **42**(5), 890–898.

Atkins, P. W. and Friedman, R. S. (2011), *Molecular quantum mechanics*, Oxford university press.

Auf der Maur, M., Penazzi, G., Romano, G., Sacconi, F., Pecchia, A. and Di Carlo, A. (2011), ‘The multiscale paradigm in electronic device simulation’, *IEEE Transactions on electron devices* **58**(5), 1425–1432.

Auger, P. (1925), ‘Sur les rayons secondaires produits dans un gaz par des rayons xcr acad. sc., 1925, 180, 65. auger p. et perrin f’, *Considérations* *théoriques sur les directions démission des photoélectrons. C. R. Acad. Sc* **180**, 1742.

Aurenhammer, F. (1991), 'Voronoi diagrams - a survey of a fundamental geometric data structure', *ACM Computing Surveys (CSUR)* **23**(3), 345–405.

Baeg, K.-J., Binda, M., Natali, D., Caironi, M. and Noh, Y.-Y. (2013), 'Organic light detectors: photodiodes and phototransistors', *Advanced Materials* **25**(31), 4267–4295.

Banerjee, A., Pais, A., Papautsky, I. and Klotzkin, D. (2008), 'A polarization isolation method for high-sensitivity, low-cost on-chip fluorescence detection for microfluidic lab-on-a-chip', *IEEE Sensors Journal* **8**(5), 621–627.

Bank, R. E., Rose, D. J. and Fichtner, W. (1983), 'Numerical methods for semiconductor device simulation', *SIAM Journal on Scientific and Statistical Computing* **4**(3), 416–435.

Bardeen, J. and Brattain, W. H. (1948), 'The transistor, a semi-conductor triode', *Physical Review* **74**(2), 230.

Bässler, H. (1993), 'Charge transport in disordered organic photoconductors a monte carlo simulation study', *physica status solidi (b)* **175**(1), 15–56.

Ben-Sasson, A. J., Ankonina, G., Greenman, M., Grimes, M. T. and Tessler, N. (2013), 'Low-temperature molecular vapor deposition of ultrathin metal oxide dielectric for low-voltage vertical organic field effect transistors', *ACS applied materials & interfaces* **5**(7), 2462–2468.

Ben-Sasson, A. J., Avnon, E., Ploshnik, E., Globerman, O., Shenhar, R., Frey, G. L. and Tessler, N. (2009), 'Patterned electrode vertical field effect transistor fabricated using block copolymer nanotemplates', *Applied Physics Letters* **95**(21), 213301.

Ben-Sasson, A. J., Chen, Z., Facchetti, A. and Tessler, N. (2012), 'Solution-processed ambipolar vertical organic field effect transistor', *Applied Physics Letters* **100**(26), 263306.

Ben-Sasson, A. J., Greenman, M., Roichman, Y. and Tessler, N. (2014), 'The mechanism of operation of lateral and vertical organic field effect transistors', *Israel Journal of Chemistry* **54**(5-6), 568–585.

Ben-Sasson, A. J. and Tessler, N. (2011), 'Patterned electrode vertical field effect transistor: Theory and experiment', *Journal of Applied Physics* **110**(4), 044501.

Ben-Sasson, A. J. and Tessler, N. (2012), 'Unraveling the physics of vertical organic field effect transistors through nanoscale engineering of a self-assembled transparent electrode', *Nano letters* **12**(9), 4729–4733.

Blakesley, J. C. and Greenham, N. C. (2009), 'Charge transfer at polymer-electrode interfaces: The effect of energetic disorder and thermal injection on band bending and open-circuit voltage', *Journal of Applied Physics* **106**(3), 034507.

Blom, P. W., Mihailetchi, V. D., Koster, L. J. A. and Markov, D. E. (2007), 'Device physics of polymer: fullerene bulk heterojunction solar cells', *Advanced Materials* **19**(12), 1551–1566.

Bolognesi, A., Berliocchi, M., Manenti, M., Di Carlo, A., Lugli, P., Lmimouni, K. and Dufour, C. (2004), 'Effects of grain boundaries, field-dependent mobility, and interface trap states on the electrical characteristics of pentacene tft', *IEEE Transactions on electron devices* **51**(12), 1997–2003.

Bolognesi, A., Di Carlo, A., Lugli, P. and Conte, G. (2003), 'Large drift-diffusion and monte carlo modeling of organic semiconductor devices', *Synthetic metals* **138**(1), 95–100.

Bortz, A. B., Kalos, M. H. and Lebowitz, J. L. (1975), 'A new algorithm for monte carlo simulation of ising spin systems', *Journal of Computational Physics* **17**(1), 10–18.

Bouhassoune, M., Van Mensfoort, S., Bobbert, P. and Coehoorn, R. (2009), 'Carrier-density and field-dependent charge-carrier mobility in organic semiconductors with correlated gaussian disorder', *Organic Electronics* **10**(3), 437–445.

Brady, M. A., Su, G. M. and Chabinyc, M. L. (2011), 'Recent progress in the morphology of bulk heterojunction photovoltaics', *Soft Matter* **7**(23), 11065–11077.

Braun, C. L. (1984), 'Electric field assisted dissociation of charge transfer states as a mechanism of photocarrier production', *The Journal of chemical physics* **80**(9), 4157–4161.

Brown, T., Kim, J., Friend, R., Cacialli, F., Daik, R. and Feast, W. (1999), ‘Built-in field electroabsorption spectroscopy of polymer light-emitting diodes incorporating a doped poly (3, 4-ethylene dioxythiophene) hole injection layer’, *Applied Physics Letters* **75**(12), 1679–1681.

Burroughes, J., Bradley, D., Brown, A., Marks, R., Mackay, K., Friend, R., Burns, P. and Holmes, A. (1990), ‘Light-emitting diodes based on conjugated polymers’, *nature* **347**(6293), 539–541.

Casalegno, M., Raos, G. and Po, R. (2010), ‘Methodological assessment of kinetic monte carlo simulations of organic photovoltaic devices: The treatment of electrostatic interactions’, *The Journal of chemical physics* **132**(9), 094705.

Caserta, G., Rispoli, B. and Serra, A. (1969), ‘Space-charge-limited current and band structure in amorphous organic films’, *physica status solidi (b)* **35**(1), 237–248.

Castro-Carranza, A., Nolasco, J., Estrada, M., Gwoziecki, R., Benwadih, M., Xu, Y., Cerdeira, A., Marsal, L., Ghibaudo, G., Iniguez, B. and Pallares, J. (2012), ‘Effect of density of states on mobility in small-molecule n-type organic thin-film transistors based on a perylene diimide’, *IEEE Electron Device Letters* **33**(8), 1201–1203.

Chao, Y.-C., Chen, C.-Y., Zan, H.-W. and Meng, H.-F. (2010), ‘The influences of device geometry and p-type doping on a solution-processed polymer space-charge-limited transistor’, *Journal of Physics D: Applied Physics* **43**(20), 205101.

Chao, Y.-C., Ku, M.-C., Tsai, W.-W., Zan, H.-W., Meng, H.-F., Tsai, H.-K., Horng, S.-F. et al. (2010), ‘Polymer space-charge-limited transistor as a solid-state vacuum tube triode’, *Applied Physics Letters* **97**(22).

Chao, Y.-C., Lai, W.-J., Chen, C.-Y., Meng, H.-F., Zan, H.-W. and Horng, S.-F. (2009), ‘Low voltage active pressure sensor based on polymer space-charge-limited transistor’, *Applied Physics Letters* **95**(25), 253306.

Chao, Y.-C., Niu, M.-C., Zan, H.-W., Meng, H.-F. and Ku, M.-C. (2011), ‘High-mobility polymer space–charge-limited transistor with grid-induced crystallinity’, *Organic Electronics* **12**(1), 78–82.

Chao, Y.-C., Tsai, H.-K., Zan, H.-W., Hsu, Y.-H., Meng, H.-F. and Horng, S.-F. (2011), 'Enhancement-mode polymer space-charge-limited transistor with low switching swing of 96 mv/decade', *Applied Physics Letters* **98**(22), 223303.

Chao, Y.-C., Tsai, W.-W., Chen, C.-Y., Zan, H.-W., Meng, H.-F., Jiang, S.-L., Chiang, C.-M. and Ku, M.-C. (2009), A 1-v operated polymer vertical transistor with high on/off current ratio, *in* 'Electron Devices Meeting (IEDM), 2009 IEEE International', IEEE, pp. 1–4.

Chen, C.-Y., Chao, Y.-C., Meng, H.-F. and Horng, S.-F. (2008), 'Light-emitting polymer space-charge-limited transistor', *Applied Physics Letters* **93**(22).

Chen, D., Nakahara, A., Wei, D., Nordlund, D. and Russell, T. P. (2010), 'P3ht/pcbm bulk heterojunction organic photovoltaics: correlating efficiency and morphology', *Nano letters* **11**(2), 561–567.

Chen, W., So, F. and Guo, J. (2014), 'Intrinsic delay of permeable base transistor', *Journal of Applied Physics* **116**(4), 044505.

Chen, Y. and Shih, I. (2007), 'Fabrication of vertical channel top contact organic thin film transistors', *Organic Electronics* **8**(6), 655–661.

Chiang, C. K., Fincher Jr, C., Park, Y. W., Heeger, A. J., Shirakawa, H., Louis, E. J., Gau, S. C. and MacDiarmid, A. G. (1977), 'Electrical conductivity in doped polyacetylene', *Physical review letters* **39**(17), 1098.

Cleveland Ashcraft, C., Grimes, R. G., Lewis, J. G., Peyton, B. W., Simon, H. D. and Bjørstad, P. E. (1987), 'Progress in sparse matrix methods for large linear systems on vector supercomputers', *The International Journal of Supercomputing Applications* **1**(4), 10–30.

Colalongo, L., Valdinoci, M., Baccarani, G., Migliorato, P., Tallarida, G. and Reita, C. (1997), 'Numerical analysis of poly-tfts under off conditions', *Solid-State Electronics* **41**(4), 627–633.

Crispin, X., Jakobsson, F., Crispin, A., Grim, P., Andersson, P., Volodin, A., Van Haesendonck, C., Van der Auweraer, M., Salaneck, W. R. and Berggren, M. (2006), 'The origin of the high conductivity of poly (3, 4-ethylenedioxythiophene)-poly (styrenesulfonate)(pedot-pss) plastic electrodes', *Chemistry of Materials* **18**(18), 4354–4360.

Dagum, L. and Menon, R. (1998), ‘Openmp: an industry standard api for shared-memory programming’, *IEEE computational science and engineering* **5**(1), 46–55.

Davids, P., Campbell, I. and Smith, D. (1997), ‘Device model for single carrier organic diodes’, *Journal of Applied Physics* **82**(12), 6319–6325.

de Falco, C., Porro, M., Sacco, R. and Verri, M. (2012), ‘Multiscale modeling and simulation of organic solar cells’, *Computer Methods in Applied Mechanics and Engineering* **245**, 102–116.

Deen, M. J., Marinov, O., Zschieschang, U. and Klauk, H. (2009), ‘Organic thin-film transistors: part iiparameter extraction’, *IEEE Transactions on Electron Devices* **56**(12), 2962–2968.

Deibel, C., Baumann, A. and Dyakonov, V. (2008), ‘Polaron recombination in pristine and annealed bulk heterojunction solar cells’, *Applied Physics Letters* **93**(16), 386.

Deibel, C. and Dyakonov, V. (2010), ‘Polymer–fullerene bulk heterojunction solar cells’, *Reports on Progress in Physics* **73**(9), 096401.

Deibel, C., Strobel, T. and Dyakonov, V. (2010), ‘Role of the charge transfer state in organic donor–acceptor solar cells’, *Advanced Materials* **22**(37), 4097–4111.

Deibel, C., Wagenpfahl, A. and Dyakonov, V. (2008), ‘Influence of charge carrier mobility on the performance of organic solar cells’, *physica status solidi (RRL)-Rapid Research Letters* **2**(4), 175–177.

Delaunay, B. (1934), ‘Sur la sphere vide’, *Izv. Akad. Nauk SSSR, Otdelenie Matematicheskii i Estestvennyka Nauk* **7**(793-800), 1–2.

Dennler, G., Forberich, K., Scharber, M. C., Brabec, C. J., Tomiš, I., Hingerl, K. and Fromherz, T. (2007), ‘Angle dependence of external and internal quantum efficiencies in bulk-heterojunction organic solar cells’, *Journal of Applied Physics* **102**(5), 054516.

Deschamps, P.-Y., Bréon, F.-M., Leroy, M., Podaire, A., Bricaud, A., Buriez, J.-C. and Seze, G. (1994), ‘The polder mission: Instrument characteristics and scientific objectives’, *IEEE Transactions on geoscience and remote sensing* **32**(3), 598–615.

Dongaonkar, S., Servaites, J. D., Ford, G. M., Loser, S., Moore, J., Gelfand, R. M., Mohseni, H., Hillhouse, H. W., Agrawal, R., Ratner, M. A. et al. (2010), 'Universality of non-ohmic shunt leakage in thin-film solar cells', *Journal of Applied Physics* **108**(12), 124509.

Ekinci, Y., Solak, H. H., David, C. and Sigg, H. (2006), 'Bilayer al wire-grids as broadband and high-performance polarizers', *Optics express* **14**(6), 2323–2334.

Estrada, M., Cerdeira, A., Mejia, I., Avila, M., Picos, R., Marsal, L., Pallares, J. and Iñiguez, B. (2010), 'Modeling the behavior of charge carrier mobility with temperature in thin-film polymeric transistors', *Microelectronic Engineering* **87**(12), 2565–2570.

Estrada, M., Cerdeira, A., Puigdollers, J., Resendiz, L., Pallares, J., Marsal, L., Voz, C. and Iñiguez, B. (2005), 'Accurate modeling and parameter extraction method for organic tfts', *Solid-state electronics* **49**(6), 1009–1016.

Estrada, M., Mejia, I., Cerdeira, A., Pallares, J., Marsal, L. and Iñiguez, B. (2008), 'Mobility model for compact device modeling of otfts made with different materials', *Solid-State Electronics* **52**(5), 787–794.

Falco, A. (2016), Printed Components For Organic Electronics, PhD thesis, Technische Universität München.

Falco, A., Cinà, L., Scarpa, G., Lugli, P. and Abdellah, A. (2014), 'Fully-sprayed and flexible organic photodiodes with transparent carbon nanotube electrodes', *ACS applied materials & interfaces* **6**(13), 10593–10601.

Feng, P., Song, S.-C., Nallapati, G., Zhu, J., Bao, J., Moroz, V., Choi, M., Lin, X.-W., Lu, Q., Colombeau, B. et al. (2017), 'Comparative analysis of semiconductor device architectures for 5-nm node and beyond', *IEEE Electron Device Letters* **38**(12), 1657–1660.

Fischer, A., Scholz, R., Leo, K. and Lüssem, B. (2012), 'An all c60 vertical transistor for high frequency and high current density applications', *Applied Physics Letters* **101**(21), 213303.

Fischer, A., Siebeneicher, P., Kleemann, H., Leo, K. and Lüssem, B. (2012), 'Bidirectional operation of vertical organic triodes', *Journal of Applied Physics* **111**(4), 044507.

French, R. H., Müllejans, H. and Jones, D. J. (1998), 'Optical properties of aluminum oxide: determined from vacuum ultraviolet and electron energy-loss spectroscopies', *Journal of the American Ceramic Society* **81**(10), 2549–2557.

Frenkel, J. (1938), 'On pre-breakdown phenomena in insulators and electronic semi-conductors', *Physical Review* **54**(8), 647.

Fujimoto, S.-Y., Nakayama, K.-I. and Yokoyama, M. (2005), 'Fabrication of a vertical-type organic transistor with a planar metal base', *Applied Physics Letters* **87**(13), 133503.

Furno, M., Kleemann, H., Schwartz, G. and Blochwitz-Nimoth, J. (2015), 39.4 l: Late-news paper: Vertical organic transistors (v-ofets) for truly flexible amoled displays, *in* 'SID Symposium Digest of Technical Papers', Vol. 46, Wiley Online Library, pp. 597–600.

Ghezzi, D., Antognazza, M. R., Maccarone, R., Bellani, S., Lanzarini, E., Martino, N., Mete, M., Pertile, G., Bisti, S., Lanzani, G. et al. (2013), 'A polymer optoelectronic interface restores light sensitivity in blind rat retinas', *Nature Photonics* **7**(5), 400–406.

Gosney, W. (1972), 'Subthreshold drain leakage currents in mos field-effect transistors', *IEEE transactions on Electron Devices* **19**(2), 213–219.

Goudon, T., Miljanović, V. and Schmeiser, C. (2007), 'On the shockley–read–hall model: generation-recombination in semiconductors', *SIAM Journal on Applied Mathematics* **67**(4), 1183–1201.

Grancini, G., Maiuri, M., Fazzi, D., Petrozza, A., Egelhaaf, H., Brida, D., Cerullo, G. and Lanzani, G. (2013), 'Hot exciton dissociation in polymer solar cells', *Nature materials* **12**(1), 29–33.

Greczynski, G., Kugler, T., Keil, M., Osikowicz, W., Fahlman, M. and Salaneck, W. R. (2001), 'Photoelectron spectroscopy of thin films of pedot–pss conjugated polymer blend: a mini-review and some new results', *Journal of Electron Spectroscopy and Related Phenomena* **121**(1), 1–17.

Greenman, M., Ben-Sasson, A. J., Chen, Z., Facchetti, A. and Tessler, N. (2013), 'Fast switching characteristics in vertical organic field effect transistors', *Applied Physics Letters* **103**(7), 073502.

Gupta, D., Katiyar, M. and Gupta, D. (2009), 'An analysis of the difference in behavior of top and bottom contact organic thin film transistors using device simulation', *Organic Electronics* **10**(5), 775–784.

Hall, R. N. (1952), 'Electron-hole recombination in germanium', *Physical review* **87**(2), 387.

Han, S., Huang, C. and Lu, Z.-H. (2005), 'Color tunable metal-cavity organic light-emitting diodes with fullerene layer', *Journal of applied physics* **97**(9), 093102.

Hecht, E. (2002), 'Optics, 4th', *International edition, Addison-Wesley, San Francisco* **3**.

Heeger, A. J. (2001), 'Semiconducting and metallic polymers: the fourth generation of polymeric materials (nobel lecture)', *Angewandte Chemie International Edition* **40**(14), 2591–2611.

Helfrich, W. and Schneider, W. (1965), 'Recombination radiation in anthracene crystals', *Physical Review Letters* **14**(7), 229.

Helfrich, W. and Schneider, W. (1966), 'Transients of volume-controlled current and of recombination radiation in anthracene', *The Journal of Chemical Physics* **44**(8), 2902–2909.

Hirashima, N., Ohashi, N., Nakamura, M. and Kudo, K. (2005), Fabrication of organic vertical-type field-effect transistors using polystyrene spheres as evaporation mask, *in* 'Proc. Int. Symp. Super Functionality Organic Devices, IPAP Conference Series', Vol. 6, pp. 158–160.

Hoppe, H. and Sariciftci, N. S. (2004), 'Organic solar cells: An overview', *Journal of Materials Research* **19**(07), 1924–1945.

Horio, K. and Yanai, H. (1990), 'Numerical modeling of heterojunctions including the thermionic emission mechanism at the heterojunction interface', *IEEE Transactions on Electron Devices* **37**(4), 1093–1098.

Horowitz, G., Hajlaoui, R. and Delannoy, P. (1995), 'Temperature dependence of the field-effect mobility of sexithiophene. determination of the density of traps', *Journal de Physique III* **5**(4), 355–371.

Hsu, Y., Fang, X., Wang, L. A., Zan, H.-W., Meng, H.-F. and Yang, S.-H. (2014), ‘Sub-100nm ald-assisted nanoimprint lithography for realizing vertical organic transistors with high on/off ratio and high output current’, *Organic Electronics* **15**(12), 3609–3614.

Huang, J., Miller, P. F., Wilson, J. S., de Mello, A. J., de Mello, J. C. and Bradley, D. D. (2005), ‘Investigation of the effects of doping and post-deposition treatments on the conductivity, morphology, and work function of poly (3, 4-ethylenedioxythiophene)/poly (styrene sulfonate) films’, *Advanced Functional Materials* **15**(2), 290–296.

Hurkx, G., De Graaff, H., Kloosterman, W. and Knuvers, M. (1992), ‘A new analytical diode model including tunneling and avalanche breakdown’, *IEEE Transactions on electron devices* **39**(9), 2090–2098.

Hurkx, G., Klaassen, D. and Knuvers, M. (1992), ‘A new recombination model for device simulation including tunneling’, *IEEE Transactions on electron devices* **39**(2), 331–338.

Iechi, H., Watanabe, Y., Yamauchi, H. and Kudo, K. (2010), ‘Organic inverter using monolithically stacked static induction transistors’, *Japanese Journal of Applied Physics* **49**(1S), 01AB12.

Ising, E. (1925), ‘Beitrag zur theorie des ferromagnetismus’, *Zeitschrift für Physik A Hadrons and Nuclei* **31**(1), 253–258.

Jacoboni, C. and Lugli, P. (2012), *The Monte Carlo method for semiconductor device simulation*, Springer Science & Business Media.

Jacques, S. L. (2013), ‘Optical properties of biological tissues: a review’, *Physics in medicine and biology* **58**(11), R37.

Jimenez-Gonzalez, A. and Schmeisser, D. (1991), ‘Preparation and spectroscopic characterization of γ-al 2 o 3 thin films’, *Surface science* **250**(1), 59–70.

Johnson, L. E. (1995), ‘Enhanced early detection and enumeration of zebra mussel (dreissena spp.) veligers using cross-polarized light microscopy’, *Hydrobiologia* **312**(2), 139–146.

Johnston, D. E., Yager, K. G., Nam, C.-Y., Ocko, B. M. and Black, C. T. (2012), ‘One-volt operation of high-current vertical channel polymer semiconductor field-effect transistors’, *Nano letters* **12**(8), 4181–4186.

Jönsson, S., Birgerson, J., Crispin, X., Greczynski, G., Osikowicz, W., Van Der Gon, A. D., Salaneck, W. R. and Fahlman, M. (2003), 'The effects of solvents on the morphology and sheet resistance in poly (3, 4-ethylenedioxythiophene)–polystyrenesulfonic acid (pedot–pss) films', *Synthetic Metals* **139**(1), 1–10.

Juška, G., Genevičius, K., Nekrašas, N., Sliaužys, G. and Dennler, G. (2008), 'Trimolecular recombination in polythiophene: fullerene bulk heterojunction solar cells', *Applied Physics Letters* **93**(14), 369.

Juška, G., Genevičius, K., Österbacka, R., Arlauskas, K., Kreouzis, T., Bradley, D. and Stubb, H. (2003), 'Initial transport of photogenerated charge carriers in -conjugated polymers', *Physical Review B* **67**(8), 081201.

Kaschura, F., Fischer, A., Kasemann, D., Leo, K. and Lüssem, B. (2015), 'Controlling morphology: A vertical organic transistor with a self-structured permeable base using the bottom electrode as seed layer', *Applied Physics Letters* **107**(3), 033301.

Katsidis, C. C. and Siapkas, D. I. (2002), 'General transfer-matrix method for optical multilayer systems with coherent, partially coherent, and incoherent interference', *Applied optics* **41**(19), 3978–3987.

Kim, C.-H., Bonnassieux, Y. and Horowitz, G. (2014), 'Compact dc modeling of organic field-effect transistors: Review and perspectives', *IEEE Transactions on Electron Devices* **61**(2), 278–287.

Kim, C. H., Castro-Carranza, A., Estrada, M., Cerdeira, A., Bonnassieux, Y., Horowitz, G. and Iñiguez, B. (2013), 'A compact model for organic field-effect transistors with improved output asymptotic behaviors', *IEEE Transactions on Electron Devices* **60**(3), 1136–1141.

Kim, H., Gilmore, C., Pique, A., Horwitz, J., Mattoussi, H., Murata, H., Kafafi, Z. and Chrisey, D. (1999), 'Electrical, optical, and structural properties of indium–tin–oxide thin films for organic light-emitting devices', *Journal of Applied Physics* **86**(11), 6451–6461.

Kim, K. and Kim, Y. (2010), 'Intrinsic capacitance characteristics of top-contact organic thin-film transistors', *IEEE Transactions on Electron Devices* **57**(9), 2344–2347.

Kim, Y. H., Sachse, C., Machala, M. L., May, C., Müller-Meskamp, L. and Leo, K. (2011), 'Highly conductive pedot: Pss electrode with optimized solvent and thermal post-treatment for ito-free organic solar cells', *Advanced Functional Materials* **21**(6), 1076–1081.

Kippelen, B. and Brédas, J.-L. (2009), 'Organic photovoltaics', *Energy & Environmental Science* **2**(3), 251–261.

Klauk, H. (2010), 'Organic thin-film transistors', *Chemical Society Reviews* **39**(7), 2643–2666.

Kleemann, H., Günther, A. A., Leo, K. and Lüssem, B. (2013), 'High-performance vertical organic transistors', *Small* **9**(21), 3670–3677.

Kleemann, H., Lüssem, B. and Leo, K. (2012), 'Controlled formation of charge depletion zones by molecular doping in organic pin-diodes and its description by the mott-schottky relation', *Journal of Applied Physics* **111**(12), 123722.

Köhler, A. and Bässler, H. (2015), *Electronic processes in organic semiconductors: An introduction*, John Wiley & Sons.

Kong, Y. L., Tamargo, I. A., Kim, H., Johnson, B. N., Gupta, M. K., Koh, T.-W., Chin, H.-A., Steingart, D. A., Rand, B. P. and McAlpine, M. C. (2014), '3d printed quantum dot light-emitting diodes', *Nano letters* **14**(12), 7017–7023.

Kordt, P., van der Holst, J. J., Al Helwi, M., Kowalsky, W., May, F., Badinski, A., Lennartz, C. and Andrienko, D. (2015), 'Modeling of organic light emitting diodes: From molecular to device properties', *Advanced Functional Materials* **25**(13), 1955–1971.

Koster, L., Mihailetchi, V. and Blom, P. (2006), 'Bimolecular recombination in polymer/fullerene bulk heterojunction solar cells', *Applied physics letters* **88**(5), 052104.

Koster, L., Smits, E., Mihailetchi, V. and Blom, P. (2005), 'Device model for the operation of polymer/fullerene bulk heterojunction solar cells', *Physical Review B* **72**(8), 085205.

Kudo, K., Iizuka, M., Kuniyoshi, S. and Tanaka, K. (2001), 'Device characteristics of lateral and vertical type organic field effect transistors', *Thin Solid Films* **393**(1), 362–367.

Kudo, K., Shimada, K., Marugami, K., Iizuka, M., Kuniyoshi, S. and Tanaka, K. (1999), 'Organic static induction transistor for color sensors', *Synthetic metals* **102**(1), 900–903.

Kudo, K., Takano, T., Yamauchi, H., Iizuka, M. and Nakamura, M. (2010), 'High-speed operation of step-edge vertical-channel organic transistors with pentacene and 6, 13-bis (triisopropyl-silylethynyl) pentacene', *Japanese Journal of Applied Physics* **49**(4S), 04DK03.

Kudo, K., Wang, D., Iizuka, M., Kuniyoshi, S. and Tanaka, K. (2000), 'Organic static induction transistor for display devices', *Synthetic Metals* **111**, 11–14.

Kurosawa, T. (1966), Monte carlo calculation of hot electron problems, *in* 'Proceedings of the International Conference on the Physics of Semiconductors', Vol. 21, pp. 424–426.

Kwiatkowski, J., Nelson, J., Li, H., Bredas, J., Wenzel, W. and Lennartz, C. (2008), 'Simulating charge transport in tris (8-hydroxyquinoline) aluminium (alq 3)', *Physical Chemistry Chemical Physics* **10**(14), 1852–1858.

Lampert, M. A. and Mark, P. (1970), 'Current injection in solids'.

Langevin, P. (1903), 'Recombinaison et mobilites des ions dans les gaz', *Ann. Chim. Phys* **28**(433), 122.

Lanzani, G. (2012), *The photophysics behind photovoltaics and photonics*, John Wiley & Sons.

Larson, B. W., Whitaker, J. B., Wang, X.-B., Popov, A. A., Rumbles, G., Kopidakis, N., Strauss, S. H. and Boltalina, O. V. (2013), 'Electron affinity of phenyl–c61–butyric acid methyl ester (pcbm)', *The Journal of Physical Chemistry C* **117**(29), 14958–14964.

Law, M. E. (2016), 20 years of sispad: Adolescence of tcad and further perspective, *in* 'Simulation of Semiconductor Processes and Devices (SISPAD), 2016 International Conference on', IEEE, pp. 1–6.

Lee, T. H. (2007), 'The (pre-) history of the integrated circuit: a random walk', *IEEE Solid-State Circuits Society Newsletter* **12**(2), 16–22.

Lee, W., Chuang, S., Chen, H., Su, W. and Lin, C. (2010), 'Exploiting optical properties of p3ht: Pcbm films for organic solar cells with semitransparent anode', *Thin Solid Films* **518**(24), 7450–7454.

Li, L., Debucquoy, M., Genoe, J. and Heremans, P. (2010), ‘A compact model for polycrystalline pentacene thin-film transistor’, *Journal of Applied Physics* **107**(2), 024519.

Li, S.-H., Xu, Z., Ma, L., Chu, C.-W. and Yang, Y. (2007), ‘Achieving ambipolar vertical organic transistors via nanoscale interface modification’, *Applied Physics Letters* **91**(8), 083507.

Li, S.-H., Xu, Z., Yang, G., Ma, L. and Yang, Y. (2008), ‘Solution-processed poly (3-hexylthiophene) vertical organic transistor’, *Applied Physics Letters* **93**(21), 213301.

Licciardo, G. D., Di Benedetto, L. and Bellone, S. (2016), ‘Modeling of the sio 2/sic interface-trapped charge as a function of the surface potential in 4h-sic vertical-dmosfet’, *IEEE Transactions on Electron Devices* **63**(4), 1783–1787.

Lin, H.-C., Zan, H.-W., Chao, Y.-C., Chang, M.-Y. and Meng, H.-F. (2015), ‘Review of a solution-processed vertical organic transistor as a solid-state vacuum tube’, *Semiconductor Science and Technology* **30**(5), 054003.

Lin, H.-C., Zan, H.-W. and Meng, H.-F. (2014), ‘Achieving good bias stress reliability in organic transistor with vertical channel’, *Organic Electronics* **15**(7), 1531–1535.

Liu, B., McCarthy, M. A. and Rinzler, A. G. (2010), ‘Non-volatile organic memory elements based on carbon-nanotube-enabled vertical field-effect transistors’, *Advanced Functional Materials* **20**(20), 3440–3445.

Liu, B., McCarthy, M. A., Yoon, Y., Kim, D. Y., Wu, Z., So, F., Holloway, P. H., Reynolds, J. R., Guo, J. and Rinzler, A. G. (2008), ‘Carbon-nanotube-enabled vertical field effect and light-emitting transistors’, *Advanced Materials* **20**(19), 3605–3609.

Lochmann, W. and Haug, A. (1980), ‘Phonon-assisted auger recombination in si with direct calculation of the overlap integrals’, *Solid State Communications* **35**(7), 553–556.

Lüssem, B., Günther, A., Fischer, A., Kasemann, D. and Leo, K. (2015), ‘Vertical organic transistors’, *Journal of Physics: Condensed Matter* **27**(44), 443003.

Lüssem, B., Tietze, M. L., Fischer, A., Pahner, P., Kleemann, H., Günther, A., Kasemann, D. and Leo, K. (2014), Beyond conventional organic transistors: novel approaches with improved performance and stability, *in* 'SPIE Organic Photonics+ Electronics', International Society for Optics and Photonics, pp. 91850H–91850H.

Ma, L. and Yang, Y. (2004), 'Unique architecture and concept for high-performance organic transistors', *Applied physics letters* **85**(21), 5084–5086.

Marinov, O., Deen, M. and Datars, R. (2009), 'Compact modeling of charge carrier mobility in organic thin-film transistors', *Journal of Applied Physics* **106**(6), 064501.

Marinov, O., Deen, M. J., Zschieschang, U. and Klauk, H. (2009), 'Organic thin-film transistors: Part icompact dc modeling', *IEEE Transactions on Electron Devices* **56**(12), 2952–2961.

McCarthy, M. A., Liu, B. and Rinzler, A. G. (2010), 'High current, low voltage carbon nanotube enabled vertical organic field effect transistors', *Nano letters* **10**(9), 3467–3472.

McCarthy, M., Liu, B., Donoghue, E., Kravchenko, I., Kim, D., So, F. and Rinzler, A. (2011), 'Low-voltage, low-power, organic light-emitting transistors for active matrix displays', *Science* **332**(6029), 570–573.

Meijer, E., Tanase, C., Blom, P., Van Veenendaal, E., Huisman, B.-H., De Leeuw, D. and Klapwijk, T. (2002), 'Switch-on voltage in disordered organic field-effect transistors', *Applied Physics Letters* **80**(20), 3838–3840.

Metropolis, N., Rosenbluth, A. W., Rosenbluth, M. N., Teller, A. H. and Teller, E. (1953), 'Equation of state calculations by fast computing machines', *The journal of chemical physics* **21**(6), 1087–1092.

Miller, A. and Abrahams, E. (1960), 'Impurity conduction at low concentrations', *Physical Review* **120**(3), 745.

Miyadera, T., Minari, T., Tsukagoshi, K., Ito, H. and Aoyagi, Y. (2007), 'Frequency response analysis of pentacene thin-film transistors with low impedance contact by interface molecular doping', *Applied physics letters* **91**(1), 013512.

Monestier, F., Simon, J.-J., Torchio, P., Escoubas, L., Flory, F., Bailly, S., de Bettignies, R., Guillerez, S. and Defranoux, C. (2007), 'Modeling the short-circuit current density of polymer solar cells based on p3ht: Pcbm blend', *Solar energy materials and solar cells* **91**(5), 405–410.

Mott, N. (1968), 'Conduction in glasses containing transition metal ions', *Journal of Non-Crystalline Solids* **1**(1), 1–17.

Movaghar, B., Grünewald, M., Ries, B., Bassler, H. and Würtz, D. (1986), 'Diffusion and relaxation of energy in disordered organic and inorganic materials', *Physical Review B* **33**(8), 5545.

Nagata, Y. and Lennartz, C. (2008), 'Atomistic simulation on charge mobility of amorphous tris (8-hydroxyquinoline) aluminum (alq 3): Origin of poole–frenkel–type behavior', *The Journal of chemical physics* **129**(3), 034709.

Nagel, R. D., Haeberle, T., Schmidt, M., Lugli, P. and Scarpa, G. (2016), 'Large area nano-transfer printing of sub-50-nm metal nanostructures using low-cost semi-flexible hybrid templates', *Nanoscale research letters* **11**(1), 143.

Nakamura, K., Hata, T., Yoshizawa, A., Obata, K., Endo, H. and Kudo, K. (2006), 'Metal-insulator-semiconductor-type organic light-emitting transistor on plastic substrate', *Applied physics letters* **89**(10), 103525.

Nakamura, K., Hata, T., Yoshizawa, A., Obata, K., Endo, H. and Kudo, K. (2008), 'Improvement of metal–insulator–semiconductor-type organic light-emitting transistors', *Japanese Journal of Applied Physics* **47**(3S), 1889.

Nakayama, K.-I., Fujimoto, S.-Y. and Yokoyama, M. (2009), 'Improvement in the on/off ratio of a vertical-type metal-base organic transistor by heat treatment in air', *Organic Electronics* **10**(3), 543–546.

Naruse, H., Naka, S. and Okada, H. (2008), 'Dual self-aligned vertical multichannel organic transistors', *Applied physics express* **1**(1), 011801.

Nau, S., Wolf, C., Sax, S. and List-Kratochvil, E. J. (2015), 'Organic nonvolatile resistive photo-switches for flexible image detector arrays', *Advanced Materials* **27**(6), 1048–1052.

Ng, K. K. (2002), *Complete Guide to Semiconductor Devices, 2nd Edition*, Wiley-IEEE Press.

Ng, T. N., Wong, W. S., Chabinyc, M. L., Sambandan, S. and Street, R. A. (2008), 'Flexible image sensor array with bulk heterojunction organic photodiode', *Applied Physics Letters* **92**(21), 213303.

Nicollian, E. and Goetzberger, A. (1967), 'The si-sio2 interface–electrical properties as determined by the metal-insulator-silicon conductance technique', *Bell System Technical Journal* **46**(6), 1055–1133.

Nicollian, E. H. and Brews, J. R. (1982), *MOS (metal oxide semiconductor) physics and technology*, Vol. 1987, Wiley New York et al.

Nilsson, P. and Forssell, G. (1977), 'Optical properties of calcium', *Physical Review B* **16**(8), 3352.

Nishizawa, J. and Terasaki, T. (1972), A low impedance field effect transistor, *in* '1972 International Electron Devices Meeting', Vol. 18, IEEE, pp. 144–144.

Novikova, T., Pierangelo, A., De Martino, A., Benali, A. and Validire, P. (2012), 'Polarimetric imaging for cancer diagnosis and staging', *Optics and photonics news* **23**(10), 26–33.

Nowy, S., Ren, W., Elschner, A., Lövenich, W. and Brütting, W. (2010), 'Impedance spectroscopy as a probe for the degradation of organic light-emitting diodes', *Journal of Applied Physics* **107**(5), 054501.

Onsager, L. (1938), 'Initial recombination of ions', *Physical Review* **54**(8), 554.

Ou, T.-M., Cheng, S.-S., Huang, C.-Y., Wu, M.-C., Chan, I.-M., Lin, S.-Y. and Chan, Y.-J. (2006), 'All-organic hot-carrier triodes with thin-film metal base', *Applied physics letters* **89**(18), 183508.

Paasch, G. and Scheinert, S. (2010), 'Charge carrier density of organics with gaussian density of states: analytical approximation for the gauss–fermi integral', *Journal of Applied Physics* **107**(10), 104501.

Pais, A., Banerjee, A., Klotzkin, D. and Papautsky, I. (2008), 'High-sensitivity, disposable lab-on-a-chip with thin-film organic electronics for fluorescence detection', *Lab on a Chip* **8**(5), 794–800.

Parashkov, R., Becker, E., Hartmann, S., Ginev, G., Schneider, D., Krautwald, H., Dobbertin, T., Metzdorf, D., Brunetti, F., Schildknecht, C. et al. (2003), ‘Vertical channel all-organic thin-film transistors’, *Applied physics letters* **82**(25), 4579–4580.

Park, Y., Choong, V., Gao, Y., Hsieh, B. and Tang, C. (1996), ‘Work function of indium tin oxide transparent conductor measured by photoelectron spectroscopy’, *Applied Physics Letters* **68**(19), 2699–2701.

Pasveer, W., Cottaar, J., Tanase, C., Coehoorn, R., Bobbert, P., Blom, P., De Leeuw, D. and Michels, M. (2005), ‘Unified description of charge-carrier mobilities in disordered semiconducting polymers’, *Physical review letters* **94**(20), 206601.

Petrosino, M. and Rubino, A. (2011), ‘Admittance spectroscopy of poly (3, 4-ethylenedioxythiophene): poly (styrenesulfonate) based organic light emitting diodes’, *Journal of Applied Physics* **109**(11), 114504.

Pettersson, L. A., Ghosh, S. and Inganäs, O. (2002), ‘Optical anisotropy in thin films of poly (3, 4-ethylenedioxythiophene)–poly (4-styrenesulfonate)’, *Organic electronics* **3**(3), 143–148.

Piris, J., Dykstra, T. E., Bakulin, A. A., Loosdrecht, P. H. v., Knulst, W., Trinh, M. T., Schins, J. M. and Siebbeles, L. D. (2009), ‘Photogeneration and ultrafast dynamics of excitons and charges in p3ht/pcbm blends’, *The Journal of Physical Chemistry C* **113**(32), 14500–14506.

Pope, M., Kallmann, H. and Magnante, P. (1963), ‘Electroluminescence in organic crystals’, *The Journal of Chemical Physics* **38**(8), 2042–2043.

Popescu, B. V., Popescu, D. H., Lugli, P., Locci, S., Arca, F., Tedde, S. F., Sramek, M. and Hayden, O. (2013), ‘Modeling and simulation of organic photodetectors for low light intensity applications’, *IEEE Transactions on Electron Devices* **60**(6), 1975–1981.

Proctor, C. M., Kuik, M. and Nguyen, T.-Q. (2013), ‘Charge carrier recombination in organic solar cells’, *Progress in Polymer Science* **38**(12), 1941–1960.

Rauch, T., Böberl, M., Tedde, S. F., Fürst, J., Kovalenko, M. V., Hesser, G., Lemmer, U., Heiss, W. and Hayden, O. (2009), ‘Near-infrared imaging with quantum-dot-sensitized organic photodiodes’, *nature photonics* **3**(6), 332–336.

Reineke, S., Lindner, F., Schwartz, G., Seidler, N., Walzer, K., Lüssem, B. and Leo, K. (2009), 'White organic light-emitting diodes with fluorescent tube efficiency', *Nature* **459**(7244), 234–238.

Reineke, S., Thomschke, M., Lüssem, B. and Leo, K. (2013), 'White organic light-emitting diodes: Status and perspective', *Reviews of Modern Physics* **85**(3), 1245.

Riede, M., Lüssem, B. and Leo, K. (2011), 'Organic semiconductors', *Comprehensive semiconductor science and technology* pp. 448–507.

Rodenhuis, M., Canovas, H., Jeffers, S., Ovelar, M., Homs, L., Min, M. and Keller, C. (2012), 'The extreme polarimeter: Design, performance, first results & upgrades', *arXiv preprint arXiv:1211.6300* .

Roosbroeck, W. v. (1950), 'Theory of the flow of electrons and holes in germanium and other semiconductors', *Bell Labs Technical Journal* **29**(4), 560–607.

Ruhstaller, B., Beierlein, T., Riel, H., Karg, S., Scott, J. C. and Riess, W. (2003), 'Simulating electronic and optical processes in multilayer organic light-emitting devices', *IEEE Journal of Selected Topics in Quantum Electronics* **9**(3), 723–731.

Scarpa, G., Idzko, A.-L., Götz, S. and Thalhammer, S. (2010), 'Biocompatibility studies of functionalized regioregular poly (3-hexylthiophene) layers for sensing applications', *Macromolecular bioscience* **10**(4), 378–383.

Scheinert, S. and Paasch, G. (2004), 'Fabrication and analysis of polymer field-effect transistors', *physica status solidi (a)* **201**(6), 1263–1301.

Scheinert, S., Paasch, G., Schrödner, M., Roth, H.-K., Sensfuß, S. and Doll, T. (2002), 'Subthreshold characteristics of field effect transistors based on poly (3-dodecylthiophene) and an organic insulator', *Journal of Applied Physics* **92**(1), 330–337.

Scheinert, S., Pernstich, K. P., Batlogg, B. and Paasch, G. (2007), 'Determination of trap distributions from current characteristics of pentacene field-effect transistors with surface modified gate oxide', *Journal of Applied Physics* **102**(10), 104503.

Schenk, A. (2012), *Advanced physical models for silicon device simulation*, Springer Science & Business Media.

Schenk, O. (2000), Scalable parallel sparse LU factorization methods on shared memory multiprocessors, PhD thesis.

Schwoerer, M. and Wolf, H. C. (2007), *Organic molecular solids*, John Wiley & Sons.

Scott, J. C. (2003), 'Metal–organic interface and charge injection in organic electronic devices', *Journal of Vacuum Science & Technology A: Vacuum, Surfaces, and Films* **21**(3), 521–531.

Selberherr, S. (2012), *Analysis and simulation of semiconductor devices*, Springer Science & Business Media.

Sharma, A., Janssen, N., Mathijssen, S., de Leeuw, D., Kemerink, M. and Bobbert, P. (2011), 'Effect of coulomb scattering from trapped charges on the mobility in an organic field-effect transistor', *Physical Review B* **83**(12), 125310.

She, X.-J., Gustafsson, D. and Sirringhaus, H. (2017), 'A vertical organic transistor architecture for fast nonvolatile memory', *Advanced Materials* **29**(8).

Shen, Y., Hosseini, A. R., Wong, M. H. and Malliaras, G. G. (2004), 'How to make ohmic contacts to organic semiconductors', *ChemPhysChem* **5**(1), 16–25.

Shockley, W. (1952), 'Transistor electronics: Imperfections, unipolar and analog transistors', *Proceedings of the IRE* **40**(11), 1289–1313.

Shockley, W. (1976), 'The path to the conception of the junction transistor', *IEEE Transactions on Electron Devices* **23**(7), 597–620.

Shockley, W. and Read Jr, W. (1952), 'Statistics of the recombinations of holes and electrons', *Physical review* **87**(5), 835.

Shur, M. (1990), *Physics of semiconductor devices*, Prentice-Hall, Inc.

Shur, M. and Hack, M. (1984), 'Physics of amorphous silicon based alloy field-effect transistors', *Journal of Applied Physics* **55**(10), 3831–3842.

Simmons, J. and Taylor, G. (1971), 'Nonequilibrium steady-state statistics and associated effects for insulators and semiconductors containing an arbitrary distribution of traps', *Physical Review B* **4**(2), 502.

Simmons, J. and Taylor, G. (1975), ‘The theory of photoconductivity in defect insulators containing discrete trap levels’, *Journal of Physics C: Solid State Physics* **8**(20), 3353.

Snik, F., Craven-Jones, J., Escuti, M., Fineschi, S., Harrington, D., De Martino, A., Mawet, D., Riedi, J. and Tyo, J. S. (2014), An overview of polarimetric sensing techniques and technology with applications to different research fields, *in* ‘Proc. SPIE’, Vol. 9099, p. 90990B.

Stallinga, P. (2009), *Electrical Characterization of Organic Electronic Materials and Devices*, John Wiley & Sons.

Stallinga, P. (2011), ‘Electronic transport in organic materials: Comparison of band theory with percolation/(variable range) hopping theory’, *Advanced Materials* **23**(30), 3356–3362.

Stallinga, P., Benvenho, A., Smits, E., Mathijssen, S., Cölle, M., Gomes, H. L. and De Leeuw, D. M. (2008), ‘Determining carrier mobility with a metal–insulator–semiconductor structure’, *Organic Electronics* **9**(5), 735–739.

Steudel, S., Myny, K., Schols, S., Vicca, P., Smout, S., Tripathi, A., van der Putten, B., van der Steen, J.-L., van Neer, M., Schtze, F., Hild, O. R., van Veenendaal, E., van Lieshout, P., van Mil, M., Genoe, J., Gelinck, G. and Heremans, P. (2012), ‘Design and realization of a flexible qqvga amoled display with organic tfts’, *Organic Electronics* **13**(9), 1729–1735.

Street, R., Schoendorf, M., Roy, A. and Lee, J. (2010), ‘Interface state recombination in organic solar cells’, *Physical Review B* **81**(20), 205307.

Sugiyama, K., Ishii, H., Ouchi, Y. and Seki, K. (2000), ‘Dependence of indium–tin–oxide work function on surface cleaning method as studied by ultraviolet and x-ray photoemission spectroscopies’, *Journal of Applied Physics* **87**(1), 295–298.

Synopsys (2015), *Sentaurus Device User Guide, Version K-2015.06, Synopsys Inc.*

Synowicki, R. (1998), ‘Spectroscopic ellipsometry characterization of indium tin oxide film microstructure and optical constants’, *Thin Solid Films* **313**, 394–397.

Sze, S. (1981), ‘Physics of semiconductor devices. new york: J’, *Whiley and Sons* .

Taflove, A. and Hagness, S. C. (2005), *Computational electrodynamics: the finite-difference time-domain method*, Artech house.

Tang, C. W. and VanSlyke, S. A. (1987), ‘Organic electroluminescent diodes’, *Applied physics letters* **51**(12), 913–915.

Tengstedt, C., Osikowicz, W., Salaneck, W. R., Parker, I. D., Hsu, C.-H. and Fahlman, M. (2006), ‘Fermi-level pinning at conjugated polymer interfaces’, *Applied Physics Letters* **88**(5), 053502.

Tessler, N., Preezant, Y., Rappaport, N. and Roichman, Y. (2009), ‘Charge transport in disordered organic materials and its relevance to thin-film devices: A tutorial review’, *Advanced Materials* **21**(27), 2741–2761.

Triebl, O. (2012), Reliability Issues in High-Voltage Semiconductor Devices, PhD thesis, Technischen Universit´at Wien.

Tsoi, W. C., Spencer, S. J., Yang, L., Ballantyne, A. M., Nicholson, P. G., Turnbull, A., Shard, A. G., Murphy, C. E., Bradley, D. D., Nelson, J. et al. (2011), ‘Effect of crystallization on the electronic energy levels and thin film morphology of p3ht: Pcbm blends’, *Macromolecules* **44**(8), 2944–2952.

Tyo, J., Rowe, M., Pugh, E. and Engheta, N. (1996), ‘Target detection in optically scattering media by polarization-difference imaging’, *Applied optics* **35**(11), 1855–1870.

Umetsu, K., Akiba, R., Nakayama, K. and Kido, J. (2013), ‘Polymer material dependence in the polymer/small molecule metal-base organic transistors’, *Molecular Crystals and Liquid Crystals* **580**(1), 117–124.

Uno, M., Doi, I., Takimiya, K. and Takeya, J. (2009), ‘Three-dimensional organic field-effect transistors with high output current and high on-off ratio’, *Applied Physics Letters* **94**(10), 103307.

Uno, M., Hirose, Y., Uemura, T., Takimiya, K., Nakazawa, Y. and Takeya, J. (2010), ‘High-power and high-speed organic three-dimensional transistors with submicrometer channels’, *Applied Physics Letters* **97**(1), 013301.

Uno, M., Nakayama, K., Soeda, J., Hirose, Y., Miwa, K., Uemura, T., Nakao, A., Takimiya, K. and Takeya, J. (2011), ‘High-speed flexible organic field-effect transistors with a 3d structure’, *Advanced Materials* **23**(27), 3047–3051.

Velmre, E. (2007), Thomas johann seebeck (1770-1831), *in* 'Proceedings of the Estonian Academy of Sciences: Engineering', Vol. 13, Estonian Academy Publishers, pp. 276–283.

Vissenberg, M. and Matters, M. (1998), 'Theory of the field-effect mobility in amorphous organic transistors', *Physical Review B* **57**(20), 12964.

Voigt, M. and Sokolowski, M. (2004), 'Electrical properties of thin rf sputtered aluminum oxide films', *Materials Science and Engineering: B* **109**(1), 99–103.

Wachutka, G. K. (1990), 'Rigorous thermodynamic treatment of heat generation and conduction in semiconductor device modeling', *IEEE transactions on computer-aided design of integrated circuits and systems* **9**(11), 1141–1149.

Walker, A., Kambili, A. and Martin, S. (2002), 'Electrical transport modelling in organic electroluminescent devices', *Journal of physics: condensed matter* **14**(42), 9825.

Wang, D. X., Tanaka, Y., Iizuka, M., Kuniyoshi, S., Kudo, K. and Tanaka, K. (1999), 'Device characteristics of organic static induction transistor using copper phthalocyanine films and al gate electrode', *Japanese journal of applied physics* **38**(1R), 256.

Wang, H., Wang, H.-Y., Gao, B.-R., Wang, L., Yang, Z.-Y., Du, X.-B., Chen, Q.-D., Song, J.-F. and Sun, H.-B. (2011), 'Exciton diffusion and charge transfer dynamics in nano phase-separated p3ht/pcbm blend films', *Nanoscale* **3**(5), 2280–2285.

Watanabe, Y., Iechi, H. and Kudo, K. (2006), 'Improvement in on/off ratio of pentacene static induction transistors with ultrathin cupc layer', *Japanese journal of applied physics* **45**(4S), 3698.

Watanabe, Y., Iechi, H. and Kudo, K. (2007), 'Improvement in on/off ratio of pentacene static induction transistors by controlling hole injection barrier', *Japanese journal of applied physics* **46**(4S), 2717.

Watanabe, Y. and Kudo, K. (2005), 'Flexible organic static induction transistors using pentacene thin films', *Applied Physics Letters* **87**(22), 223505.

Watkins, P. K., Walker, A. B. and Verschoor, G. L. (2005), 'Dynamical monte carlo modelling of organic solar cells: The dependence of internal quantum efficiency on morphology', *Nano letters* **5**(9), 1814–1818.

Williams, G., Backhouse, C. and Aziz, H. (2014), ‘Integration of organic light emitting diodes and organic photodetectors for lab-on-a-chip bio-detection systems’, *Electronics* **3**(1), 43–75.

Windbacher, T., Sverdlov, V. and Selberherr, S. (2011), Classical device modeling, *in* ‘Nano-Electronic Devices’, Springer, pp. 1–96.

Wolf, U., Arkhipov, V. I. and Bässler, H. (1999), ‘Current injection from a metal to a disordered hopping system. i. monte carlo simulation’, *Physical Review B* **59**(11), 7507.

Woon, K. and Yeo, G. (2014), ‘Vertical organic field effect phototransistor with two dissimilar source and drain contacts’, *Thin Solid Films* **562**, 525–529.

Wu, Y.-K., Huang, J.-H., Tsai, W.-W., Chen, Y.-P., Lin, S.-C., Hsu, Y., Zan, H.-W., Meng, H.-F. and Wang, L. A. (2013), ‘Solution-processed vertical organic transistors fabricated by nanoimprint lithography’, *Electron Device Letters, IEEE* **34**(2), 313–315.

Xu, Z., Li, S.-H., Ma, L., Li, G. and Yang, Y. (2007), ‘Vertical organic light emitting transistor’, *Applied Physics Letters* **91**(9), 092911.

Yang, D., Zhang, L., Wang, H., Wang, Y., Li, Z., Song, T., Fu, C., Yang, S. and Zou, B. (2015), ‘Pentacene-based photodetector in visible region with vertical field-effect transistor configuration’, *IEEE Photonics Technology Letters* **27**(3), 233–236.

Yu, X. and Kwok, H. S. (2003), ‘Optical wire-grid polarizers at oblique angles of incidence’, *Journal of applied physics* **93**(8), 4407–4412.

Zade, S. S. and Bendikov, M. (2006), ‘From oligomers to polymer: convergence in the homo-lumo gaps of conjugated oligomers’, *Organic letters* **8**(23), 5243–5246.

Zaki, T., Scheinert, S., Horselmann, I., Rodel, R., Letzkus, F., Richter, H., Zschieschang, U., Klauk, H. and Burghartz, J. N. (2014), ‘Accurate capacitance modeling and characterization of organic thin-film transistors’, *IEEE Transactions on Electron Devices* **61**(1), 98–104.

Zan, H.-W., Hsu, Y.-H., Meng, H.-F., Huang, C.-H., Tao, Y.-T. and Tsai, W.-W. (2012), ‘High output current in vertical polymer space-charge-limited transistor induced by self-assembled monolayer’, *Applied Physics Letters* **101**(9), 093307.

Zan, H.-W., Tsai, W.-W. and Meng, H.-F. (2011), 'Vertical polymer phototransistor featuring photomultiplication due to base-field shielding', *Applied Physics Letters* **98**(5), 053305.

Zschieschang, U., Ante, F., Kälblein, D., Yamamoto, T., Takimiya, K., Kuwabara, H., Ikeda, M., Sekitani, T., Someya, T., Blochwitz-Nimoth, J. et al. (2011), 'Dinaphtho [2, 3-b: 2, 3-f] thieno [3, 2-b] thiophene (dntt) thin-film transistors with improved performance and stability', *Organic Electronics* **12**(8), 1370–1375.

List of Symbols

Notable physical quantities that appear in this thesis are listed below. For each, a brief description is reported on the right-hand side with the relative symbol on the left-hand side.

First defined in Chapter 1.

η	Inverse Localization Radius
$\Delta\varepsilon_{ij}$	Energy Difference Between i-th and j-th Localized States
f_i	Occupation Probability of the i-th Localized State
k_B	Boltzmann Constant
λ_i	Decay Rate of the i-the Localized State
ν_0	Phonon Frequency
r_{ij}	Distance Between i-th and j-th Localized States
t	Time
T	Temperature
w_{ij}	Hopping Rate From Localized State i to j

First defined in Chapter 2.

α_{abs}	Absorption Coefficient
c	Speed of Light

χ	Electron Affinity
d	Density
D_n	Electron Diffusivity
D_p	Hole Diffusivity
E_A	Activation Energy
E_C	Conduction Band-Edge Energy Level
E_F	Fermi Energy Level
$E_{F,i}$	Intrinsic Fermi Energy Level
$E_{F,n}$	Electron Quasi-Fermi Energy Level
$E_{F,p}$	Hole Quasi-Fermi Energy Level
E_G	Energy Gap
E_{HOMO}	HOMO Energy Level
E_{LUMO}	LUMO Energy Level
E_μ	Mean Energy Level in Traps DOS
E_σ	Energy Spreading in Traps DOS
E_T	Trap Energy Level
E_V	Valence Band-Edge Energy Level
ε	Absolute Dielectric Constant
ε_0	Vacuum Dielectric Constant
ε_r	Relative Dielectric Constant
F	Electric Field
$F_\perp$	Normal Electric Field
F_0	Electric Field Normalization Constant
$F_{1/2}(x)$	Fermi Integral of order $1/2$

f_n	Electron Occupation Probability
g_n	Electron Density of States
g_p	Hole Density of States
G_{opt}	Optical Generation Rate
γ	Photogeneration Quantum Yield
Γ_n	Auger Coefficient for Electrons
Γ_p	Auger Coefficient for Holes
h	Planck Constant
I_{opt}	Optical Intensity Rate
J_n	Electron Current Density
J_p	Hole Current Density
k	Extinction Coefficient
λ	Optical Wavelength
m_n^*	Electron Effective Mass
m_p^*	Hole Effective Mass
μ	Mobility
μ_0	Low-Field Mobility
μ_n	Electron Mobility
μ_p	Hole Mobility
n	Free Electron Concentration
N_A	Ionized Acceptors Concentration
N_{AV}	Avogadro Number
n_c	Complex Refractive Index
N_C	Effective Density of States of the Conduction Band

N_D	Ionized Donors Concentration
N_{DOS}	Effective Density of States
N_{HOMO}	Density of Hopping Sites for the HOMO Level
n_i	Intrinsic Free Charge Concentration
N_{LUMO}	Density of Hopping Sites for the LUMO Level
n_r	Refractive Index
N_{shell}	The Number of Electrons in the Outer Electronic Shell of an Atom
N_T	Total Trap Concentration
N_V	Effective Density of States of the Valence Band
ν	Optical Frequency
p	Free Hole Concentration
Φ	Work Function
ψ	Electrostatic Potential
q	Elementary Charge
R_{net}	Net Recombination Rate
ρ	Charge Density
ρ_{trap}	Traps Charge Density
σ	Electrical Conductivity
σ_n	Energy Spreading for Electrons in the GDM
σ_p	Energy Spreading for Holes in the GDM
τ_n	Electron Lifetime
τ_p	Hole Lifetime
θ_i	Impinging Ray Angle
θ_r	Reflected Ray Angle

θ_t	Transmitted Ray Angle
V_T	Thermal Voltage
$v_{th,n}$	Thermal Velocity for Electrons
$v_{th,p}$	Thermal Velocity for Holes
w	Atomic Weight
x_n	Electron Capture Cross-Section
x_p	Hole Capture Cross-Section
ξ_n	Corrective Factor in Fermi statistics for Electrons
ξ_p	Corrective Factor in Fermi statistics for Holes
ζ	Mobility Exponent in the PL Model

First defined in Chapter 3.

α_S	A Fitting Parameter in the Estrada and Li DC Models
B	A Fitting Parameter in the Estrada DC Model
C	Electrical Capacitance
C_{ins}	Gate Insulator Capacitance
C_P	Capacitance Function (Parallel Admittance)
ε_{ins}	Gate Insulator Dielectric Constant
f_c	Cut-off Frequency
g_m	Transconductance Gain
I_D	Drain Current
I_{OFF}	Off-State Current
κ	A Field-Effect Mobility Empirical Parameter in the Li DC Model
L	Electrical Inductance

L_{CH}	Channel Length
L_P	Loss Function (Parallel Admittance)
λ_{CH}	Channel Length Modulation Factor
m	A Fitting Parameter in the Estrada and Li DC Models
μ_{FE}	Field-Effect Mobility
μ_{FE0}	Field-Effect Mobility Prefactor in DC Models
N_{fix}	Fixed Charge Density
N_{if}	Interface Traps Concentration
R	Electrical Resistance
R_C	Contact Resistance
s	A Field-Effect Mobility Empirical Parameter in the Li DC Model
SS	Subthreshold Swing
t_{ins}	Gate Insulator Thickness
t_{OSC}	Organic Semiconductor Thickness
τ_0	Charge Relaxation Lifetime
V_{AA}	Filed-Effect Mobility Normalization Factor in Marinov and Estrada DC Models
V_B	A Fitting Parameter in the Estrada DC Model
V_D	Drain Voltage
V_{DS}	Drain-Source Voltage
V_G	Gate Voltage
V_{GOV}^{abv}	Gate Overdrive Voltage (Above-Threshold)
V_{GOV}^{sub}	Gate Overdrive Voltage (Sub-Threshold)
V_{GS}	Gate-Source Voltage

V_{ON}	Onset Voltage
V_{SS}	A Fitting Parameter in the Marinov DC Model
V_{TH}	Threshold Voltage
W_{CH}	Channel Width
ω	Angular Frequency
Y_P	Parallel Admittance

First defined in Chapter 4.

α	Current Transmission Ratio
β	Current Transmission Ratio
I_{EC}	Transmission Current
I_C	Collector Current
J_C	Collector Current Density
J_D	Drain Current Density
L_{PO}	Pinch-off Length
L_{SUP}	Superposition Length
R_{OFF}^{ON}	On-Off Ratio
$\|V\|_{range}$	Operating Voltage Range

First defined in Chapter 5.

A_{BHJ}	Bulk Heterojunction Interfacial Area
d_{av}	Average Grain Size
ε_i	Ising Model Exchange Energy

$\Delta\varepsilon$	Energy Difference between Ising Model Configurations
F_i^{TE}	Incident Electric Field for TE Polarization
F_i^{TM}	Incident Electric Field for TM Polarization
F_t^{TE}	Transmitted Electric Field for TE Polarization
F_t^{TM}	Transmitted Electric Field for TM Polarization
J	Ising Model Interaction Energy
l_{BHJ}	Bulk Heterojunction Lattice Constant
N	Number of Opposite Spin 1st Order Nearest Neighbor in the Ising Model
N_{TOT}	Total Number of Lattice Sites
P_{ex}	Ising Model Exchange Probability
T^{TE}	TE Polarization Transmission
T^{TM}	TM Polarization Transmission
V_{BHJ}	Bulk Heterojunction Volume

Acronyms

The acronyms used in this thesis are listed below. For each, the extended form is reported on the right-hand side with the relative abbreviated form on the left-hand side.

4PP	4 Point Probe
AC	Alternate Coupling
AFM	Atomic Force Microscopy
BGTC	Bottom-Gate Top-Contacts
BGBC	Bottom-Gate Bottom-Contacts
BHJ	Bulk Heterojunction
BJT	Bipolar Junction Transistor
BTE	Boltzmann Transport Equation
CCM	Charge Control Model
CT	Charge Transfer
DC	Direct Coupling
DD	Drift-Diffusion
DFT	Density Functional Theory
DOS	Density Of States
EELS	Electron Energy-Loss Spectroscopy
EDA	Electronic Design Automation

EQE	External Quantum Efficiency
FDTD	Finite-Difference Time-Domain
FVM	Finite Volume Method
GDM	Gaussian Disorder Model
HIL	Hole Injection Layer
HOMO	Highest Occupied Molecular Orbital
ISC	Inter-System Crossing
IUPAC	International Union of Pure and Applied Chemistry
KP	Kelvin Probe
LCAO	Linear Combination of Atomic Orbitals
LoC	Lab-on-a-Chip
LUMO	Lowest Unoccupied Molecular Orbital
MATLAB©	Matrix Laboratory
MC	Monte Carlo
MDP	Molecularly Doped Polymer
MIS	Metal-Insulator-Semiconductor
MOSFET	Metal-Oxide-Semiconductor Field-Effect Transistor
MTR	Multiple Trapping and Release
NIR	Near Infrared
OFET	Organic Field-Effect Transistor
OLED	Organic Light Emitting Diode
OLET	Organic Light Emitting Transistor
OPBT	Organic Permeable Base Transistor
OPD	Organic Photodiode

OPT	Organic Phototransistor
OPV	Organic Photovoltaic
OSBT	Organic Schottky Barrier Transistor
OSC	Organic Semiconductor
OSIT	Organic Static Induction Transistor
PDE	Partial Differential Equation
PER	Polarization Extinction Ratio
PF	Poole-Frenkel
PL	Power Law
PMI	Physical Model Interface
POPD	Polarized Organic Photodiode
PS	Photoelectron Spectroscopy
PVD	Physical Vapor Deposition
RTA	Reflectance Transmittance Absorption
SCLC	Space Charge Limited Conduction
SIT	Static Induction Transistor
SRH	Shockley-Read-Hall
TE	Transverse Electric
TEM	Transmission Electron Microscopy
TCAD	Technology Computer Aided Design
TGTC	Top-Gate Top-Contacts
TGBC	Top-Gate Bottom-Contacts
TM	Transverse Magnetic
VDPM	Van Der Pauw Method

VOFET	Vertical Organic Field Effect Transistor
VOT	Vertical Organic Transistor
VRH	Variable Range Hopping
VS	Virtual Semiconductor
WGP	Wire Grid Polarizer